THE UNIVERSITY OF WARWICK

Library Declaration and Deposit Agreement

1. STUDENT DETAILS

Please complete the following:

Full name: ……

University ID number: ……

2. THESIS DEPOSIT

2.1 I understand that under my registration at the University, I am required to deposit my thesis with the University in BOTH hard copy and in digital format. The digital version should normally be saved as a single pdf file.

2.2 The hard copy will be housed in the University Library. The digital version will be deposited in the University's Institutional Repository (WRAP). Unless otherwise indicated (see 2.3 below) this will be made openly accessible on the Internet and will be supplied to the British Library to be made available online via its Electronic Theses Online Service (EThOS) service.
[At present, theses submitted for a Master's degree by Research (MA, MSc, LLM, MS or MMedSci) are not being deposited in WRAP and not being made available via EthOS. This may change in future.]

2.3 In exceptional circumstances, the Chair of the Board of Graduate Studies may grant permission for an embargo to be placed on public access to the hard copy thesis for a limited period. It is also possible to apply separately for an embargo on the digital version. (Further information is available in the *Guide to Examinations for Higher Degrees by Research*.)

2.4 *If you are depositing a thesis for a Master's degree by Research, please complete section (a) below. For all other research degrees, please complete both sections (a) and (b) below:*

(a) Hard Copy

I hereby deposit a hard copy of my thesis in the University Library to be made publicly available to readers (please delete as appropriate) EITHER immediately OR after an embargo period of ……..... months/years as agreed by the Chair of the Board of Graduate Studies.

I agree that my thesis may be photocopied. YES / NO (*Please delete as appropriate*)

(b) Digital Copy

I hereby deposit a digital copy of my thesis to be held in WRAP and made available via EThOS.

Please choose one of the following options:

EITHER My thesis can be made publicly available online. YES / NO (*Please delete as appropriate*)

OR My thesis can be made publicly available only after…..[date] (Please give date)
YES / NO (*Please delete as appropriate*)

OR My full thesis cannot be made publicly available online but I am submitting a separately identified additional, abridged version that can be made available online.
YES / NO (*Please delete as appropriate*)

OR My thesis cannot be made publicly available online. YES / NO (*Please delete as appropriate*)

3. GRANTING OF NON-EXCLUSIVE RIGHTS

Whether I deposit my Work personally or through an assistant or other agent, I agree to the following:

Rights granted to the University of Warwick and the British Library and the user of the thesis through this agreement are non-exclusive. I retain all rights in the thesis in its present version or future versions. I agree that the institutional repository administrators and the British Library or their agents may, without changing content, digitise and migrate the thesis to any medium or format for the purpose of future preservation and accessibility.

4. DECLARATIONS

(a) I DECLARE THAT:

- I am the author and owner of the copyright in the thesis and/or I have the authority of the authors and owners of the copyright in the thesis to make this agreement. Reproduction of any part of this thesis for teaching or in academic or other forms of publication is subject to the normal limitations on the use of copyrighted materials and to the proper and full acknowledgement of its source.

- The digital version of the thesis I am supplying is the same version as the final, hard-bound copy submitted in completion of my degree, once any minor corrections have been completed.

- I have exercised reasonable care to ensure that the thesis is original, and does not to the best of my knowledge break any UK law or other Intellectual Property Right, or contain any confidential material.

- I understand that, through the medium of the Internet, files will be available to automated agents, and may be searched and copied by, for example, text mining and plagiarism detection software.

(b) IF I HAVE AGREED (in Section 2 above) TO MAKE MY THESIS PUBLICLY AVAILABLE DIGITALLY, I ALSO DECLARE THAT:

- I grant the University of Warwick and the British Library a licence to make available on the Internet the thesis in digitised format through the Institutional Repository and through the British Library via the EThOS service.

- If my thesis does include any substantial subsidiary material owned by third-party copyright holders, I have sought and obtained permission to include it in any version of my thesis available in digital format and that this permission encompasses the rights that I have granted to the University of Warwick and to the British Library.

5. LEGAL INFRINGEMENTS

I understand that neither the University of Warwick nor the British Library have any obligation to take legal action on behalf of myself, or other rights holders, in the event of infringement of intellectual property rights, breach of contract or of any other right, in the thesis.

Please sign this agreement and return it to the Graduate School Office when you submit your thesis.

Student's signature: .....…… Date: .....

THE UNIVERSITY OF
WARWICK

AUTHOR: **Stephen Jowan Gallagher** DEGREE: **Ph.D.**

TITLE: **Zonal flow generation through four wave interaction in reduced models of fusion plasma turbulence**

DATE OF DEPOSIT: .....

I agree that this thesis shall be available in accordance with the regulations governing the University of Warwick theses.

I agree that the summary of this thesis may be submitted for publication.

I **agree** that the thesis may be photocopied (single copies for study purposes only).

Theses with no restriction on photocopying will also be made available to the British Library for microfilming. The British Library may supply copies to individuals or libraries. subject to a statement from them that the copy is supplied for non-publishing purposes. All copies supplied by the British Library will carry the following statement:

> "Attention is drawn to the fact that the copyright of this thesis rests with its author. This copy of the thesis has been supplied on the condition that anyone who consults it is understood to recognise that its copyright rests with its author and that no quotation from the thesis and no information derived from it may be published without the author's written consent."

AUTHOR'S SIGNATURE: .....

USER'S DECLARATION

1. I undertake not to quote or make use of any information from this thesis without making acknowledgement to the author.
2. I further undertake to allow no-one else to use this thesis while it is in my care.

DATE SIGNATURE ADDRESS

.....

.....

.....

.....

.....

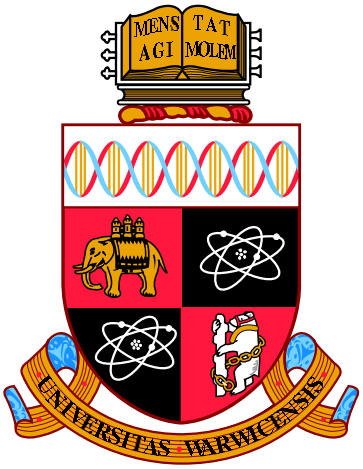

Zonal flow generation through four wave interaction in reduced models of fusion plasma turbulence

by

Stephen Jowan Gallagher

Thesis

Submitted to the University of Warwick

for the degree of

Doctor of Philosophy

Physics

August 2013

THE UNIVERSITY OF
WARWICK

Contents

List of Tables

List of Figures

Acknowledgments

First and foremost, I thank my PhD supervisor, Dr. Bogdan Hnat, for his immeasurable support and unending patience over these last few years. Without his guidance I would not have completed this thesis.

I would like to express my gratitude to Professor Sergey Nazarenko and Dr. Colm Connaughton, without their advice this thesis would contain considerably less maths. Also, to Dr. Christopher Brady. Without our many coffee break conversations I would still be trying to debug computer codes.

I have been blessed with great friends at Warwick University, Pete, Rachel, Simon, Matt, and all the rest. Thank you for your encouragement, help and entertainment; you made my time at Warwick fun.

I would like to acknowledge the staff in the CFSA and Physics department, many thanks to all of you who have helped me in any way during my time there. Also the staff of the CSC, for keeping the computers running.

I am also grateful to the EPSRC for funding my PhD research.

Finally, I thank my family for their unwavering support in all of my endeavours. Without you I could not have come so far.

Declarations

I declare that the work contained in this thesis is my own except where otherwise stated. Chapters 1, 2 and 3 contain no original work but provide a theoretical background to the subjects of fusion plasma, zonal flows, drift waves and the reduced models of plasma turbulence used in subsequent chapters. Chapter 4 describes the techniques used to write the numerical codes used throughout this work. The only original work in chapter 4 is the summary, which describes how the techniques are combined to produce the final codes. Chapters 5 to 7 all contain original work. The numerical simulations presented therein were carried out by the author, using codes written by the author. The mathematical analysis carried out in chapters 5 to 7 is based on [Connaughton et al., 2010] and was carried out by the author in collaboration with the authors of [Connaughton et al., 2010] and [Gallagher et al., 2012]. The work presented in chapter 5 has been published in [Gallagher et al., 2012]. This thesis has not been submitted for a degree at another university.

Abstract

In tokamaks, turbulence is a key contributor to cross field transport. However, it is also responsible for the spontaneous generation of large scale structures such as zonal flows. These are of relevance to fusion plasmas as they can create transport barriers which aid plasma confinement. The interaction between drift waves and zonal flows can be investigated using reduced models such as the Hasegawa-Mima and Hasegawa-Wakatani equations.

A four-wave truncated model is developed for the Extended-Hasegawa-Mima (EHM) equation. This produces a set of four ordinary differential equations (ODEs) that are used to investigate the modulational instability (MI), a mechanism by which drift waves can produce a zonal flow. These equations are linearised to produce a dispersion relation for the MI which is used to produce a set of maps of the linear growth rate of the MI. These show how additional modes become unstable as the gyroradius is increased. The truncated model and dispersion relation are then compared to measurements taken from simulations of the full EHM partial differential equation (PDE) which has been seeded with an appropriate initial condition. Good agreement is found when the pump wave has no component in the direction of the density gradient.

A similar truncated model is derived for the Extended-Hasegawa-Wakatani (EHW) equations. As the EHW system has separate equations for density and potential this leads to a set of eight ODEs. The linearisation technique used for the EHM system cannot be applied here. Instead, approximations based on the built in EHW instability are made to calculate a linear growth rate for the zonal flow using the ODEs describing it. These analytical predictions are then compared to a full PDE simulation of the system, which is initialised using random noise. It is found that for particular sets of waves the ODEs provide a good prediction of the linear growth rate.

A driving term is added to the EHM equation to reproduce the effect of the built in instability of the EHW equations. This causes a drift wave spectrum to grow when full EHW PDE simulations are seeded with random noise. The four-wave ODE model is updated to include this driving. The ODE model again produces good predictions for the growth rate of the zonal flow.

Abbreviations

EHM Extended-Hasegawa-Mima

ODE Ordinary differential equation

MI Modulational instability

PDE Partial differential equation

EHW Extended-Hasegawa-Wakatani

D–T Deuterium-Tritium

D–He^3 Deuterium-Helium-3

FLR Finite Larmor radius

MHD Magnetohydrodynamics

CHM Charney-Hasegawa-Mima

PDF Probability distribution function

KZ Kolmogorov-Zakharov

FTCS Forward time centred space

MPI Message Passing Interface

4MT Four mode truncated OR four mode truncation

ETF Energy transfer function

Chapter 1

Introduction

1.1 Thermonuclear Fusion

In recent decades it has become apparent that the burning of fossil fuels is having a detrimental effect on the global climate. An increase in the burning of fossil fuels in order to satisfy the growing energy needs of the planet is therefore not a feasible option. As a result of this many 'green' technologies have been developed in order to produce electricity without increasing carbon-dioxide output. However, there are many drawbacks to these clean power plants, the most pressing of which are perhaps the amount of land needed to produce an equivalent amount of energy to a conventional power station, and the intermittence of the supply.

Currently the only comparable clean method of producing energy is nuclear fission reactors. These however produce active waste products that cannot be released into the environment. Nuclear fusion provides a possible solution to this problem. Like a conventional fossil fuel plant it has the capacity to produce a steady supply of energy, yet, the waste products produced should be more manageable than those from nuclear fission.

Nuclear fusion is known to be operating inside the Sun, where hydrogen is fused to produce helium. The Sun uses gravitational confinement to contain plasma at densities that are not achievable on earth. The principle of energy production via fission and fusion is the same. Fusion combines light elements to produce a heavier element, whereas fission splits heavy elements, however, in both cases the products of the reaction have a lower total mass than that of the reactants and the loss of mass is converted to energy in accordance with Einstein's

$$E = mc^2$$

mass-energy equivalence formula. In order for this to happen in nuclear fusion, nuclei of light elements must come sufficiently close together that the strong force can overcome coulomb repulsion to form a new nucleus. In thermonuclear fusion collisions at high temperatures bring nuclei close enough together that they can quantum mechanically tunnel through the coulomb barrier. These requirements are included in the definition of the fusion cross section, which gives the probability of a reaction between a pair of colliding particles[Azteni and Meyer-ter-Vehn, 2004, p.4]. A graph of cross sections of power generation relevant fusion reactions is given in figure 1.1. It can be seen that the highest cross section is for Deuterium–Tritium (D–T) reactions at a temperature of approximately 100keV. It is not necessary to heat the plasma to this temperature however, as particles in the high energy tail of a Maxwellian temperature distribution, peaked at around 10keV, will be hot enough for fusion to take place. At such temperatures a D–T gas mixture will become fully ionised and form a plasma[Wesson, 2004, p.2].

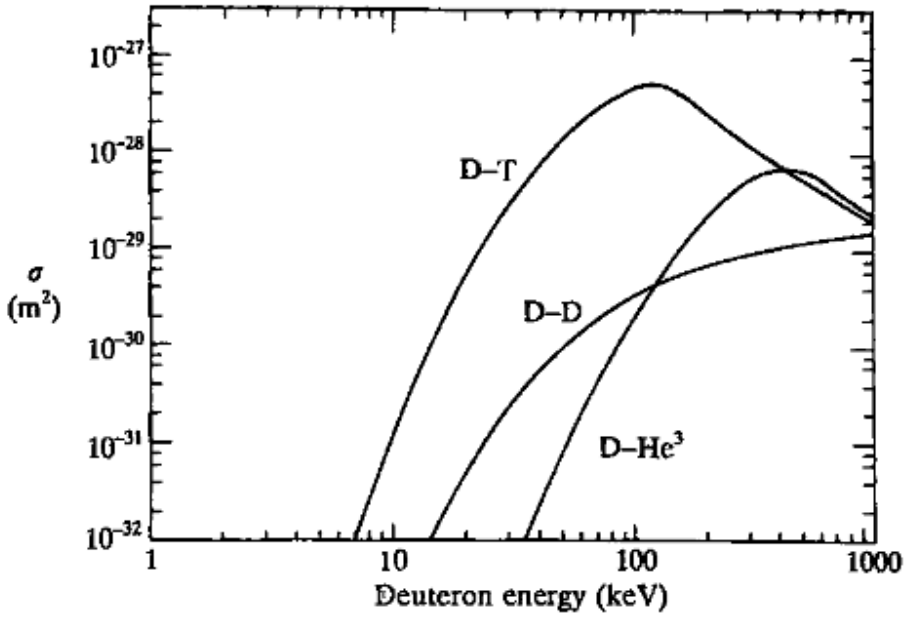

Figure 1.1: Reaction cross sections for Detuerium–Tritium (D–T), Deuterium-Deuterium (D–D) and Deuterium–Helum–3 (D–He^3) reactions. Figure from [Wesson, 2004, p.5].

In order to achieve self sustained nuclear fusion the Lawson criterion must be satisfied. This states that the energy produced by the fusion reactions taking place

must be great enough maintain the temperature of the plasma, despite losses and without any other energy input. For confinement fusion it is convenient to write this as [Wesson, 2004, p.10],

$$n_e \tau_E > \frac{12 k_B}{E_{ch}} \frac{T}{\langle \sigma v \rangle} \tag{1.1}$$

where n_e is the electron density, τ_E is the energy confinement time, T is the temperature, E_{ch} is the energy of the charged fusion products, σ is the fusion cross section and v is the relative velocity. From this point onwards the usual plasma convention of using energy units for temperature will be used and the Boltzmann constant, k_B, will be suppressed. The right hand side of (1.1) is a function of temperature which has a minimum at $T = 30keV$ where the inequality becomes[Wesson, 2004, p.11]

$$n\tau_E > 1.5 \times 10^{20} m^{-3} s. \tag{1.2}$$

There are two main approaches to creating fusion plasmas that satisfy (1.2). Firstly inertial confinement fusion attempts to rapidly achieve high densities via the compression of a pellet of Deuterium-Tritium (D–T) fuel using lasers. Secondly, magnetic fields can be used to confine low density D–T plasmas to achieve high energy confinement times. This is known as magnetic confinement fusion.

1.2 Plasma

Plasma is a state of matter where at least some of the electrons have disassociated from their atoms to leave a system to positively charged ions and negatively charged electrons. As these particles are all charged they respond to electric and magnetic fields, including any that they set up themselves via charge separation. As the electrons have less mass than the ions in the system they move more rapidly, and therefore distribute themselves so as to counteract any potentials that build up. This process is called screening. The result is that inside the plasma, fields only act over a short distance known as the debye length[Wesson, 2004, p.36]

$$\lambda_D = \left(\frac{\varepsilon_0 T_e}{n_e e^2} \right)^{\frac{1}{2}}, \tag{1.3}$$

where T_e is the electron temperature, ε_0 is the permittivity of free space, e is the charge of an electron and n_e is the electron density.

A plasma in which the density of positive charges in the plasma is equal to

the density of the negative charges, when averaged over the entire system, is called quasineutral. This can be seen by considering that a plasma in thermal equilibrium must have electrostatic energy roughly comparable to thermal energy[Hazeltine and Meiss, 2003, p.35]

$$e\phi \sim T,$$

where ϕ is electrostatic potential and T is temperature. When we restrict ourselves to considering only processes that are slow in comparison to electromagnetic waves the electrostatic approximation allows us to define the electrostatic potential using

$$\vec{E} = -\nabla\phi, \tag{1.4}$$

where $\vec{E}$ is the electric field. Poisson's equation can then be written as,

$$\nabla^2\phi = -\frac{\rho_c}{\epsilon_0}, \tag{1.5}$$

where ρ_c is the charge density. A few algebraic steps allows us to find a relation between charge separation and λ_D,

$$\begin{gathered}
\nabla \cdot \vec{E} = \frac{\rho_c}{\epsilon_0} \\
\Rightarrow \\
\frac{1}{L^2}\phi \sim e(n_e - n_i) \\
\Rightarrow \\
\frac{n_e - n_i}{n_e} \sim \left(\frac{\lambda_D}{L}\right)^2,
\end{gathered} \tag{1.6}$$

where n_i is the density of ions with unit charge. When the length scale for potential variation, L, is much greater than the Debye length the right hand side of equation (1.6) tends to zero and the quasineutrality approximation is given as

$$n_e - n_i \approx 0. \tag{1.7}$$

Quasineturality is a property of the bulk plasma and does not preclude strong local electric fields, perturbations in the charge density will lead to the creation of a potential and, via (1.4), an electric field. Charged particles are accelerated by such fields so as to counteract them. This produces a current with a corresponding local magnetic field, however, for the magnetised plasmas considered in this work, the background magnetic field is so strong that it is only slightly perturbed by these

local fields. Having gained kinetic energy whilst being accelerated by the local electric field, charged particles will overshoot the point where the field becomes 0 and instead reverse the direction of the field and direction of acceleration. This process is cyclical and leads to a wave in the plasma at a frequency

$$\omega_p = \sqrt{\frac{n_0 e^2}{m\varepsilon_0}} = \frac{1}{\lambda_D}\sqrt{\frac{T}{m}},$$

known as the plasma frequency. Having a lower mass than ions, electrons will move rapidly and screen out charge imbalances on a timescale $\frac{1}{\omega_p}$, in effect they form electron clouds around the ions. In order for a plasma to maintain quasineutrality the time between collisions of particles in the plasma, τ_c must be greater than the inverse plasma frequency, $\tau_c > \frac{1}{\omega_p}$.

1.3 Transport

1.3.1 Motion in a Magnetic Field

In the absence of an electric field charged particles will spiral around magnetic field lines. This can be shown with the Lorentz force law,

$$\vec{F} = q(\vec{E} + \vec{v} \times \vec{B}), \tag{1.8}$$

where $\vec{F}$ is the force experienced by a particle, q is its charge, $\vec{v}$ its velocity and $\vec{E}$ and $\vec{B}$ are the electric and magnetic fields present. Splitting the velocity into components parallel to the magnetic field, $\vec{v}_\parallel$, and perpendicular to it, $\vec{v}_\perp$, and in the case where there is no electric field, this becomes

$$\vec{F_\perp} = m\frac{d\vec{v_\perp}}{dt} = q\vec{v_\perp} \times \vec{B}. \tag{1.9}$$

As $\vec{v_\parallel} \times \vec{B} = 0$ there is no force parallel to the magnetic field and particles are free to move along field lines. Perpendicular to the field the particles experiences a force perpendicular to both the field lines and the velocity of the particle. The particle motion can be split into two parts, a motion along the magnetic field and a rapid gyration around it; the particle traces out a helix. The position of the centre of this helix, known as its guiding centre, is given by[Helander and Sigmar, 2005]

$$\vec{R} = \vec{r} - \frac{1}{\omega_c}\vec{b} \times \vec{v}, \tag{1.10}$$

where $\vec{b}$ is a unit vector pointing along the magnetic field, $\vec{b} = \frac{\vec{B}}{|\vec{B}|}$, and $\vec{r}$ is the position of the particle. ω_c is the angular frequency of circular motion and is known as the gyrofrequency or cyclotron frequency and is given by

$$\omega_c = \frac{qB_0}{m}. \tag{1.11}$$

Differentiating (1.10) and using equation (1.9) an equation for the velocity of the guiding centre can be obtained,

$$\frac{d}{dt}\vec{R} = \vec{v} - \frac{m}{eB}\vec{b} \times \frac{d}{dt}\vec{v} = v_{\|}\vec{b}, \tag{1.12}$$

which shows that the guiding centre moves along the magnetic field.

Equating the perpendicular force to the centripetal force experienced by a particle undergoing circular motion, an equation for the radius, at which the particle orbits the field line, can be derived. This radius is known as the Larmor radius, or equivalently the gyroradius, and is given by

$$\rho = \frac{mv_{\perp}}{qB_0}, \tag{1.13}$$

where m is the mass of the particle, $v_{\perp}$ is the velocity perpendicular to the field line, q is the charge of the particle and B_0 is the magnitude of the magnetic field.

As the particle is a charge moving in a circle it is effectively a current loop and has an associated magnetic moment

$$\mu = \frac{mv_{\perp}^2}{2B}. \tag{1.14}$$

This quantity is an adiabatic invariant and is conserved to first order, it has been shown that higher order system have an equivalent conserved property[Hazeltine and Waelbroeck, 2004, p.29].

1.3.2 Particle Drifts

There are a number of drifts in magnetised plasmas that can cause the guiding centre of individual particles to cross field lines. The general formula for a particle drift is given as

$$\vec{v}_f = \frac{1}{q}\frac{\vec{F} \times \vec{B}}{B} \tag{1.15}$$

where q is the charge on the particle, $\vec{F}$ is the force it is experiencing and $\vec{B}$ is the magnetic field. The general principle is that a force on a particle will accelerate it in

a given direction and once it is in motion it will be deflected by the magnetic field.

The $\vec{E} \times \vec{B}$ Drift

When there is an electric field present as well as a magnetic field particles will experience a drift parallel to both the magnetic and electric fields called the $\vec{E} \times \vec{B}$ drift. This can easily be shown by taking the electric field contribution to the Lorentz force law (1.8) and substituting it into the general drift equation (1.15) to give.

$$\vec{v_E} = \frac{\vec{E} \times \vec{B}}{B^2} \tag{1.16}$$

This drift is independent of both particle mass and charge so the entire plasma will drift in this direction. The electric field in this drift can be set up locally by fluctuations and is important for the phenomenon of drift waves discussed in section 1.7.1.

The $\nabla \vec{B}$ Drift

Gradients in fields can also produce drifts. Here the example of a small transverse gradient, in the $\hat{y}$ direction, of a magnetic field, in the $\hat{z}$ direction, is presented. In this case the force experienced by the particle as it orbits magnetic field lines is not constant and the orbit has a smaller radius of curvature in regions of stronger magnetic field.

The $\nabla \vec{B}$ drift for a particle can be calculated by considering its equation of motion in the direction parallel to the magnetic field gradient,

$$m\frac{dv_y}{dt} = -qv_x B. \tag{1.17}$$

If the gradient in the magnetic field is small the total magnetic field can be written as

$$B = B_0 + \frac{dB}{dy}y,$$

where y=0 is at the midplane of the orbit. Considering the total velocity in the direction perpendicular to the magnetic field as a combination of the $\nabla \vec{B}$ drift velocity and the existing perpendicular velocity gives,

$$v_x = v_{x0} + v_d,$$

where $v_d \ll v_{x0}$. This means that equation (1.17) can be written as

$$m\frac{dv_y}{dt} = -qv_{x0}(B_0 + \frac{dB}{dy}y) - qv_dB_0 - qv_d\frac{dB}{dy}y. \tag{1.18}$$

The final term in this equation contains two small parameters, v_d and $\frac{dB}{dy}$, and is therefore negligible. Considering the equations of motion for a particle moving in an unperturbed circle perpendicular to the magnetic field gives

$$v_{x0} = v_\perp \sin(\omega_c t)$$

and

$$y = \frac{v_\perp}{\omega_c}\sin(\omega_c t)$$

which can be combined with equation (1.18) to give

$$\frac{m}{q}\frac{dv_y}{dt} = -v_\perp \sin(\omega_c t)\left(B_0 + \frac{dB}{dy}\frac{v_\perp}{\omega_c}\sin(\omega_c t)\right) - v_dB_0. \tag{1.19}$$

Time averaging such that

$$< \frac{dv_y}{dt} >= 0$$

gives

$$v_d = -\frac{1}{2}\frac{v_\perp}{\omega_c}\frac{1}{B}\frac{dB}{dy}v_\perp,$$

or in vector notation

$$\vec{v}_d = \frac{1}{2}\frac{v_\perp}{\omega_c}\frac{\vec{B}\times\nabla B}{B^2}v_\perp. \tag{1.20}$$

ω_c is given by equation (1.11) and changes sign depending on the charge of the particle under consideration. This means that the ∇B drift will cause electrons and ions to drift in opposite directions. This can cause charge separation and therefore an electric field.

The Polarisation Drift

The polarisation drift occurs when there is a time varying electric field perpendicular to the magnetic field. In this case the guiding centre will accelerate at

$$\frac{d}{dt}\vec{v_E} = \frac{d}{dt}\frac{\vec{E}\times\vec{B}}{B^2}$$

which is equivalent to a force in the frame of the guiding centre of

$$\vec{F} = -m\frac{d}{dt}\frac{\vec{E}\times\vec{B}}{B^2}.$$

Once again this can be substituted into the general equation (1.15) to give the polarisation drift velocity

$$\vec{v_p} = \frac{1}{\omega_c B_0}\frac{d\vec{E}}{dt} \tag{1.21}$$

where ω_c changes sign with the charge of the particle, meaning that ions and electrons drift in opposite directions, setting up a current.

A drift that causes charge separation, such as the aforementioned ∇B drift, will create a time varying electric field which in turn will lead to a polarisation drift. The new polarisation drift will act to cancel the original drift and maintain quasineutrality, hence, $\vec{v_p} = -\vec{v_d}$. This allows the calculation of the electric field via

$$\frac{d\vec{E}}{dt} = -\vec{v}_d\omega_c B_0.$$

1.3.3 Fluid Drifts

Fluid drifts come from the collective behaviour of particles in a fluid element. In the presence of a gradient in the plasma the number of particles passing through the reference cell will vary across it. For example, it can be seen in figure 1.2 that in the presence of a density gradient a given cell will have more particles moving in one direction than the other, in this case downwards. The net effect in this this example is a downwards momentum causing the cell to drift downwards, perpendicularly to the density gradient and the magnetic field. The velocity of this drift is

$$\vec{v}_D = -\frac{\nabla p\times\vec{B}}{qnB^2} \tag{1.22}$$

where $p = nT$ is the pressure and n is density. In the case of a constant temperature this defines the diamagnetic drift, which is the drift that provides advection in the reduced models that will be discussed in chapter 3. In the presence of either a temperature or a magnetic field gradient the Larmor radius of particles will vary across the cell, again leading to a net imbalance in momentum.

In order to capture these drifts correctly with a particle description it is necessary to include the effects from charged particle gyration[Garcia, 2003]. We first define a magnetic moment

$$\vec{M} = n\langle\vec{\mu}\rangle \tag{1.23}$$

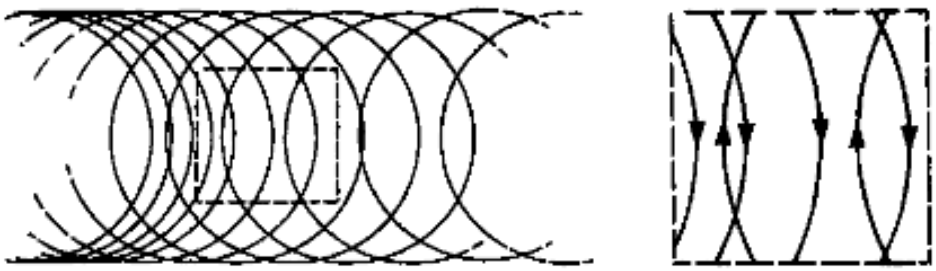

Figure 1.2: Particle orbits in a density gradient. The expanded section shows an impalance in upwards and downwards moving particles. This leads to the diamagnetic drift. Figure from [Wesson, 2004, p.87].

where the <> brackets denote a weighted average over the particle velocity distribution. Then considering the plasma as a collection of magnetic moments, as given by equation (1.14), a magnetisation current can be defined

$$\vec{j_\mu} = \nabla \times \vec{M}. \tag{1.24}$$

Defining the magnetisation drift as

$$\langle \vec{u_\mu} \rangle = \frac{\langle \vec{j_\mu} \rangle}{qn} \tag{1.25}$$

results in a total drift of

$$\langle \vec{u_B} + \vec{u_\mu} \rangle = \frac{1}{qnB} \vec{b} \times \nabla p_\perp + \frac{p_\parallel - p_\perp}{qnB} \nabla \times \vec{b}. \tag{1.26}$$

Here $\langle \vec{u_B} \rangle$ is the velocity average of the ∇B and curvature drifts as given in [Garcia, 2003]. Replacing the scaler pressure in equation (1.22) with an anisotropic pressure distribution, represented by the gyrotropic pressure tensor[Chew et al., 1956]

$$P = p_\perp (\mathbb{I} - \vec{b} \cdot \vec{b}) + p_\parallel \vec{b} \cdot \vec{b}, \tag{1.27}$$

where $\mathbb{I}$ is the unit tensor, the original diamagnetic drift becomes

$$\vec{v}_D = \frac{1}{qnB} \vec{b} \times \nabla p_\perp + \frac{p_\parallel - p_\perp}{qnB} \nabla \times \vec{b}. \tag{1.28}$$

This is identical to equation (1.26) confirming that the diamagnetic drift is in fact a consequence of particle gyration.

1.4 Fluid models

To see the origin of the fluid description of a plasma it is first necessary to consider a kinetic description. The kinetic equation is

$$\frac{\partial f_s}{\partial t} + \nabla \vec{v} \cdot f_s + \vec{a_s} \cdot \frac{\partial f_s}{\partial \vec{v}} = C_s(f), \tag{1.29}$$

where $f_s = f_s(\vec{r}, \vec{v}, t)$ is a distribution function. For each particle species s, f_s is the density of particles near point $\vec{r}$ with velocity $\vec{v}$ at time t, and $\vec{a_s}$ is the acceleration given by the Lorentz force as

$$\vec{a_s} = \frac{e_s}{m_s}\left(\vec{E} + \vec{v} \times \vec{B}\right). \tag{1.30}$$

When the collision operator is approximated by the Boltzmann collision operator, $C(f, f)$, (1.29) is known as the Boltzmann equation. $C(f, f)$ is bilinear and considers binary collisions between both like species and different species in a neutral gas. The long-range of the Coulomb interaction means that approximating the collisions as purely binary is not strictly correct, however, Debye shielding means that it is normally a good approximation[Hazeltine and Waelbroeck, 2004, p.49]. Note that (1.29) does not take into account the creation or destruction of particles, nor the changing of particles from one species to another, via ionisation for example. To do this an appropriate source term must be added to its right hand side.

Fluid models are obtained by taking moments of the kinetic equation. To do this (1.29) is multiplied by $\vec{v}^N$, where N is an integer and represents the moment being calculated, and then integrated over $\vec{v}$.

Density is defined as

$$n_s = \int d^3v f_s \tag{1.31}$$

and the flux density as,

$$n_s \vec{V_s} = \int d^3v \vec{v} f_s, \tag{1.32}$$

so that the 0-th moment of equation (1.29) describes the conservation of particles

$$\begin{aligned} \frac{\partial}{\partial t}\int d^3v f_s + \nabla \int d^3v \vec{v} \cdot f_s + \int d^3v \overline{\vec{a_s}} \cdot \frac{\partial f_s}{\partial \vec{v}} &= \int d^3v C_s(f) \\ \Rightarrow \frac{\partial}{\partial t} n_s + \nabla\left(n_s \vec{V_s}\right) &= 0 \end{aligned} \tag{1.33}$$

where the term on the right hand side is 0 as the collision operator is symmetric with respect to velocities, $C_s(f(\vec{v})) = C_s(f(-\vec{v}))$.

The stress tensor, which describes the flow of momentum in the laboratory frame, is defined as

$$\vec{P_s} = \int d^3v m_s \vec{v}\vec{v} \cdot f_s \tag{1.34}$$

and the friction force, which describes momentum transfer between particle species, as

$$\vec{F_s} = \int d^3v \vec{v} m_s C_s(f), \tag{1.35}$$

so the 1st moment describes the conservation of momentum

$$\begin{aligned} \frac{\partial}{\partial t}\int d^3v \vec{v} f_s + \nabla \int d^3v \vec{v}\vec{v} \cdot f_s + \int d^3v \vec{v}\overline{\vec{a_s}} \cdot \frac{\partial f_s}{\partial \vec{v}} &= \int d^3v \vec{v} C_s(f) \\ \Rightarrow m_s \frac{\partial}{\partial t} n_s \vec{V_s} + \nabla \vec{P_s} - e_s n_s \left(\vec{E} + \vec{V_s} \times \vec{B}\right) &= \vec{F_s}. \end{aligned} \tag{1.36}$$

To take the 2nd moment it is necessary to define the energy flux density as

$$\vec{Q_s} = \int d^3v f_s \frac{1}{2} m_s v^2 \vec{v}, \tag{1.37}$$

and the pressure tensor, which describes the flow of momentum in the rest frame of the fluid, as

$$\vec{p_s} = \int d^3v f_s m_s \vec{w_s}\vec{w_s}. \tag{1.38}$$

$\vec{w_s}$ is the relative velocity used to transform from the lab frame to the rest frame of the fluid,

$$\vec{w_s} = \vec{v_s} - \vec{V_s}. \tag{1.39}$$

Requiring that energy is conserved in collisions means that the quantity

$$W_{Lss'} = \int d^3v \frac{1}{2} m_s v^2 C_s(f) \tag{1.40}$$

must be conserved, the L subscript denotes that the energy is measured in the 'Lab' frame. This is related to the quantity measured in the rest frame of the fluid using

$$W_{ss'} = W_{Lss'} - \vec{V_s} \cdot \vec{F_s}. \tag{1.41}$$

In total this gives the 2nd moment as

$$\frac{\partial}{\partial t} \frac{1}{m_s} \vec{P_s} + \frac{2}{m_s} \nabla \vec{Q_s} + \frac{2}{m_s} e_s n_s \vec{E_s} \cdot \vec{V_s} = \frac{2}{m_s} \left(W_{ss'} + \vec{V_s} \cdot \vec{F_s}\right). \tag{1.42}$$

Using the scalar pressure

$$p_s = \frac{1}{3} Tr(\vec{p_s}), \tag{1.43}$$

where $Tr(\vec{p_s})$ indicates the trace of $\vec{p_s}$, and the relation

$$\vec{P_s} = \vec{p_s} + m_s n_s \vec{V_s} \vec{V_s} \tag{1.44}$$

equation (1.42) can be converted to the contracted 2nd moment which describes energy conservation

$$\frac{\partial}{\partial t}\left(\frac{3}{2} p_s + \frac{1}{2} m_s n_s V_s^2\right) + \nabla \cdot \vec{Q_s} - e_s n_s \vec{E_s} \cdot \vec{V_s} = W_s + \vec{V_s} \cdot \vec{F_s}. \tag{1.45}$$

For the case of two fluids, one representing electrons and the other ions, a similar procedure can be used to derive the Braginskii equations[Braginskii, 1965]. For each species these are

$$\frac{\partial}{\partial t} n + \nabla \left(n \vec{V}\right) = 0, \tag{1.46}$$

$$mn\left(\frac{\partial}{\partial t} + \vec{V} \cdot \nabla\right) \vec{V} = -\nabla p + en\left(\vec{E} + \vec{V} \times \vec{B}\right) - \nabla \cdot \Pi + \vec{F}, \tag{1.47}$$

$$\frac{3}{2} \frac{d}{dt} p + \frac{5}{2} p \nabla \cdot \vec{V} = -\nabla \cdot \vec{q} - \Pi : \nabla \vec{V} + W. \tag{1.48}$$

The subscripts have been dropped but otherwise the terms correspond to those described in the general fluid equation derivation. The only additional terms necessary are the heat flux density

$$\vec{q_s} = \int d^3 v f_s \frac{1}{2} m_s w_s^2 \vec{w_s} \tag{1.49}$$

and the generalised viscosity tensor Π. This is defined so that

$$\vec{p} = \mathbb{I} p + \Pi,$$

$\mathbb{I}$ is again the unit tensor, hence, Π contains the terms in the tensor pressure that do not come from the scalar pressure. In conventional fluids this includes effects such as viscous stress, for plasmas additional effects are possible[Hazeltine and Waelbroeck, 2004, p.54].

The Braginskii equations are coupled to Maxwells equations,

$$\nabla \cdot \vec{E} = \frac{\rho_c}{\varepsilon_0}, \tag{1.50}$$

$$\nabla \cdot \vec{B} = 0, \tag{1.51}$$

$$\nabla \times \vec{E} = -\frac{\partial \vec{B}}{\partial t}, \tag{1.52}$$

$$\nabla \times \vec{B} = \mu_0 \vec{j}, \tag{1.53}$$

through the charge density, ρ_c, and current density, $\vec{j}$, expressed as

$$\rho_c = \sum_s e_s n_s$$

and

$$\vec{j} = \sum_s e_s n_s \vec{V}_s.$$

Maxwell's correction ($+\mu_0 \varepsilon_0 \frac{\partial \vec{E}}{\partial t}$) to equation (1.53) has been dropped as we restrict ourselves to slow timescales.

From the above general fluid equations, (1.33), (1.36) and (1.45), the general problem with fluid equations can be seen; each moment of the kinetic equation is coupled to the two neighbouring moments. An exact solution therefore requires an infinite number of equations. This is known as the closure problem, there are two main approaches to solving it. The first is to truncate the series of equations by assuming that the next moment is 0, or is determined in some way by the previous moments. The second method is known as asymptotic closure and relies on the use of some small parameter in the system. The kinetic equation, (1.29), is solved perturbatively and terms above a certain order in the small parameter are neglected. The resulting distributions can be combined with moment equations to form a closed system[Hazeltine and Meiss, 2003]. For example magnetohydrodynamics (MHD) describes a plasma in the presence of a strong magnetic field where the gyroradius becomes vanishingly small, $\rho \to 0$, but the electric drift is retained by requiring

$$\frac{E_\perp}{B} \sim v_t, \text{ or } \frac{v_t}{v_E} \equiv \delta \sim 1$$

where v_t is the thermal velocity.

Here we will discuss 'drift ordering' as a way of closing the fluid equations. In this case the gyroradius is still a small parameter, however we now assume that

there are moderate electric fields so that

$$\frac{E}{B} \sim v_t, \text{ or } \frac{v_t}{v_E} \equiv \delta \gg 1.$$

This is more appropriate for confinement devices, such as tokamaks, in which diamagnetic drifts are comparable to $\vec{E} \times \vec{B}$ drifts and processes with frequencies near to the drift frequency, $\omega_\star$, are no longer negligible. A general description of the drift frequency is

$$\omega_\star = \frac{1}{qnB}\vec{k} \cdot \hat{z} \times \nabla p,$$

which is simply the product of some fluctuation in the plasma, with wave vector $\vec{k}$, and the diamagnetic drift, equation (1.22).

In order to adequately describe such a system it is necessary to retain terms that are $O(\rho)$, the physics described by these terms is known as 'finite Larmor radius', or FLR, effects. The finite size of the Larmor radius means that particles no longer see the instantaneous field, but rather a smoothed field that averages over variations on scales smaller than ρ.

In the drift model a dispersion relation can be derived using the conservation of particles, which remains identical to (1.46), and the drift equation for motion parallel to the magnetic field lines

$$m_i n \frac{\partial \vec{V_\parallel}}{\partial t} + \left(\vec{V_E} + \vec{V_\parallel}\right) \cdot \nabla \vec{V_\parallel} + \nabla_\parallel \left(p_i + p_e - 2\chi_g\right) = 0. \tag{1.54}$$

where

$$\chi_g = \frac{p_i}{2\Omega_i}\vec{b} \cdot \nabla \times \vec{V_\perp}$$

In addition the system is constrained so that electric fields parallel to the magnetic field are given by

$$E_\parallel + \frac{1}{en}\nabla_\parallel p_e \equiv \frac{F_{\parallel e}}{en} \tag{1.55}$$

It is assumed that the system is electrostatic so that $\vec{E} = -\nabla\phi$, the magnetic field is constant and in the $\hat{z}$ direction, $\vec{B} = \hat{z}B$, and the ion temperature is 0. Finally equations are linearised by assuming that they consist of a perturbation (subscript 1) around an equilibrium quantity (subscript 0) which varies only with x, such that

$$n = n_0(x) + n_1(x)e^{-i\omega t + ik_\perp y + ik_\parallel z}. \tag{1.56}$$

We assume that there are no electron collisions in the parallel direction. In this case equation (1.55) describes the ability of electrons to equilibrate a parallel electrostatic

field. They can move along the field lines sufficiency fast compared to the rate at which the potential ϕ changes that their motion can be considered instantaneous. This means that there can be no electron temperature gradient in the parallel direction so that equation (1.55) links the density perturbations to the electrostatic potential with an adiabatic electron response given by

$$\frac{n_1}{n_0} = \frac{e\phi}{T_e}, \tag{1.57}$$

where the subscript on ϕ has been dropped as $\phi_0 = 0$. Equation (1.46) can be linearised to give

$$-i\omega n_1 + ik_\parallel n_0 V_{\parallel 1} + i\omega_{\star ne} n_0 \frac{e\phi}{T_e}, \tag{1.58}$$

where

$$\omega_{\star ne} = -\frac{k_\perp T_e}{eB}\frac{dlog(n_0)}{dx} \tag{1.59}$$

is the drift frequency defined with the density gradient rather than the pressure gradient, using the ideal gas expression $p = nT$. The parallel equation of motion is then linearised to give

$$-i\omega m_i n_0 \vec{V_{\parallel 1}} + ik_\parallel p_{e1} = 0, \tag{1.60}$$

which can be combined with (1.58) to give

$$\left(\omega - \frac{k_\parallel^2 c_s^2}{\omega}\right)\frac{n_1}{n_0} = \omega_{\star ne}\frac{e\phi}{T_e}, \tag{1.61}$$

where $c_s = \sqrt{\frac{T_e}{m_i}}$ is the ion sound speed. Combining this with electron adiabaticity, equation (1.57), gives the drift wave dispersion relation

$$\omega - \omega_{\star ne} = \frac{k_\parallel^2 c_s^2}{\omega}. \tag{1.62}$$

If we now allow parallel electron collisions, equation (1.55) will no longer reduce to an adiabatic response, instead it will take the form

$$\frac{n_1}{n_0} = \frac{e\phi}{T_e}(1 - i\Delta). \tag{1.63}$$

This describes a phase shift between the density perturbation and the potential perturbation which results in an unstable drift wave. If the density perturbation leads the electrostatic potential then Δ is positive then the wave will grow. This is the basic form of a drift instability.

1.5 Magnetic Confinement Fusion

The most promising reaction for fusion power is fusing deuterium and tritium to produce an alpha particle, the reaction is written as

$$ {}_1D^2 +_1 T^3 \rightarrow_2 He^4 +_0 n^1. $$

This requires heating a plasma to around 100 million degrees centigrade, a temperature so hot that confinement by a material wall is not practical. Therefore magnetic fields are used to contain the plasma and keep it separated from the wall of a containment vessel which is keep at near vacuum conditions. To do this the internal pressure of the plasma must be balanced by an appropriate magnetic field. The mass deficit in this reaction is 0.01875 proton masses, which is equivalent to the release of 17.6MeV of energy. In a fusion device the 3.5MeV which is released in the alpha particle will be used to heat the plasma and sustain the temperatures needed for the reaction, whereas the neutrons will be able to escape the confining magnetic field so will be used to extract energy from the system for power generation. Thermonuclear fusion is a very high density energy source; D-T fusion releases around 17MeV compared to around 1eV from chemical reactions. This high energy density makes nuclear fusion a very promising source for power generation in the future.

Tokamaks are the most advanced method of producing fusion by magnetic confinement. They were invented in the Soviet Union in the 1950s[Wesson, 2004, p.27] and use a helical magnetic field in a torus to balance the outwards pressure of the plasma. This pressure balance can be seen using the ideal MHD equations[Dendy, 1990, p.58-60],

$$ \frac{\partial \rho_m}{\partial t} + \nabla \cdot (\rho_m \vec{v}) = 0, \tag{1.64} $$

$$ \rho_m \frac{\partial \vec{v}}{\partial t} = \vec{J} \times \vec{B} - \nabla p, \tag{1.65} $$

$$ \vec{E} + \vec{v} \times \vec{B} = 0, \tag{1.66} $$

where ρ_m is mass density. Faraday's law, equation (1.52), and Ampère's law, equation (1.53), are used to close the system. The system is in equilibrium when the left hand side of equation (1.65) is zero, giving

$$ \nabla p = \vec{J} \times \vec{B}, \tag{1.67} $$

which shows that the pressure gradients must be balanced by the Lorentz force law.

This implies that $\vec{B} \cdot \nabla p = 0$ and $\vec{J} \cdot \nabla p = 0$ so that p must be constant along magnetic field lines and along current lines. The simplest geometry in which this requirement can be met whilst Ampères law is still satisfied is a torus.

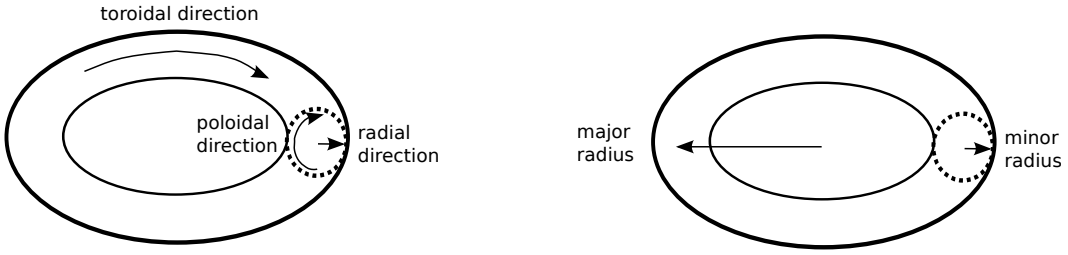

Figure 1.3: A diagram demonstrating tokamak directions (left) and the two radii of a torus (right). The dotted line indicates a ploidal cross seciton

To define the directions in a tokamak, a torus is here considered as a surface of revolution created by rotating a circle 360° around a central axis coplanar with the circle and where the axis of revolution does not touch the circle. The poloidal direction points around the circle, the radial direction along its radius and the toroidal direction points in the direction that it is rotated. Two radii define the torus, the major radius, from the centre of rotation to the centre of the circle, and the radius of the small circle, the minor radius. This is shown in figure 1.3. A computer generated image of a plan for the ITER tokamak, where the pure toroidal shape has been deformed to better contain the plasma, is shown in figure 1.4.

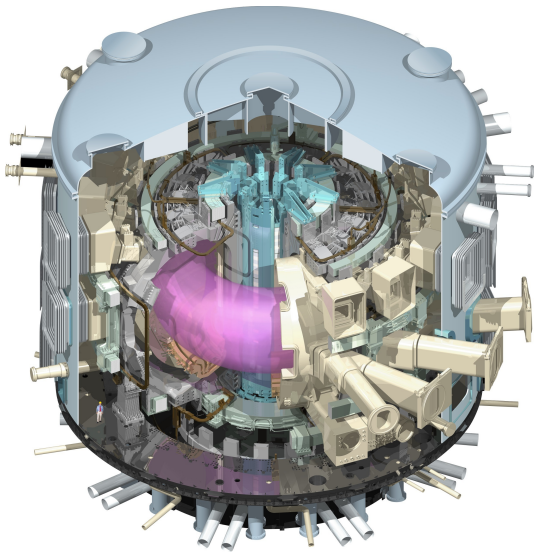

Figure 1.4: A cartoon of the ITER tokamak, under construction in France. The contained plasma is shown in pink[ITER Organisation, 2013].

To calculate the equilibrium fields and currents for a tokamak the Grad–Shafranov equation,

$$R\frac{\partial}{\partial R}\frac{1}{R}\frac{\partial \psi}{\partial R} + \frac{\partial^2}{\partial z^2} = -\mu_0 R^2 \frac{dp}{d\psi} - \mu_0^2 f \frac{df}{d\psi},$$

is used. This is derived by expanding equation (1.67) into components and writing it in terms of arbitrary functions of a poloidal magnetic field flux function, ψ, where

$$B_R = -\frac{1}{R}\frac{\partial \psi}{\partial z},\ B_z = \frac{1}{R}\frac{\partial \psi}{\partial R},$$

and f is a poloidal current density function

$$j_R = -\frac{1}{R}\frac{\partial f}{\partial z},\ j_z = \frac{1}{R}\frac{\partial f}{\partial R}.$$

The coordinate system for this system is based around the major radius of the tokamak, $\widehat{R}$ points along the major radius, $\widehat{\phi}$ is in the toroidal direction and $\widehat{z}$ is perpendicular to these directions. $R = 0$ is the major axis. Solving the Grad-Shafranov equation numerically for a typical tokamak regieme produces a set of nested flux surfaces, with radial profiles in j_ϕ, p and B_ϕ as shown in figure 1.5.

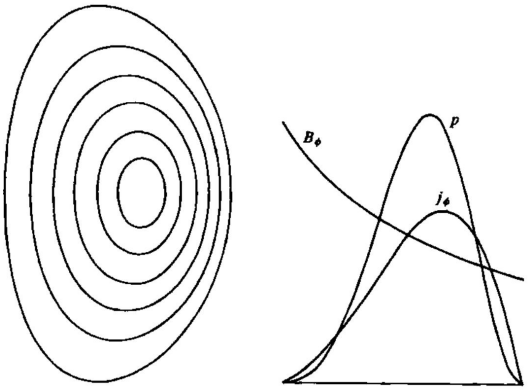

Figure 1.5: Equilibrium magnetic flux surfaces (left) and midplane profiles of toroidal current density, plasma pressure and toridal magnetic field (right). Image from [Wesson, 2004, p.111].

The basic principle of plasma confinement using a tokamak is shown in figure 1.6 and for the remainder of this paragraph *italics* refer to labels in this figure. D shaped *toroidal field coils* are used to create a magnetic field in the toroidal direction. These coils define the torus in which the plasma will be be confined. A current is driven through the *inner poloidal field coils* to produce a changing flux through the center of the torus. The *inner poloidal field coils* act as the primary winding on a transformer, and the plasma itself acts as the secondary winding. This induces a *toroidal current* in the plasma. This toroidal current produces a *poloidal magnetic field* which combines with the toroidal field to give the *resulting helical magnetic field*.

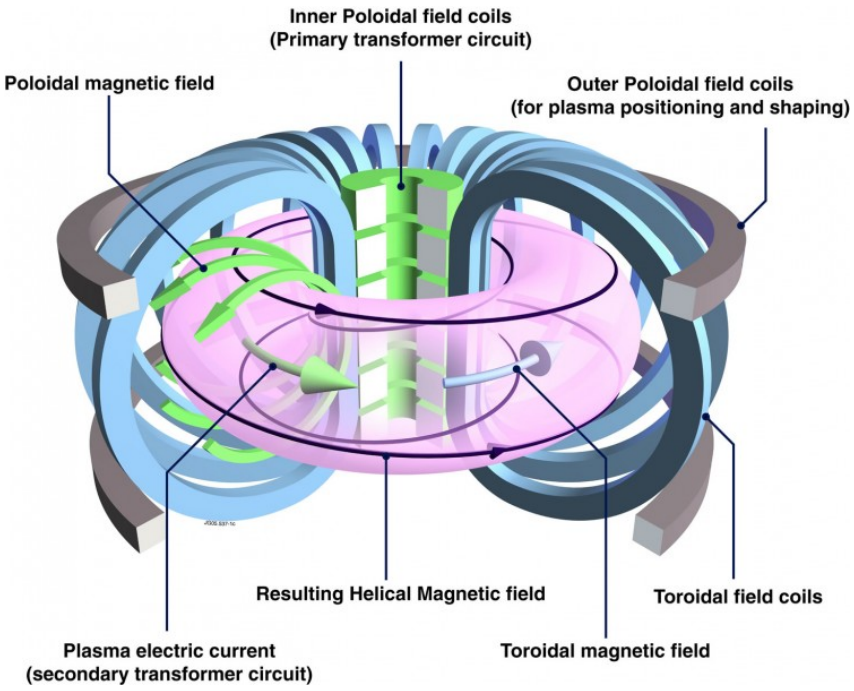

Figure 1.6: Diagram showing tokamak fields and the coils used to produce them[EFDA, 2013b].

A helical field is necessary to prevent the charge separation and drifts that would occur in a purely toroidal field. As the particles travel around the torus they experience a centrifugal force,

$$F_c = \frac{mv_\parallel^2}{R_c}, \tag{1.68}$$

where R_c is the radius of curvature. This force is directed outwards, away from the centre of curvature. The associated drift is calculated using the general drift equation, (1.15), and is given as

$$\vec{v_c} = -m\frac{v_\parallel^2}{R_c^2}\frac{\vec{R_c}\times\vec{B}}{qB^2}, \tag{1.69}$$

where the instantaneous radius of curvature, $\vec{R_c}$, is directed towards the centre of curvature.

There is also a gradient in the magnetic field and therefore a ∇B drift. This can be written as[Gurnett and Bhattacharjee, 2005]

$$\vec{v_G} = \frac{m}{2}v_\perp^2\frac{\widehat{B}\times\nabla B}{qB^2}. \tag{1.70}$$

These drifts are in the same direction and in the simple case where

$$\nabla B = \widehat{R_c}\frac{B}{R_c},$$

they can be written together as

$$\vec{v_d} = \frac{m}{q}\left(v_{\parallel}^2 + \frac{1}{2}v_{\perp}^2\right)\frac{\vec{R_c}\times\vec{B}}{R_c^2 B^2}. \tag{1.71}$$

In equation (1.71), q denotes the charge of the particle under consideration, so this drift causes charge separation. In a purely poloidal field this will create a vertical electric field. The $\vec{E}\times\vec{B}$ drift would then cause the plasma to drift radially leading to a loss of confinement. The helical field prevents this charge separation as particles are free to flow along the field lines and cancel it out.

Although the helical magnetic field prevents large drifts from charge separation, there are still a number of ways in which large scale instabilities can form. Techniques have been developed experimentally to suppress most of them, for example the MHD kink mode, so that they are no longer catastrophic in tokamaks. However, turbulence driven by micro-instabilities, such as the drift-waves discussed in section 1.7.1, is still a problem for confinement.

The plasma in a tokamak is initially heated by ohmic heating from the plasma current itself. The ohmic heating density is given as

$$P_\Omega = \eta j^2$$

where η is the resistivity of the plasma and j is the current density[Wesson, 2004]. However, as the resistivity varies as $T_e^{-\frac{3}{2}}$, this stops being an efficient heating method at temperatures of a few keV. After this there are two main schemes for heating the plasma. The first is neutral beam injection. In this case a beam of neutral atoms is injected into the plasma where collisions ionise it and transfer energy to the plasma. The second is to launch radio waves into the plasma at one of the resonant frequencies at which wave-particle interaction can take place. A number of resonances can be used, most common are ion cyclotron, lower hybrid and electron cyclotron heating[Wesson, 2004, p.261].

The other approach to producing a helical magnetic field for magnetic plasma confinement is the stellarator. In this case there is no induced toroidal current in the plasma and the twisted magnetic field lines are produced directly using helical magnetic field coils. A cartoon of the coil configuration is shown in figure 1.7. This scenario differs from the tokamak case as a stable equilibrium is calculated

in advance and the stellarator and its magnetic field are designed to impose this equilibrium on the plasma. The lack of a toroidal current in stellarators removes a source of instabilities and as such long confinement times have been achieved. In general, the physics of stellarators, as well as their design and construction, is more complex than tokamaks and as such they are less well developed as a fusion device.

Figure 1.7: A cartoon showing the coil and plasma configuration in a stellarator[EFDA, 2013a].

1.6 Collisional Transport

To describe the transport across field lines we consider particle and heat transport using flux models. For particles we write

$$\frac{\partial n}{\partial t} + \nabla \cdot \vec{\Gamma} = \vec{S_n} \tag{1.72}$$

and for heat we use

$$\frac{3}{2}\frac{\partial p}{\partial t} + \nabla \cdot \vec{q} = \vec{S_h}, \tag{1.73}$$

where $\vec{S_n}$ and $\vec{S_h}$ represent particle and heat source terms respectively. As we are interested in the transport of existing particles we will assume the source terms are negligible. Rather than a formal definition as used in a fluid model we now assume that the particle flux has the form

$$\vec{\Gamma} = -D\nabla n, \tag{1.74}$$

where D is a diffusion coefficient, and that the heat flux takes the form

$$\vec{q} = -\kappa \nabla T, \tag{1.75}$$

where κ is the thermal conductivity.

The case of straight magnetic field lines in a cylinder where particles only deviate from the field due to collisions is known as classical transport. This provides estimates on confinement time which can be up to two orders of magnitude smaller than is measured in confinement devices experimentally[Wesson, 2004, p.150].

To estimate the diffusion constant D for classical transport we assume a cross field density gradient in the $\widehat{x}$ direction. This means that we write the flux in the $\widehat{x}$ direction as

$$\Gamma_x = \frac{1}{2}(n_x - n_{x+\Delta x})V_x, \tag{1.76}$$

where

$$V_x = \frac{\Delta x}{\tau}$$

is the random walk velocity of the particles. As we are interested collisions that move particles across field lines they must cause a deviation at least as large as the Larmor radius, therefore

$$\Delta x = \rho.$$

τ is the time that it takes for multiple small deflections from the result of grazing collisions to accumulate to a total deflection of ρ[Helander and Sigmar, 2005].

We use

$$n(x + \Delta x) \simeq n(x) + \frac{\partial n}{\partial x}\Delta x$$

to write

$$\Gamma_x = -\frac{1}{2}\frac{\partial n}{\partial x}\Delta x V_x = -\frac{1}{2}\frac{\rho^2}{\tau}\nabla_x n, \tag{1.77}$$

giving a diffusion coefficient of the form

$$D \simeq \frac{1}{2}\rho^2\nu,$$

where ν is the collision frequency given by

$$\nu = \frac{1}{\tau}.$$

Momentum conservation means that collisions between ions of the same species does not cause transport, therefore we are only interested in electron-ion collisions. The electron diffusion coefficient becomes

$$D_e \simeq \frac{1}{2}\rho_e^2\nu_{ei} \tag{1.78}$$

where the e subscript denotes electrons and the ei subscript denotes electron ion

collisions. As

$$\rho_i = \left(\frac{m_i}{m_e}\right)^{\frac{1}{2}} \rho_e \tag{1.79}$$

and

$$\nu_{ie} = \left(\frac{m_e}{m_i}\right) \nu_{ei}, \tag{1.80}$$

the ion diffusion coefficient

$$D_i \simeq \frac{1}{2}\rho_i^2 \nu_{ie} = D_e$$

is equal to the electron diffusion coefficient, showing that ions and electrons contribute equally to particle transport.

The heat transport across magnetic field lines is estimated in a similar manner. The heat flux is given by

$$\vec{q} \sim n(mv_T^2/2)\vec{V}$$

and it is assumed that there is now a temperature gradient in the $\widehat{x}$ direction but no density gradient. This means that a particle making a jump of size Δx in the $\widehat{x}$ direction will produce a heat flux

$$q_x = \frac{1}{2}\frac{nm}{2}\left(v_{T_x}^2 - v_{T_{x+\Delta x}}^2\right) V_x \tag{1.81}$$

where v_T is the thermal velocity. Using the definitions given above and

$$\frac{mv_T^2}{2} = T,$$

this becomes

$$q_x \sim -\frac{\rho^2 \nu n}{2}\frac{\partial T}{\partial x}. \tag{1.82}$$

Unlike the particle case like species collisions do lead to heat transport, therefore due to equation (1.79) heat transport is dominated by ions and we have

$$q_x \simeq q_i = -\frac{\rho_i^2 n}{2\tau_{ii}}\frac{\partial T}{\partial x} \tag{1.83}$$

giving

$$\kappa = n_i \chi_i \tag{1.84}$$

where χ is the ion heat diffusivity given by

$$\chi_i = \frac{\rho_i^2}{2\tau_{ii}} \tag{1.85}$$

and τ_{ii} is the collision time for ion-ion collisions.

For tokamaks an order of magnitude improvement in confinement time estimates can be made by taking into account the curvature of the magnetic field lines in a torus. This is known as neoclassical transport.

In a tokamak the magnetic field is weaker on the outer edge. A particle moving along magnetic field lines experiences a changing magnetic field and is subject to the magnetic mirror effect. This can be seen by considering energy conservation,

$$E = \frac{m{v_\perp}^2}{2} + \frac{m{v_\parallel}^2}{2},$$

where E is the total kinetic energy of a particle. In the limit of a slowly varying magnetic field and no particle collisions this must be conserved[Dendy, 1990, p.30]. In the same limit the magnetic moment, μ, is constant and equation (1.14) shows that as B increases so must $v_\perp^2$. To keep a constant energy $v_\parallel$ must therefore decrease. If $v_\parallel$ reaches 0 before the particle moves into a region of decreasing magnetic field it will be reflected back and begin to orbit on the low field side of the torus. When projected onto the poloidal plane the shape of these orbits leads to the name 'banana orbits'.

If the plasma is sufficiently hot the collision time τ_c will be less than the time needed to complete a banana orbit τ_b, the particle will only leave the orbit when collisions have moved it a distance greater than the with of the orbit w_b. Using a random walk estimate for the diffusion coefficient, with $\Delta x = w_b$ and $\tau = \tau_b$, gives

$$D_b = \frac{(\Delta x)^2}{\tau} = \frac{w_b^2}{\tau_b}, \tag{1.86}$$

which is generally larger than D_i and leads to a lower confinement time[Wesson, 2004]. The corresponding heat diffusivity is given by

$$\chi_i^{ban} = f_t(\Delta x)^2 \nu_{eff}, \tag{1.87}$$

where $f_t \simeq (2\epsilon)^{\frac{1}{2}}$ is the fraction of particles trapped in banana orbits, $\Delta x \sim w_b$ is the step size necessary to move a particle by more than the width of an orbit and $\nu_{eff} = \frac{\nu_{ii}}{\epsilon}$ is the frequency at which collisions causing such a deviation occur. The width of a banana orbit is approximately $w_b \sim \rho_p\sqrt{\epsilon}$, where

$$\rho_p = \frac{v_T}{\Omega_p}$$

is the gyroradius in the poloidal magnetic field. In total we have

$$\chi_i^{ban} = \sqrt{2\epsilon}\rho_{pi}^2\nu_{ii}, \tag{1.88}$$

where $\epsilon = \frac{r}{R}$ is the inverse aspect ratio of the torus in question with r its minor radius and R its major radius.

Taking the ratio

$$\frac{\chi_i^{ban}}{\chi_i} = \sqrt{2\epsilon}\left(\frac{B}{B_p}\right)^2 \sim \frac{1}{2}100 \tag{1.89}$$

shows that the heat transport in the banana regime is higher than in the classical regime.

Neoclassical theory does not include small-scale fluctuations and therefore micro-turbulence related phenomena. These make up the remaining order of magnitude difference in confinement between theoretical predictions and experimental measurements. The diffusion from turbulence is labelled 'anomalous'. An estimate for anomalous diffusion is given by Bohm diffusion using a random walk estimate. It is known that turbulent structures can trap particles and aid spatial advection[Dubos and Babiano, 2003]. As the $\vec{E} \times \vec{B}$ velocity is the dominant velocity in a turbulent plasma, the velocity at which particles move during a random walk is written as

$$V_x = v_E = \frac{-\nabla\phi}{B} \sim \frac{\phi}{\Delta x B}. \tag{1.90}$$

The saturation amplitude of turbulent fluctuations is defined as $\frac{e\phi}{T} = k_0 < 1$, where Bhom estimated $k_0 = \frac{1}{16}$[Helander and Sigmar, 2005]. The step size in turbulent diffusion is approximately the size of the electrostatic structures in the plasma, this means that k_0 can be substituted into (1.90) to give

$$D_{Bohm} = \frac{(\Delta x)^2}{\tau} \sim \frac{Tk_0}{eB} = \frac{1}{16}\frac{T}{eB}.$$

Bohm diffusion is normally much faster than classical diffusion, for instance

$$\frac{D_{Bohm}}{D} \sim k_0\omega_{ce}\tau_{ei}. \tag{1.91}$$

Using values from the appendix of [Wesson, 2004], a temperature of 10keV, a density of $10^{19}m^{-3}$ and a magnetic field of 3.5T this becomes

$$\frac{D_{Bohm}}{D} \sim 3.1 \times 10^6. \tag{1.92}$$

For electrons a more complete description in [Helander and Sigmar, 2005] gives

$$D_b = (2\epsilon)^{\frac{1}{2}} \frac{\rho_p}{\tau_{ei}}, \tag{1.93}$$

which is also leads to faster diffusion in the Bohm regime than the banana regime,

$$\frac{D_{Bohm}}{D_b} \sim \frac{T}{eB} \frac{\tau_{ei}}{\rho_p} (2\epsilon)^{-\frac{1}{2}} = \omega_{ce} \tau_{ei} \rho_e \frac{B_p}{B} (2\epsilon)^{-\frac{1}{2}} \sim 3 \times 10^3. \tag{1.94}$$

Using the Bohmm diffusion coefficient the Bhom diffusion time can be defined as

$$t_{Bohm} = \frac{a^2}{D_{Bohm}}, \tag{1.95}$$

where a is the plasma radius. This quantity is used in scaling relations to make predictions for new tokamaks, Bohm scaling is when these scaling laws take the form

$$t_E = t_{Bohm} F(\beta, \nu_\star), \tag{1.96}$$

where $F(\beta, \nu_\star)$ is some function of plasma beta, the ratio of pressure to magnetic field pressure

$$\beta = \frac{p}{B^2/2\mu_0}, \tag{1.97}$$

and $\nu_\star$ is the ratio of the effective collision frequency for trapped particles to their bounce frequency. This scaling occurs when the turbulence scale is comparable with a. For high confinement, H-mode, discharges the scaling laws take the form

$$t_E = t_{Bohm} \frac{1}{\rho_\star} F(\beta, \nu_\star), \tag{1.98}$$

which is known as gyro-Bohm scaling, $\rho_\star = \frac{\rho}{a}$ is the normalised gyroradius[Wesson, 2004, p.193-194].

1.7 Turbulence

Turbulence is perhaps most often associated with fluid dynamics and is included in the Navier-Stokes equations[Frisch, 1995]

$$\partial_t \vec{v} + \vec{v} \nabla \vec{v} = -\nabla p + \nu \nabla^2 \vec{v}, \tag{1.99}$$

$$\nabla \vec{v} = 0. \tag{1.100}$$

Turbulence is a seemingly chaotic state of motion that consists of eddies at all scales. In the case of fully developed homogeneous isotropic turbulence its statistical properties do not change under translations or rotations[Frisch, 1995].

In the case of hydrodynamic turbulence a control parameter known as the Reynolds number can be introduced to describe a particular system,

$$R = \frac{LV}{\nu}, \tag{1.101}$$

where L and V are the characteristic length scale and velocity of the system and ν is its viscosity. Generally, high Reynolds numbers lead to turbulent behaviour while low Reynolds numbers lead to laminar flow. This is because the Reynolds number effectively measures the relative strength of the non-linear term ($\vec{v}\nabla\vec{v}$) as compared to the linear term ($\nu\nabla^2\vec{v}$). In the case of a low Reynolds number the Navier-Stokes equation is effectively linear whereas with a high Reynolds number the nonlinear terms will be most important in determining the development of the system. Despite being a deterministic set of equations (1.99) and (1.100) are so highly affected by initial conditions that no equation for $\vec{v}$ at a given time can be constructed[Frisch, 1995]. However, there are a number of statistical properties of turbulence, including Navier-Stokes turbulence, that are reproducible. This generally leads to the formation of probabilistic descriptions of turbulence.

One way of thinking of turbulence is as a series of cascading eddies. The system is driven on large scales and forms large eddies that break up into a number of smaller eddies. These eddies then break up and the process continues until the eddies are small enough that energy can be dissipated by viscosity. The range of scales between the energy injection and dissipation is known as the inertial range. Within this range the energy is transferred from mode k to k', where $k < k'$, without dissipation. This is the basis behind Kolmogorov's 1941 theory in which it was shown that for 3D isotropic, homogeneous and incompressible turbulence the energy spectrum of the system goes as[Frisch, 1995]

$$E(k) \sim k^{-\frac{5}{3}}. \tag{1.102}$$

The 3D turbulence model used by Kolmogorov is not appropriate for tokamak physics, in part because the presence of the magnetic field gives the turbulence a defined direction. The rapid motion of electrons along the magnetic field lines tends to suppress parallel gradients and this makes the tokamak turbulence effectively 2D, in which case enstrophy is also conserved. Enstrophy is the magnitude of vorticity

squared, for the plasma physics case used here this is

$$\mathcal{E} = |\nabla^2 \phi|^2,$$

where ϕ is the potential. Requiring that enstrophy is conserved leads to two cascades in the system[Kraichnan, 1967b]. Energy now performs an 'inverse cascade' and transfers energy to large, low wavenumber, structures such as vortices and, potentially, zonal flows. Enstrophy cascades in the usual direction and transfers energy to fine, high wavenumber, structures. In hydrodynamic turbulence this enstrophy cascade has a spectrum that goes as

$$\mathcal{E}(k) \sim k^{-3}.$$

The situation is more complicated in plasma tubulence as there is multiple scales in the system, for example there is more than one characteristic velocity, for example the sound speed and the Alfvén speed. Attempts have been made to find scaling relations for magnetised plasmas, for example by [Chen, 1965] for low beta plasmas and by Iroshnikov and Kraichnan for MHD turbulence, who predicted an energy spectrum[Biskamp, 1993]

$$E(k) \sim k^{-\frac{3}{2}}.$$

1.7.1 A physical mechanism for drift waves

Turbulence in fusion plasmas is often treated using a drift wave and drift instability formulation. In this description drift waves are generated on scales $\sim \rho_i$ and, when their amplitude becomes large, these couple to produce turbulent flows. Here we present a mechanism by which drift waves, as described by (1.62), can be produced.

We consider the case where fluctuations in density cause a small build up in charge, via an adiabatic response (1.57), and the associated increase in potential establishes an electric field according to (1.4). As there is a background magnetic field an $\vec{E} \times \vec{B}$ drift, from equation (1.16), will be established. In the particularly ideal case, presented in figure 1.8, this will cause particles to drift around the perturbation. In the presence of a background density, denser plasma will be moved into regions of low density, and vice versa. This is demonstrated in Figure 1.8 where the higher density is above the perturbation and the particles circulate clockwise. This means higher density plasma will be moved towards the right (along the positive direction of the y axis) and lower density plasma to the left, therefore the higher density of plasma that caused the initial charge perturbation will be moved to the right. If this process is continuous the density perturbation will propagate along the

y axis.

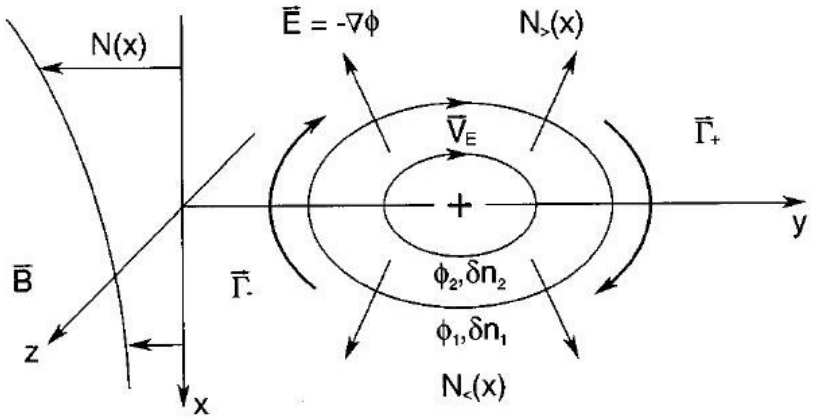

Figure 1.8: A mechanism for drift waves[Horton, 1999].

A sequence of these perturbations can form a wave, as shown in figure 1.9, where the drift wave is considered as a perturbation of a density isobar. In the example shown, this perturbation is roughly sinusoidal. The resultant $\vec{E} \times \vec{B}$ drift acts to remove the perturbations, as it does so it will increase the momentum of the plasma causing it to overshoot the unperturbed state, setting up periodic motion. Again this example is an adiabatic case the the wave travels, in the negative y direction, without growing.

On its own the process described by figure 1.8 would not lead to a loss of confinement as the y axis is roughly equivalent to the poloidal direction in a tokamak. However, a situation where the charge perturbation and the density perturbation are out of phase, with the density perturbation leading the charge perturbation, will cause the higher density plasma to be placed in a region where there is already an excess of density. This is unstable and will cause perturbation to grow. In addition there will be a net transport of plasma down the density gradient[Horton, 1999], in the case of a tokamak this corresponds to radial transport and a loss of confinement.

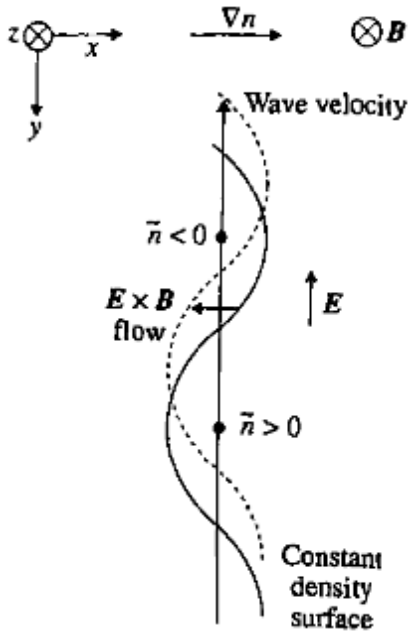

Figure 1.9: A diagram of the perturbed density surface showing how small perturbations can lead to a moving wave. Figure from[Wesson, 2004, p.420].

1.7.2 Zonal Flows

A characteristic feature of non-equilibrium turbulent systems is the growth of structures. An example of such a structure, of particular relevance to plasma physics, is the zonal flow. These are of interest as they may help to confine plasma. Zonal flows are 'azimuthally symmetric band-like shear flows'[Diamond et al., 2005], see figure 1.10, which develop from the nonlinear interactions within a plasma. Zonal flows are of particular interest because they themselves do not reduce confinement. The total energy of drift waves and zonal flows is conserved[Diamond et al., 2005], therefore as the zonal flow grows the drift wave energy reduces. The zonal flows themselves are not subject to Landau damping and can accelerate to high velocities, therefore they can store energy without causing a deterioration in confinement.

In addition to this zonal flows can shear large vortices and increase their coupling to small scales where they are dissipated more easily. In some simulations this actually breaks up the eddies and therefore reduces turbulence[Diamond et al., 2005].

The transition from drift-waves to zonal-flows is governed by two processes. The first is an inverse cascade of energy to small scales and the second is non-local resonant interactions.

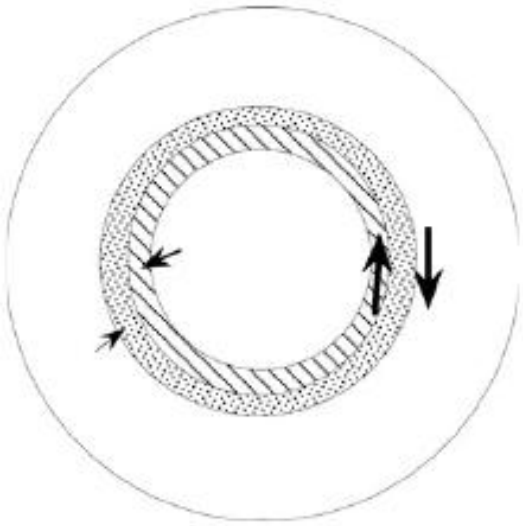

Figure 1.10: A diagram of zonal flows in a tokamak as viewed from a poloidal cross section, the hatched region denotes positive charge, the dotted negative. The large arrows give the direction of the flow[Diamond et al., 2005].

1.8 Outline

Chapter 2 gives derivations of the reduced models used throughout this work. The first half of the chapter discusses the Charney-Hasegawa-Mima (CHM) equation and begins with a derivation. The CHM was originally derived for plasmas by Akira Hasegawa and Kunioki Mima in 1978, the Charney prefix is added as it has the same form as the Quasi–Geostrophic Vorticity equation derived earlier by J Charney, in 1949, for atmospheric physics. The CHM equation is a two dimensional model of a plasma slab with a density gradient in the $\widehat{x}$ direction and a constant magnetic field. The motion of electrons along the magnetic field lines is modelled as instantaneous and therefore density and potential fluctuations are linked adiabatically via a Boltzmann response.

The chapter then proceeds to derive the Extended-Hasegawa-Mima equation, a form more appropriate to tokamaks, in which the parallel coupling between global flows and surface fluctuations is removed by altering the density response to potential variations. The EHM is then linearised to show that it has the same dispersion relation for a plane wave as the non-extended CHM case.

Finally the transform of the EHM to Fourier space is demonstrated as this version of the equation is vital to the models derived in later chapters.

The second half of chapter 3 follows a similar structure, only this time

the Extended-Hasegawa-Wakatani (EHW) equations are derived directly; extended again indicates the decoupling of global flows and surface fluctuations. The chapter then proceeds to derive the Fourier space version of the equations and finishes with the EHW linear dispersion relation, which demonstrates the ability of the EHW to grow drift waves.

Chapter 4 gives an overview of the numerical techniques used to construct the numerical codes used to solve the EHM and EHW equations. General categories of numerical schemes for solving partial differential equations (PDEs) are discussed at the beginning of the chapter, followed by the specific techniques used in this work. The chapter finishes by describing how these techniques were combined to produce the final codes used here.

Chapters 5 to 7 contain the original research in this thesis. They all begin by deriving a four-mode truncated model and an equation for the linear growth rate for the system under consideration. These analytical results are then compared to simulations.

Chapter 5 is based on work published in [Gallagher et al., 2012] and looks at the EHM system. In the style of [Connaughton et al., 2010] the dispersion relation of the four–wave zonal flow transition is used to produce maps to predict the growth rate of various modes in the system under various parameter regimes. After this four-mode ordinary differential equation (ODE) model is compared to the full PDE system and the effect of varying the gyroradius is investigated. The chapter ends with a look at a streamer case.

Chapter 6 compares a truncated model and full PDE simulations of the Extended-Hasegawa-Wakatani equations. It looks at two cases, the $\alpha = 10$ adiabatic limit, where EHM like behaviour is expected, and $\alpha = 0.5$ non-adiabatic case that is more relevant to tokamaks. The chapter finishes by using energy transfer functions to categorise local vs. non-local in k–space interactions.

Chapter 7 attempts to grow drift waves in the Extended-Hasegawa-Mima system by driving it so as to reproduce the effect of the linear dispersion relation of the Hasegawa-Wakatani system. A corresponding driving term is added to the Hasegawa-Mima reduced models so that they can be compared with the full driven system. Finally, energy transfer functions are used to isolate the strongest growing mode in the system and it is shown that the truncated model captures the growth of this mode well.

Chapter 8 is a conclusions chapter which summarises the work in chapters 5 to 7.

Chapter 2

Nonlinear Physics

2.1 Weak Turbulence

Weak turbulence differs from traditional, strong, hydrodynamic turbulence as it treats the turbulence as a system of waves rather than vortices. In reality both vortices and waves will be present[Nazarenko, 2011]. Unlike in the Richardson model, weak turbulence theory does not require interactions to be local, waves at all scales can interact simultaneously, and the nature of interaction between the waves determines the spectrum of waves [Zakharov, 1965].

Normally it is assumed that the waves in question are weakly nonlinear and dispersive. This means that the wave turbulence can be split into two timescales. There is a linear time which is approximately equal to the period of a linear wave, $\tau_L \sim \frac{2\pi}{\omega_k}$, and a nonlinear time which is considerably longer than this, $\tau_{NL} \gg \tau_L$. For time intervals that are considerably shorter than τ_{NL} the interacting waves can be approximated as independent linear waves whose amplitudes are time independent. Over longer timescales nonlinear interactions will cause their amplitude to vary. However, there is a large enough scale difference between the period of the linear variations and the variation caused by the nonlinear interactions that the rapid linear variation can be averaged over.

Wave turbulence is still described as turbulence as it deals with out of equilibrium, random nonlinear waves. In wave turbulence formalism it is assumed that the phases of the waves describing the system are independent random variables, often the same assumption is made for the amplitudes of the waves. There can be multiple sources and sinks in the system, at well separated scales. The Random phase approximation is motivated by the fact that a large number of waves can be excited across a large number of time and spatial scales and due to this statistical

techniques are required to describe the system. As with normal turbulence this description can also take the form of a flux of energy through k-space. In common with normal normal two-dimensional turbulence, multiple conserved quantities in wave turbulence can lead to dual cascades.

As an example, the multiple interacting waves of weak turbulence can be described using a Hamiltonian description. For weakly interacting waves in a box this allows us to write a general equation describing the system,

$$i\frac{\partial}{\partial t}a_k = \frac{\partial \mathcal{H}}{\partial \overline{a_k}}, \tag{2.1}$$

where $\overline{a_k}$ is the complex conjugate of a_k. The field variable a_k represents the amplitude of an interacting plane wave. The Hamiltonian is given as an expansion in powers of small amplitudes

$$\mathcal{H} = \mathcal{H}_2 + \mathcal{H}_3 + \mathcal{H}_4 ... \tag{2.2}$$

where $\mathcal{H}_2$ corresponds to an equation of motion for linear noninteracting waves and can be diagonalised to give

$$\mathcal{H}_2 = \sum_k \omega_k |a_k|^2. \tag{2.3}$$

Higher orders of $\mathcal{H}$ correspond to nonlinear interactions with $\mathcal{H}_3$ representing a three-wave interaction and $\mathcal{H}_4$ a four-wave interaction. Higher orders of $\mathcal{H}$ can be included but are usually negligible.

Although they are not written in Hamiltonian form the equations described in chapter 3 can be used to demonstrate this separation of linear and nonlinear contributions. For example the Hasegawa-Mima equation can be written in Fourier space as,

$$\partial_t \Phi_{\vec{k}} + i\Omega_{\vec{k}}\Phi_{\vec{k}} - \frac{1}{2}\sum_{\vec{k_1},\vec{k_2}} T(\vec{k},\vec{k_1},\vec{k_2})\Phi_{\vec{k_1}}\Phi_{\vec{k_2}}\delta_{\vec{k},\vec{k_1}+\vec{k_2}} = 0. \tag{2.4}$$

The linear interactions, analogous to $\mathcal{H}_2$, are described by the second term and the three-wave nonlinear interactions, analogous to $\mathcal{H}_3$, are described by the third term.

This in fact demonstrates the general form of a nonlinear term when it is represented in Fourier space, it will take the form of a summation over a series of interacting waves. The third term in equation (2.4) describes how the wave $\Phi_{\vec{k}}$ interacts with waves $\Phi_{\vec{k}_1}$ and $\Phi_{\vec{k}_2}$, where $\vec{k} = \vec{k}_1 + \vec{k}_2$. Here Φ represents the amplitude of the wave and T is an interaction coefficient.

In the case of higher order resonances the sum will be taken over more waves, with the interaction coefficient changed appropriately. Depending on the precise

system being investigated different order resonances will be present, for example it is possible for the dispersion relation of a system to exclude three-wave interactions but permit four-wave interactions[Nazarenko, 2011].

With some considerable manipulation as described in [Nazarenko, 2011; Choi et al., 2004] it is possible to develop an equation for the evolution of a probability distribution function (PDF) for wave amplitudes in a weakly turbulent system. For a single mode this can be written in terms of a flux of probabilities,

$$\frac{\partial}{\partial t}\mathcal{P}_k + \frac{\partial}{\partial s_k}\mathcal{F}_k = 0 \tag{2.5}$$

where s_j is a wave intensity given by $s_j = |a_j|^2$. $\mathcal{F}_k$ is a probability flux which will be dictated by the system under investigation.

Sources or sinks in the equation of motion do not produce sources or sinks in the probability flux. Therefore, to find a stationary solution in the inertial range one solves equation 2.5 with F=0 to give[Choi et al., 2004]

$$\mathcal{P}_k = \frac{1}{n_k^{KZ}} \exp\left(-\frac{s_k}{n_k^{KZ}}\right) \tag{2.6}$$

where n_k^{KZ} is the Kolmogorov-Zakharov (KZ) spectrum. Ultimately, this means that the integrated energy spectrum of a weakly turbulent system can be derived from the equations describing it, a process which is not possible for strong turbulence. A dimensional derivation for the KZ spectrum will be presented in section 2.3.

2.2 Strong Turbulence

2.2.1 Hydrodynamic turbulence and the Richardson model

The hydrodynamic turbulence described in section 1.7 is based on the Richardson model of interacting vortices. Turbulence theories generally makes the assumptions that the turbulence is homogeneous and isotropic. Although this is not always strictly true as the turbulence is often driven by a gradient in some quantity, such as velocity, it is generally an appropriate description when dealing with statistically averaged quantities[Biskamp, 1993].

Kolmogorov's 1941 prediction of a turbulent energy spectrum in integrated wavenumber in the form of

$$E(k) \sim k^{-\frac{5}{3}} \tag{2.7}$$

can be derived from dimensional arguments. We assume that energy is transferred

between vortices with similar sizes only, and that we are only describing the inertial range of scales where there is no energy input or dissipation, only transfer of energy from scale to scale. It is assumed that under the conditions the only relevant parameters are the energy dissipation rate ε and the wavenumber k. Firstly $E(k)$ is defined as energy for unit mass, so has units

$$[E(k)] = \frac{[\text{energy}]}{[\text{mass}]} = \frac{[\text{length}]^2}{[\text{time}]^2}.$$

We then need to combine ε, with units

$$[\varepsilon] = \frac{[\text{energy}]}{[\text{time}]} = \frac{[\text{length}]^2}{[\text{time}]^3},$$

and k, with units

$$[k] = [\text{length}^{-1}],$$

to give a formula for $E(k)$. The only way this can be done whilst keeping units consistent is

$$E(k) = \mathcal{C}\varepsilon^{\frac{2}{3}}k^{-\frac{5}{3}}, \tag{2.8}$$

where $\mathcal{C}$ is a unitless constant. This is one of the most important predictions of turbulence theory as it is often observed experimentally, it remains important for the weak turbulence discussed in section 2.1 as similar cascading states are observed in both cases.

2.2.2 Two-Dimensional Cascades

As with three-dimensional systems, two-dimensional systems conserve energy. However, as mentioned in section 1.7, two-dimensional systems also conserve enstropy. Having two conserved quantities leads to a dual cascade, with energy and enstrophy cascading in opposite directions. A Fjørtoft argument[Fjørtoft, 1953] can be used to determine the directions of the cascade.

We first denote the scale at which turbulence is excited as k_f. Then, the enstrophy production rate, η, is related to ε via

$$\eta \sim k_f^2\varepsilon.$$

Assuming that tubulence is now dissipated at both large wavenumbers, k_+, and small wavenumbers k_-, we now have two inertial ranges where energy is neither

dissipated nor exited,

$$k_- < k < k_f$$

and

$$k_f < k < k_+.$$

We also consider statistically stationary turbulence so that the dissipation rate is equal to the production rate. Let us first consider a cascade of energy from k_f to k_+ where energy must be dissipated at a rate comparable to the injection rate ε. This means that enstrophy would be dissipated at a rate

$$\sim k_+^2 \varepsilon \gg k_f^2 \varepsilon \sim \eta.$$

In a steady state this is not possible as it implies that enstrophy is being dissipated faster than it is being injected into the system. This means that energy must be dissipated at k_- and therefore cascade from k_f to k_-. It is therefore called an inverse energy cascade.

Repeating this process for enstrophy we assume that it is dissipated at k_- at a rate comparable to η. This implies that energy would be dissipated at a rate

$$\sim \frac{\eta}{k_-^2} \gg \frac{\eta}{k_f^2} \sim \varepsilon.$$

Again this is not possible as it would imply that energy would be dissipated faster than it is created. Therefore enstrophy must be dissipated at k_+ and there is a direct enstrophy cascade from k_f to k_+.

In a vortex description of turbulence these two cascades determine the evolution of the vortices. Small vortices merge to form large structures from the inverse energy cascade. Whist the vortices are merging, long thin vorticity filaments are formed by the direct enstrophy cascade.

The energy spectrum of the two-dimensional system was determined by Robert Kraichnan in 1967[Kraichnan, 1967a]. As long as both the energy and enstrophy cascades are local the Kolmogorov dimensional argument presented earlier can be used. In the inverse energy cascade range the picture is essentially unchanged and equation 2.8 is recovered, only with a different value of $\mathcal{C}$ and different sign of ε. To find the spectrum in the direct cascade range we note the dimensions of η,

$$[\eta] = [k^2][\varepsilon] = [\text{length}^{-2}]\frac{[\text{length}^2]}{[\text{time}^3]} = [\text{time}^{-3}]. \tag{2.9}$$

As with the energy case, the only way that η can be combined with k to give a

formula for $E(k)$ whilst keeping units consistent is

$$E(k) = \mathcal{C}_\eta \eta^{\frac{2}{3}} k^{-3}. \tag{2.10}$$

Dual cascades have been found in both simulations and observations of two-dimensional turbulence[Boffetta, 2007; Manz et al., 2009b; Frisch and Sulem, 1984; Hasegawa et al., 1979; Boffetta and Ecke, 2012].

2.3 Weak Turbulence Wave-Spectra

One of the main successes for wave turbulence theory is its ability to predict Kolmogorov like spectra, known as the Kolmogorov-Zakharov (KZ) spectra. Here we present dimensional arguments for the spectra, for details of the mathematics see [Nazarenko, 2011].

We consider resonant interactions of N waves, where N is the minimum number of waves for which frequency resonances,

$$\omega(\vec{k}_1) \pm \omega(\vec{k}_2) \pm ... \pm \omega(\vec{k}_N) = 0,$$

and wave vector resonances,

$$\vec{k}_1 \pm \vec{k}_2 \pm ... \pm \vec{k}_N = 0,$$

can be satisfied simultaneously[Nazarenko, 2011]. The signs will change depending on what type of interaction is occurring. Three-wave processes will have two '+' signs and one '−' sign whereas four-wave processes will have two '+' signs and two '−' signs. For an N wave process the rate of energy transfer is related to the number of waves via the relation[Nazarenko, 2011]

$$\frac{\partial E}{\partial t} \sim \varepsilon \sim E^{N-1}, \tag{2.11}$$

where ε is the rate of energy dissipation.

The KZ spectrum is obtained for the case of an incompressible fluid, in which case the density $\rho = \frac{m}{V}$ is constant. By setting $\rho = 1$ we define a system where m and V have the same units, hence $[m] = [\text{length}^3]$. In this case we can write

$$[E] = \left[\frac{1}{2}mv^2\right] = \frac{[\text{length}^5]}{[\text{time}^2]}$$

for the units of energy and

$$\frac{[E]}{[\text{length}^d]} = \left[\int E_k dk\right] = [E_k][\text{length}^{-1}]$$

for the energy density, where d is the number of dimensions. Combining these gives

$$[E_k] = \frac{[\text{length}^{6-d}]}{[\text{time}^2]}. \tag{2.12}$$

As we wish to investigate cascades in the inertial range we can write an energy balance equation,

$$\frac{\partial E}{\partial t} + \frac{\partial \varepsilon}{\partial k} = 0, \tag{2.13}$$

and use this to determine the dimensions of ε as

$$[\varepsilon] = \frac{[\text{length}^{5-d}]}{[\text{time}^3]}.$$

As we are discussing waves we write a general dispersion relation

$$\omega = \lambda k^\alpha \tag{2.14}$$

where λ depends on the particlar system being described. We use this to determine

$$[\lambda] = [\omega][k^{-\alpha}] = [\text{time}^{-1}][\text{length}^\alpha]. \tag{2.15}$$

Equation (2.11) implies that the energy transfer term must be of the form $\varepsilon^{\frac{1}{N-1}}$, combining this with k and λ to produce an equation for E_k gives

$$E_k \sim \lambda^x \varepsilon^{\frac{1}{N-1}} k^y. \tag{2.16}$$

To ensure the dimensions are consistent we must have

$$x = 2 - \frac{3}{N-1}$$

and

$$y = d - 6 + 2\alpha + \frac{5 - d - 3\alpha}{N-1}.$$

2.3.1 Examples of wave spectra

Capillary Waves

Capillary waves are waves on the surface of a liquid, the surface tension provides the restoring force for the wave. They interact via three-wave interactions and are effectively two dimensional, therefore we have $N = 3$ and $d = 2$. Their dispersion relation relies on the surface tension coefficient σ, which is the equivalent of λ in equation (2.14), it is given by

$$\omega = \sigma^{\frac{1}{2}} k^{\frac{3}{2}}.$$

This means that $\alpha = \frac{3}{2}$ and equation (2.16) becomes

$$E_k \sim \varepsilon^{\frac{1}{2}} \sigma^{\frac{1}{4}} k^{-\frac{7}{4}}$$

which is known as the Zakharov-Filonenko spectrum[Zakharov and Filonenko, 1967].

Alfvén Waves

Alfvén waves are low frequency plasma waves caused by oscillations in the ions and the magnetic field. For a weak magnetic field the system of Alfvén waves is three dimensional and the interactions are three-wave based, so we have $N = 3$ and $d = 3$. The dispersion relation is $\omega = c_A k_\parallel$ so we substitute $\alpha = 1$ and $\lambda = c_A$ into (2.14) to give

$$E_k = (\varepsilon c_A)^{\frac{1}{2}} k^{-\frac{3}{2}}.$$

This is the Iroshnikov-Kraichnan spectrum[Kraichnan, 1965].

When the magnetic field is strong the turbulence becomes very anisotropic with $k_\perp \gg k_\parallel$, in this case the turbulence is essentially two-dimensional so a system with $d = 2$ is more appropriate. In this case the spectrum is

$$E_k \sim (\varepsilon c_A)^{\frac{1}{2}} k_\perp^{-2}.$$

Langmuir Waves in Isotropic Plasmas

The oscillations described in section 1.2 are also known as Langmuir waves, when thermal effects are taken into account they have a dispersion relation

$$\omega_k = \omega_p + \frac{3}{2} v_{th} \lambda_D k^2.$$

ω_p, v_{th} and λ_D are the plasma frequency, thermal velocity and Debye length respectively. As the system has four-wave interactions the ω_p term cancels when the

system is in resonance. Therefore the λ term can be replaced by $\frac{3}{2}v_{th}\lambda_D$, $\alpha = 2$ and $d = 3$, to give[Zakharov, 1972]

$$E_k \sim v_{th}\lambda_D \varepsilon^{\frac{1}{3}} k^{-\frac{1}{3}}.$$

2.4 The Modulational Instability

The modulation instability describes the instability of a high frequency carrier wave when modulated by a low frequency envelope. For a simple description of the process we use a model for the evolution of the envelope based on the non-linear Schrödinger equation[Agrawal, 2013]

$$\frac{\partial A}{\partial z} + i\beta \frac{\partial^2 A}{\partial t^2} = i\gamma |A|^2 A \tag{2.17}$$

where A is the slowly varying envelope propagating in the z direction described by

$$A = \psi e^{i\gamma\psi^2 z}.$$

The β parameter describes group velocity dispersion and γ the amplitude of the nonlinearity. ψ^2 is the power of the waveform and is assumed to be constant.

Perturbing this solution whilst keeping the phase factor separate gives

$$A = (\psi + \varepsilon(t, z))\, e^{i\gamma\psi^2 z}. \tag{2.18}$$

This can be substituted in to equation (2.17) to give an equation for the evolution of the perturbation,

$$\frac{\partial \varepsilon}{\partial z} + i\beta \frac{\partial^2 \varepsilon}{\partial t^2} = i\psi^2\gamma(\varepsilon + \varepsilon^\star), \tag{2.19}$$

where terms $\mathcal{O}(\varepsilon^2)$ have been dropped as $\varepsilon \ll 1$. Defining

$$\varepsilon = a_1 e^{i(kx - wt)} + a_2 e^{-i(kx - wt)} \tag{2.20}$$

gives a dispersion relation

$$k = \pm\sqrt{\beta^2\omega^2 + 2\gamma\beta\psi^2\omega^2}. \tag{2.21}$$

It should be noted that equation (2.17) has factored out the frequency of the carrier waves meaning that ω and k are actually relative to its frequency and wavenumber, ω_0 and k_0. Therefore, the absolute frequencies and wave vectors of the unstable perturbations are $\omega_0 \pm \omega$ and $k_0 \pm k$. This means that the two terms

in (2.20) represent two waves with frequency components $\omega_0 + \omega$ and $\omega_0 - \omega$. These are the sidebands that will be discussed in chapter 5.

For the case of anomalous dispersion β is negative, in which case the the quantity under the square root in equation (2.21) can be negative and the sideband frequencies will contain an imaginary part, leading to an unstable envelope. This implies that the modulation of a system of high frequency waves by a low frequency envelopes in unstable, hence the name modulational instability.

The Zakharov Equations

For a more physical description of the modulational instability relevant in a plasma physics context we will use the Zakharov equations[Dendy, 1990],

$$-2i\omega_p \frac{\partial \vec{\overline{E}}}{\partial t} - 3v_{T_e}^2 \nabla \left(\nabla \cdot \vec{\overline{E}} \right) + c^2 \nabla \times \left(\nabla \times \vec{\overline{E}} \right) + \omega_p^2 \frac{\delta n}{n_0} \vec{\overline{E}} = 0, \tag{2.22}$$

$$\left(\frac{\partial^2}{\partial t^2} - c_s^2 \nabla^2 \right) \delta n - \frac{\varepsilon_0}{4M} \nabla^2 |\vec{\overline{E}}|^2 = 0. \tag{2.23}$$

These are two fluid equations, one modelling a fluid of electrons and one a fluid of ions; ω_p is the electron plasma frequency, M is the ion mass and c_s the ion-acoustic speed. The large difference between the mass of an electron and an ion mean that they accelerate very differently in response to an applied force. To model this the derivation of the Zakharov equations splits the density into an ion density part

$$n_i = n_0 + \delta n_i \tag{2.24}$$

and an electron density part

$$n_e = n_0 + \delta n_e + \tilde{n}_e \tag{2.25}$$

where n_0 is a time independent equilibrium value, the δn terms describe a slow timescale perturbation and $\tilde{n}_e$ is a rapid electron perturbation. In this case the quasineutrality condition becomes $\delta n_i \simeq \delta n_e$. Assuming that the electric fields in the plasma only come from deviations from charge neutrality they are given by

Poisson's equation, (1.4), this leads to electric fields given by

$$\vec{E} = \vec{\tilde{E}} + \vec{E}_{\text{slow}} \tag{2.26}$$

$$\nabla \cdot \vec{\tilde{E}} = \frac{-e\tilde{n}_e}{\varepsilon_0} \tag{2.27}$$

$$\nabla \cdot \vec{E}_{\text{slow}} = \frac{-e(\delta n_e - \delta n_i)}{\varepsilon_0}. \tag{2.28}$$

The electric field related to rapid oscillations can then be split further into

$$\vec{\tilde{E}}(\vec{r},t) = \frac{1}{2}\vec{\overline{E}}(\vec{r},t)e^{-i\omega_{pe}t} + c.c. \tag{2.29}$$

where $\vec{\overline{E}}$ is a slowly varying electric field and $c.c$ indicates the complex conjugate. This slowly varying electric field is the only one not eliminated during the derivation the the Zakharov equations.

It is possible to define a dimensionless parameter for this system by taking the ratio of the average electric field energy to the thermal energy[Dendy, 1990],

$$\overline{W} = \frac{\varepsilon_0 < |\vec{\tilde{E}}|^2 >}{2} \frac{1}{n_0 k_B T_e} = \frac{\varepsilon_0 |\vec{\overline{E}}|^2}{4 n_0 k_B T_e}. \tag{2.30}$$

This is is known as the turbulence parameter.

Dividing equation (2.23) by n_0, using this equation for $\overline{W}$ and the definition of the ion-acoustic velocity for this system, $c_s = \sqrt{\frac{k_B(T_e+3T_i)}{M}}$, gives

$$\frac{\partial^2}{\partial t^2}\frac{\delta n}{n_0} = c_s^2 \nabla^2 \left(\frac{\delta n}{n_0} + \overline{W} \right). \tag{2.31}$$

This has a stationary solution when $\frac{\delta n}{n_0} = -\overline{W}$ which describes a system where regions of enhanced electric field amplitude correspond to regions of depleted ion densities. In this situation we have

$$\frac{\delta n}{n_0} < 0. \tag{2.32}$$

In the Zakharov system the equation for the evolution of $\vec{\tilde{E}}$ is

$$\frac{\partial^2 \vec{\tilde{E}}}{\partial t^2} + \omega_{pe}^2 \left(1 + \frac{\delta n}{n_0} \right) \vec{\tilde{E}} - 3 v_{Te}^2 \nabla \left(\nabla \cdot \vec{\tilde{E}} \right) + c^2 \nabla \times \left(\nabla \times \vec{\tilde{E}} \right) = 0. \tag{2.33}$$

Neglecting the last term and looking for solutions of the form $e^{i(\vec{k}\vec{r}-\omega t)}$ leads to a

dispersion relation

$$\omega^2 = \omega_{pe}^2 \left(1 + \frac{3k^2}{k_D^2} + \frac{\delta n}{n_0}\right), \tag{2.34}$$

where in general $\frac{k^2}{k_D^2} < 1$. There are two cases of interest here, the first has

$$|\frac{\delta n}{n_0}| < \frac{3k^2}{k_D^2} \tag{2.35}$$

in which case equations (2.32) and (2.34) indicate that for a given wavenumber, k, a wave in a region of density depletion will have a lower frequency, ω, than in a region where $\delta n = 0$. The second case is where

$$|\frac{\delta n}{n_0}| > \frac{3k^2}{k_D^2}, \tag{2.36}$$

in which case equatiosn (2.32) and (2.34) indicate that

$$\omega < \omega_{pe}. \tag{2.37}$$

As waves travel through inhomogeneous materials their frequency tends to stay constant while their wavenumber changes. This means that if a wave with a small enough wavenumber to satisfy equation (2.36) tries to propagate to a region without a density depletion, $\frac{\delta n}{n_0} \geq 0$, it cannot satisfy equations (2.34) and (2.37) simultaneously whilst maintaining a constant frequency. The result is that waves can become trapped in regions of depleted density, in the stationary case discussed here this implies waves are trapped when

$$\overline{W} > \frac{3k^2}{k_D^2}. \tag{2.38}$$

This process is not stable, when an electrostatic wave is trapped it will increase the local electric field energy and hence the value of $\overline{W}$. This will lead to more waves becoming trapped, this process will continue until the equations we have been using cease to be appropriate. This is again the modulational instability as it is the result of the high frequency waves described by $\vec{\tilde{E}}$ being modulated by a low frequency wave, $\vec{\overline{E}}$.

Chapter 3

Reduced equations of laboratory plasma transport

3.1 The Hasegawa-Mima equation

3.1.1 Introduction

The Hasegawa-Mima equation is a reduced model of plasma that is primarily used to study plasma turbulence. It assumes that changes in density are linked to changes in potential adiabatically and can be modelled via a Boltzmann response, equation (3.2). The system is simplified so that it can be represented as a two dimensional slab of plasma with a constant magnetic field and fixed density gradient.

This results in a 'single fluid' model of plasma potential that can be investigated using well known numerical and analytical techniques. The shortcoming of the Hasegawa-Mima model is its reliance on prescribed initial conditions, there is no instability inherent in the system and energy and enstrophy are conserved. To study a particular phenomenon, such as the drift wave to zonal flow transition, the system must be initialised with a potential profile that will trigger the behaviour of interest.

The Hasegawa-Mima equation, as derived by Akira Hasegawa and Kunioki Mima in 1978[Hasegawa and Mima, 1978], is the same formula as the Quasi-Geostrophic Vorticity Equation developed by Jule G. Charney in 1949 for atmospheric physics[Charney, 1949]. Only the meaning of the parameters differs. As such we will refer to the Hasegawa-Mima equation as the Charney-Hasegawa-Mima (CHM) equation, and the extended version introduced in section 3.1.3, which is more appropriate for tokamak plasmas, as the Extended-Hasegawa-Mima (EHM) equation.

3.1.2 Derivation

We now define a cooridnate system using the normal plasma convention. The $\widehat{z}$ direction is along the magnetic field so that $\vec{B} = B_0\widehat{z}$. $\widehat{x}$ and $\widehat{y}$ are in the plane perpendicular to the magnetic field with $\widehat{x}$ pointing along the density gradient. When relating this back to a tokamak the $\widehat{x}$ direction should be thought of as the radial direction and the $\widehat{y}$ as the poloidal direction.

Also, it is assumed that the system can be considered electrostatic and the electric field $\overrightarrow{E}$ is given by

$$\overrightarrow{E} = -\nabla\phi, \tag{3.1}$$

where ϕ is the electrostatic potential, which is assumed to vary with x and y only.

The density response of the electrons to the magnetic field is modelled as adiabatic, which is to say their motion along the magnetic field is fast enough to be considered instantaneous, as described in section 1.4. Density is therefore given by

$$n_e = n_e(x) = n_0(x)e^{\frac{e\phi}{T_e}}, \tag{3.2}$$

where n_e is the density of the electrons (assuming quasi-neutrality gives $n = n_i = n_e$), e is the charge on an electron and T_e is the electron temperature. Throughout this derivation the subscript e denotes electrons and the subscript i denotes ions.

Equation (3.2) can be Taylor expanded to

$$n_e \approx n_0(x)(1 + \frac{e\phi}{T_e} + \cdots), \tag{3.3}$$

which is the form that will be used later in this derivation.

Conservation of Momentum

Drifts for the ions are derived using the momentum balance equation. This is obtained by neglecting collisions and rewriting equation (1.36) as

$$m_i n(\frac{\partial\overrightarrow{v_i}}{\partial t} + (\overrightarrow{v_i} \bullet \nabla)\overrightarrow{v_i}) = \frac{d\overrightarrow{v_i}}{dt} = -\nabla P_i + en(\overrightarrow{E} + \overrightarrow{v_i} \times \overrightarrow{B}), \tag{3.4}$$

where m_i is the mass of the ions and $\overrightarrow{v_i}$ is their velocity.

$\vec{E} \times \vec{B}$ drift

We assume that the effects of gyrations can be averaged out by restricting ourselves to processes that occur more slowly than the ion gyrofrequency ω_i,

$$\omega \ll \omega_i = \frac{eB_0}{m_i}, \tag{3.5}$$

where ω is the frequency regime we are considering and B_0 is the magnitude of $\overrightarrow{B}$. Also, considering only the case of cold ions gives $\nabla P_i = 0$. This means that to first order, assuming there is no acceleration, equation (3.4) can written as

$$\overrightarrow{E} + \overrightarrow{v_i} \times \overrightarrow{B} = 0.$$

Hence, taking the cross product with $\overrightarrow{B}$ of both sides of this equation and using the vector identity $(\vec{C} \times \vec{B}) \times \vec{A} = (\vec{A} \bullet \vec{C})\vec{B} - (\vec{A} \bullet \vec{B})\vec{C}$ gives

$$-\overrightarrow{E} \times \overrightarrow{B} = (\overrightarrow{B} \bullet \overrightarrow{v_i})\overrightarrow{B} - (\overrightarrow{B} \bullet \overrightarrow{B})\overrightarrow{v_i} = -{B_0}^2\overrightarrow{v_i},$$

where $\overrightarrow{B} \bullet \overrightarrow{v_i} = 0$ as $\overrightarrow{B}$ is perpendicular to $\overrightarrow{v_i}$. This can be rearranged to give

$$\overrightarrow{v_i} = \overrightarrow{E} \times \frac{\overrightarrow{B}}{{B_0}^2} = \overrightarrow{v_E}. \tag{3.6}$$

$\overrightarrow{v_E}$ is the $\overrightarrow{E} \times \overrightarrow{B}$ drift which can also be written as

$$\overrightarrow{v_E} = -\nabla\phi \times \frac{\overrightarrow{\hat{z}}}{B_0}. \tag{3.7}$$

Polarisation Drift

Equation (3.6) does not allow for compression of the ions so quasineutrality can not be satisfied, meaning a second order correction is needed. The polarisation drift is derived by substituting the $\overrightarrow{E} \times \overrightarrow{B}$ drift, equation (3.6), in to the Ion Momentum balance, equation (3.4), again neglecting the pressure term, hence

$$\frac{d\overrightarrow{v_E}}{dt} = \frac{e}{m}(-\nabla\phi + \overrightarrow{v} \times \overrightarrow{B}).$$

Again taking the cross product of both sides with $\overrightarrow{B}$ and using the aforementioned vector identity gives

$$\frac{d}{dt}(\overrightarrow{v_E} \times \overrightarrow{B}) = \frac{e}{m}\{-\nabla\phi \times \overrightarrow{B} + (\overrightarrow{B} \bullet \overrightarrow{v_E})\overrightarrow{B} - (\overrightarrow{B} \bullet \overrightarrow{B})\overrightarrow{v_E}\} = -\frac{e}{m}\nabla\phi \times \overrightarrow{B} - \frac{e}{m}{B_0}^2\overrightarrow{v},$$

$\overrightarrow{B} \bullet \overrightarrow{v_E} = 0$ as $\overrightarrow{B}$ is perpendicular to $\overrightarrow{v_E}$, so by expanding the left hand side,

$$\frac{\partial}{\partial t}(\overrightarrow{v_E} \times \overrightarrow{B}) + (\overrightarrow{v_E} \bullet \nabla)(\overrightarrow{v_E} \times \overrightarrow{B}) = -\frac{e}{m}\nabla\phi \times \overrightarrow{B} - \frac{e}{m}{B_0}^2\overrightarrow{v}.$$

Substituting for $\overrightarrow{v_E}$ gives

$$\frac{-1}{{B_0}^2}\frac{\partial}{\partial t}((\nabla\phi \times \overrightarrow{B}) \times \overrightarrow{B}) - \frac{1}{{B_0}^2}(\overrightarrow{v_E} \bullet \nabla)((\nabla\phi \times \overrightarrow{B}) \times \overrightarrow{B}) = -\frac{e}{m}\nabla\phi \times \overrightarrow{B} - \frac{e}{m}{B_0}^2\overrightarrow{v}.$$

Using the same vector relation as earlier gives

$$\frac{-1}{{B_0}^2}\frac{\partial}{\partial t}((\overrightarrow{B}\bullet\nabla\phi)\overrightarrow{B} - {B_0}^2\nabla\phi) - \frac{1}{{B_0}^2}(\overrightarrow{v_E}\bullet\nabla)((\overrightarrow{B}\bullet\nabla\phi)\overrightarrow{B} - {B_0}^2\nabla\phi) = -\frac{e}{m}\nabla\phi\times\overrightarrow{B} - \frac{e}{m}{B_0}^2\overrightarrow{v}.$$

As ϕ is a flux function given as $\phi = \phi(x, y)$ only, this means $\overrightarrow{B} \bullet \nabla\phi = 0$, hence,

$$\frac{1}{{B_0}^2}\frac{\partial\nabla\phi}{\partial t} + \frac{1}{{B_0}^2}(\overrightarrow{v_E} \bullet \nabla)\nabla\phi = -\frac{e}{mB_0^2}\nabla\phi \times \overrightarrow{B} - \frac{e}{m}\overrightarrow{v}.$$

Rearranging (3.5) and substituting for B_0,

$$\frac{e}{m\omega_i B_0}\frac{\partial}{\partial t}\nabla\phi + \frac{e}{m\omega_i B_0}(\overrightarrow{v_E} \bullet \nabla)\nabla\phi = -\frac{e}{mB_o^2}\nabla\phi \times \overrightarrow{B} - \frac{e}{m}\overrightarrow{v},$$

which can be rearranged to give

$$\begin{aligned}\overrightarrow{v} &= \frac{1}{B_0^2}\nabla\phi \times \overrightarrow{B} - \frac{1}{\omega_i B_0}\frac{\partial}{\partial t}\nabla\phi - \frac{1}{\omega_i B_0}(\overrightarrow{v_E} \bullet \nabla)\nabla\phi \\ &= \overrightarrow{v_E} - \frac{1}{\omega_i B_0}\frac{\partial}{\partial t}\nabla\phi - \frac{1}{\omega_i B_0}(\overrightarrow{v_E} \bullet \nabla)\nabla\phi. \end{aligned} \tag{3.8}$$

This is the sum of the $\overrightarrow{E} \times \overrightarrow{B}$ drift and the polarisation drift, which is given by

$$\overrightarrow{v_p} = \frac{1}{\omega_i B_0}(-\frac{\partial}{\partial t}\nabla_\perp\phi - (\overrightarrow{v_E} \bullet \nabla)\nabla_\perp\ \phi). \tag{3.9}$$

The total velocity of the ions is therefore

$$\overrightarrow{v_i} = \overrightarrow{v_E} + \overrightarrow{v_p}. \tag{3.10}$$

Conservation of Mass

Finally, the CHM equation is derived using the conservation of mass, which is expressed using the ion continuity equation, (1.33), rewritten as

$$\frac{\partial n}{\partial t} + \nabla(n \bullet \overrightarrow{v_i}) = 0 \tag{3.11}$$

or

$$\frac{\partial n}{\partial t} = -(\overrightarrow{v_i} \bullet \nabla)n - n(\nabla \bullet \overrightarrow{v_i}).$$

This can be rearranged to give

$$\frac{\frac{\partial n}{\partial t} + (\overrightarrow{v_i} \bullet \nabla)n}{n} = \frac{dln(n)}{dt} = -(\nabla \bullet \overrightarrow{v_i}). \tag{3.12}$$

To continue we take the divergence of both of the drifts derived earlier. As we are in an electrostatic regime and B_0 is a constant this gives

$$\nabla \bullet \overrightarrow{v_E} = -\nabla \bullet \frac{\overrightarrow{E} \times \overrightarrow{B}}{B_0} = 0$$

for the $\vec{E} \times \vec{B}$ drift.

We are dealing with an equation to describe a plasma in a two dimensional slab so we make the assumption that there is no velocity in the direction of the magnetic field. This gives the divergence of the polarisation drift as

$$\nabla \bullet \overrightarrow{v_p} = \nabla_\perp \bullet \overrightarrow{v_p} = \frac{1}{\omega_i B}(\nabla_\perp{}^2 \frac{\partial \phi}{\partial t} + (\overrightarrow{v_E} \bullet \nabla)\nabla_\perp{}^2 \phi), \tag{3.13}$$

which can be used as the right hand side of (3.12). The quantity $\nabla^2\phi$ is known as vorticity.

Now, using equation (3.3) and the Taylor expansion for a natural logarithm,

$$ln(n) = ln(n_0(1 + \frac{e\phi}{T_e})) = ln(n_0) + ln(1 + \frac{e\phi}{T_e}) \approx ln(n_0) + \frac{e\phi}{T_e}, \tag{3.14}$$

the left hand side of equation (3.12) becomes

$$\frac{\partial}{\partial t} + (\overrightarrow{v_E} \bullet \nabla)(ln(n_0) + \frac{e\phi}{T_e}),$$

and it can be written as

$$(\frac{\partial}{\partial t} + (\overrightarrow{v_E} \bullet \nabla))(ln(n_0) + \frac{e\phi}{T_e} - \frac{1}{\omega_i B_0}\nabla_\perp{}^2 \phi) = 0. \tag{3.15}$$

Using the definition of $\vec{v_E}$, equation (3.7), and some rearranging gives

$$(\frac{\partial}{\partial t} - \frac{1}{B_0}\frac{T_e}{e}(\nabla\frac{e\phi}{T_e} \times \vec{\hat{z}}) \bullet \nabla)(ln(n_0) + \frac{e\phi}{T_e} - \frac{T_e}{\omega_i B_0 e}{\nabla_\perp}^2\frac{e\phi}{T_e}) = 0. \tag{3.16}$$

Rewriting the gyroradius, equation (1.13), as

$${\rho_s}^2 = \frac{T_e}{m_i {\omega_i}^2} \tag{3.17}$$

gives

$$(\frac{\partial}{\partial t} - \frac{{\rho_s}^2 eB_0}{m_i}(\nabla\frac{e\phi}{T_e} \times \vec{\hat{z}}) \bullet \nabla)(ln(n_0) + \frac{e\phi}{T_e} - \frac{{\rho_s}^2 eB_0}{\omega_i m_i}{\nabla_\perp}^2\frac{e\phi}{T_e}) = 0. \tag{3.18}$$

Then using the ion gyrofrequency, equation (1.11),

$$\omega_i = \frac{eB_0}{m_i}$$

and dividing through by ω_i gives

$$(\frac{1}{\omega_i}\frac{\partial}{\partial t} - {\rho_s}^2(\nabla\frac{e\phi}{T_e} \times \vec{\hat{z}}) \bullet \nabla)(ln(n_0) + \frac{e\phi}{T_e} - {\rho_s}^2{\nabla_\perp}^2\frac{e\phi}{T_e}) = 0. \tag{3.19}$$

Using the normalizations

$$\frac{e\phi}{T_e} \to \phi,$$

$$\frac{x, y}{\rho_s} \to x, y$$

and

$$\omega_i t \to t,$$

equation (3.19) can be simplified to

$$(\frac{\partial}{\partial t} - (\nabla\phi \times \vec{\hat{z}}) \bullet \nabla)(ln(n_0) + \phi - {\nabla_\perp}^2\phi) = 0. \tag{3.20}$$

Upon expanding and rearranging this becomes

$$\begin{aligned}\frac{\partial}{\partial t}(\phi - \nabla_\perp^2\phi) - (\frac{\partial\phi}{\partial y}\frac{\partial ln(n_0)}{\partial x} - \frac{\partial\phi}{\partial x}\frac{\partial ln(n_0)}{\partial y}) - (\frac{\partial\phi}{\partial y}\frac{\partial\phi}{\partial x} - \frac{\partial\phi}{\partial x}\frac{\partial\phi}{\partial y}) \\ - (\frac{\partial\phi}{\partial y}\frac{\partial\nabla_\perp^2\phi}{\partial x} - \frac{\partial\phi}{\partial x}\frac{\partial\nabla_\perp^2\phi}{\partial y}) = 0.\end{aligned} \tag{3.21}$$

Using $v_* = \frac{\partial ln(n_0)}{\partial x}$ and the condition $n_0 = n(x)$ only this can be simplified to

$$\frac{\partial}{\partial t}(\phi - \nabla_\perp^2 \phi) - v_*(\frac{\partial \phi}{\partial y}) - [\phi, \nabla_\perp^2 \phi] = 0. \tag{3.22}$$

This is the Hasegawa-Mima equation, which describes how the potential in the system will evolve in time and space. The square bracket is a Poisson bracket defined as

$$[A, B] = \frac{\partial A}{\partial x}\frac{\partial B}{\partial y} - \frac{\partial B}{\partial x}\frac{\partial A}{\partial y}. \tag{3.23}$$

In order to more accurately represent observed phenomena it is possible to extend the Hasegawa-Mima equation by adding terms to introduce viscosity and driving. The viscosity term is given as

$$-\nu\nabla^2(\nabla^2\phi) \tag{3.24}$$

where ν is the viscous coefficient. The forcing term can be any physical function of position and time. It is of particular interest as it can be used to grow structures in the system. For example it can make drift waves appear in a steady plasma, which does not happen naturally in equation (3.22)[Connaughton et al., 2010].

In total the final CHM equation with viscosity and forcing terms is written

$$\frac{\partial}{\partial t}(\phi - {\nabla_\perp}^2\phi) - v_*\frac{\partial \phi}{\partial y} - [\phi, {\nabla_\perp}^2\phi] = -\nu\nabla^2(\nabla^2\phi) - f(x, y, t). \tag{3.25}$$

3.1.3 The Extended Hasegawa-Mima equation

While the CHM equation is appropriate for atmospheric physics, the coupling between global flows and surface fluctuations permitted by it is not a good model for plasmas in fusion devices. To improve the model it is possible to remove this coupling by writing the density response, equation (3.3), as

$$\frac{n_{i,e} - n_0}{n_0} = \frac{e}{T_e}(\phi - \delta_{s,1}\overline{\phi}), \tag{3.26}$$

where

$$\bar{\phi} = \frac{1}{L}\int_0^L \phi dy \tag{3.27}$$

is the surface averaged potential[Dorland et al., 1990; Smolyakov et al., 2000b,a; Manfredi et al., 2001; Dewar and Abdullatif, 2007] . $\delta_{s,1}$ is a Kronecker delta used

to select either the extended or non-extended versions of the equation. In the CHM case we use $s = 0$ and in the EHM case $s = 1$.

In this case we have

$$ln(n) = ln\left(n_0\left(1 + \frac{e(\tilde{\phi} + \delta_{s,0}\overline{\phi})}{T_e}\right)\right) \approx ln(n_0) + \frac{e(\tilde{\phi} + \delta_{s,0}\overline{\phi})}{T_e} \tag{3.28}$$

and equation (3.15) becomes

$$(\frac{\partial}{\partial t} + (\vec{v_E}\nabla))(\ln(n_0) + \frac{e(\tilde{\phi} + \delta_{s,0}\overline{\phi})}{T_e}) = \frac{1}{\omega_i B_0}(\frac{\partial}{\partial t}\nabla_\perp^2\phi + (\vec{v_E}\nabla)\nabla_\perp^2\phi). \tag{3.29}$$

Defining a stream function,

$$\Phi = \frac{\phi}{B_0},$$

rather than using the normalisations presented in the CHM derivation, equation (3.29) can be manipulated to give the Extended-Hasegawa-Mima (EHM) equation ,

$$(\frac{\partial}{\partial t} + v\vec{_E}\nabla + \vec{v_\star}\nabla)(\tilde{\Phi} + \delta_{s,0}\overline{\Phi}) - (\frac{\partial}{\partial t} + \vec{v_E}\nabla)\rho_s^2\nabla_\perp^2\Phi = 0, \tag{3.30}$$

where $\vec{v_\star}$ is now given by

$$\vec{v_\star} = -\frac{T_e\widehat{z} \times \nabla n_0}{eB_0 n_0} \tag{3.31}$$

and

$$\vec{v_E} = \widehat{z} \times \nabla\Phi.$$

Using a stream function rather than normalisation means that all quantities are measured in SI units, Φ itself then has units $\frac{m^2}{s}$. Using Poisson brackets the EHM equation can be written as

$$\frac{\partial}{\partial t}(\tilde{\Phi} + \delta_{s,0}\overline{\Phi} - \rho_s^2\nabla_\perp^2\Phi) + [\Phi, \tilde{\Phi} + \delta_{s,0}\overline{\Phi}] + v_\star\partial_y(\tilde{\Phi} + \delta_{s,0}\overline{\Phi}) - \rho_s^2[\Phi, \nabla^2\Phi] = 0 \tag{3.32}$$

where

$$v_\star = \rho_s^2\omega_i\frac{\partial ln(n_0)}{\partial x}. \tag{3.33}$$

As all of parameters are in SI units this means that $v_\star$ has units $\frac{m}{s}$ which is as expected as it represents the electron diamagnetic drift velocity[Dewar and Abdullatif, 2007].

3.1.4 Linear Dispersion Relation

Equation (3.32) can be linearised by assuming that all parts of the potential can be written in the form

$$\Phi(x,y,t) = \Phi_c + \varepsilon\Phi_1(x,y,t), \tag{3.34}$$

where Φ_c is a constant and ε is a small parameter. Remembering that the Poisson brackets denote taking gradients gives

$$\frac{\partial}{\partial t}\varepsilon(\tilde{\Phi}_1+\delta_{s,0}\overline{\Phi}_1-\rho_s^2\nabla_\perp^2\Phi_1)+[\varepsilon\Phi_1,\varepsilon\tilde{\Phi}_1+\varepsilon\delta_{s,0}\overline{\Phi}_1]+v_\star\partial_y\varepsilon(\tilde{\Phi}_1+\delta_{s,0}\overline{\Phi}_1)-\rho_s^2[\varepsilon\Phi_1,\varepsilon\nabla^2\Phi_1]=0. \tag{3.35}$$

Dropping terms $\mathcal{O}(\varepsilon^2)$ leaves a linear version of the EHM equation,

$$\frac{\partial}{\partial t}(\tilde{\Phi}_1+\delta_{s,0}\overline{\Phi}_1-\rho_s^2\nabla_\perp^2\Phi_1)+v_\star\partial_y(\tilde{\Phi}_1+\delta_{s,0}\overline{\Phi}_1)=0. \tag{3.36}$$

We have now removed any terms that provide a coupling between different waves, so we can assume plane wave solutions,

$$\Phi_1 = \Phi_{\vec{k}}e^{-i(\vec{k}.\vec{x}+\Omega_{\vec{k}}t)} \tag{3.37}$$

$$\overline{\Phi}_1 = \Phi_{\vec{k}}\delta_{\vec{k}y,0}e^{-i(\vec{k}.\vec{x}+\Omega_{\vec{k}}t)}. \tag{3.38}$$

Substituting these into equation (3.36) gives

$$-i\Omega_{\vec{k}}(\Phi_{\vec{k}}-\Phi_{\vec{k}}\delta_{\vec{k}y,0}+\delta_{s,0}\Phi_{\vec{k}}\delta_{\vec{k}y,0}+\rho_s^2k^2\Phi_{\vec{k}})-v_\star ik_y(\Phi_{\vec{k}}-\Phi_{\vec{k}}\delta_{\vec{k}y,0}+\delta_{s,0}\Phi_{\vec{k}}\delta_{\vec{k}y,0})=0 \tag{3.39}$$

which can be rearranged as

$$\Omega_{\vec{k}} = \frac{-v_\star k_y(1+\delta_{s,1}\delta_{k_y,0})}{1+\delta_{s,1}\delta_{k_y,0}+\rho_s^2k^2},$$

which, on considering the k_y in the numerator, becomes

$$\Omega_{\vec{k}} = \frac{-v_\star k_y}{1+\rho_s^2k^2}. \tag{3.40}$$

This is the linear dispersion relation for the Extended-Hasegawa-Mima equation. It is identical to the linear dispersion relation for the non-extended case and is entirely real, indicating that any change in the amplitude of waves in an unforced system is due to nonlinear interactions.

3.1.5 Fourier space representation

The Fourier transform of the potential is given by

$$\Phi = \sum_{\vec{k}} \Phi_{\vec{k}} e^{-i\vec{k}.\vec{x}} \tag{3.41}$$

and the surface averaged potential by

$$\bar{\Phi} = \frac{1}{2\pi} \sum_{\vec{k}} \Phi_{\vec{k}} \int_0^{2\pi} e^{-i\vec{k}.\vec{x}} dy = \sum_{\vec{k}} \Phi_{\vec{k}} \delta_{\vec{k}y,0} e^{-i\vec{k}.\vec{x}}. \tag{3.42}$$

These can be substituted into (3.30) and rearranged to give

$$\begin{aligned}\partial_t \sum_{\vec{k}} (1 - \delta_{k_y,0} + \delta_{s,0}\delta_{k_y,0} + \rho_s^2 k^2)\Phi_{\vec{k}} e^{-i\vec{k}.\vec{x}} - iv_\star \sum_{\vec{k}} (1 - \delta_{k_y,0} + \delta_{s,0}\delta_{k_y,0}) k_y \Phi_{\vec{k}} e^{-i\vec{k}.\vec{x}} \\ + \sum_{\vec{k_1},\vec{k_2}} \{ik_{1_x}\Phi_{\vec{k_1}} e^{-i\vec{k_1}.\vec{x}} ik_{2_y}(1 - \delta_{k_{2_y},0} + \delta_{s,0}\delta_{k_{2_y},0} + \rho_s^2 {k_2}^2)\Phi_{\vec{k_2}} e^{-i\vec{k_2}.\vec{x}} \\ -ik_{1_y}\Phi_{\vec{k_1}} e^{-i\vec{k_1}.\vec{x}} ik_{2_x}(1 - \delta_{k_{2_y},0} + \delta_{s,0}\delta_{k_{2_y},0} + \rho_s^2 {k_2}^2)\Phi_{\vec{k_2}} e^{-i\vec{k_2}.\vec{x}}\} = 0.\end{aligned} \tag{3.43}$$

Rewriting the nonlinear term gives

$$\begin{aligned}\partial_t \sum_{\vec{k}} (1 - \delta_{\vec{k_y},0} + \delta_{s,0}\delta_{\vec{k_y},0} + \rho_s^2 \vec{k}^2)\Phi_{\vec{k}} e^{-i\vec{k}.\vec{x}} \\ -iv_\star \sum_{\vec{k}} (1 - \delta_{\vec{k_y},0} + \delta_{s,0}\delta_{\vec{k_y},0}) \vec{k_y} \Phi_{\vec{k}} e^{-i\vec{k}.\vec{x}} \\ + \sum_{\vec{k}} \sum_{\vec{k_1},\vec{k_2}} (\vec{k_{1_y}} \vec{k_{2_x}} - \vec{k_{1_x}} \vec{k_{2_y}})((1 - \delta_{\vec{k_{2_y}},0} + \delta_{s,0}\delta_{\vec{k_{2_y}},0} + \rho_s k_2^2)\Phi_{\vec{k_1}} \Phi_{\vec{k_2}} \delta_{\vec{k},\vec{k_1}+\vec{k_2}} e^{-i\vec{k}.\vec{x}}) = 0.\end{aligned} \tag{3.44}$$

This can be simplified and rearranged to give

$$\begin{aligned}\partial_t \Phi_{\vec{k}} - \frac{iv_\star(1 - \delta_{k_y,0} + \delta_{s,0}\delta_{k_y,0})k_y}{(1 - \delta_{k_y,0} + \delta_{s,0}\delta_{k_y,0} + \rho_s^2 k^2)} \Phi_{\vec{k}} \\ + \sum_{\vec{k_1},\vec{k_2}} \frac{(k_{1_y}k_{2_x} - k_{1_x}k_{2_y})(1 - \delta_{k_{2_y},0} + \delta_{s,0}\delta_{k_{2_y},0} + \rho_s^2 {k_2}^2)}{(1 - \delta_{k_y,0} + \delta_{s,0}\delta_{k_y,0} + \rho_s^2 k^2)} \Phi_{\vec{k_1}} \Phi_{\vec{k_2}} \delta_{\vec{k},\vec{k_1}+\vec{k_2}} = 0,\end{aligned} \tag{3.45}$$

or

$$\partial_t \Phi_k + i\Omega_k - \Lambda^k_{k_1,k_2} \Phi_{k_1} \Phi_{\vec{k_2}} \delta_{\vec{k},\vec{k_1}+\vec{k_2}} = 0 \tag{3.46}$$

where Ω_k is given by equation (3.40) and

$$\Lambda^k_{k_1,k_2} = -\frac{(k_{1_y}k_{2_x} - k_{1_x}k_{2_y})(1 - \delta_{k_{2_y},0} + \delta_{s,0}\delta_{k_{2_y},0} + \rho_s^2 k_2^2)}{(1 - \delta_{k_y,0} + \delta_{s,0}\delta_{k_y,0} + \rho_s^2 k^2)}. \tag{3.47}$$

Next a symmetric version of the nonlinear coupling parameter $\Lambda^k_{k_1,k_2}$ is defined,

$$T(\vec{k},\vec{k_1},\vec{k_2}) = (\Lambda^k_{k_1,k_2}+\Lambda^k_{k_2,k_1}) = -\frac{(k_{1_y}k_{2_x} - k_{1_x}k_{2_y})(\rho_s^2(k_2^2-k_1^2)+\delta_{s,1}(\delta_{k_{1_y},0}-\delta_{k_{2_y},0}))}{(1+\rho_s^2k^2-\delta_{k_y,0}\delta_{s,1})}. \tag{3.48}$$

This leads to a representation of the EHM in Fourier space,

$$\partial_t\Phi_{\vec{k}} + i\Omega_{\vec{k}}\Phi_{\vec{k}} - \frac{1}{2}\sum_{\vec{k_1},\vec{k_2}} T(\vec{k},\vec{k_1},\vec{k_2})\Phi_{\vec{k_1}}\Phi_{\vec{k_2}}\delta_{\vec{k},\vec{k_1}+\vec{k_2}} = 0, \tag{3.49}$$

where the factor $\frac{1}{2}$ has been added to prevent modes being counted twice due the symmetrisation of $\Lambda^k_{k_1,k_2}$. As for the real space equation, all quantities are measured in SI units. The only new parameters are ω_k and $T(\vec{k},\vec{k_1},\vec{k_2})$ which have units s and m^{-2} respectively.

3.2 The Extended-Hasegawa-Wakatani Equation

3.2.1 Introduction

The Hasegawa-Wakatani[Hasegawa and Wakatani, 1983] model relaxes the adiabatic electron assumption of the Hasegawa-Mima equation and instead models parallel electron behaviour via electron dynamics in the direction parallel to the magnetic field. This leads to a two fluid model with coupled equations describing fluctuations of density and potential around a mean value. This system has a built in instability that, combined with the nonlinear terms, is capable of growing a broadband spectrum of drift waves. This is a much more 'physical' model as it can transition to a zonal flow state without the introduction of a specific initial condition. Here we will derive the Extended-Hasegawa-Wakatani model[Dorland and Hammett, 1993; Numata et al., 2007] . We use the term 'extended' to indicate the removal of the zonal components of density and potential from the current describing the electron dynamics parallel to the magnetic field. Further discussion of the benefits of the Hasegawa-Wakatani equations in comparison to the Hasegawa-Mima equation will be given in chapter 6.

3.2.2 Derivation

As with the Hasegaw-Mima equation we define a coordinate system where the $\widehat{z}$ direction is parallel to the magnetic field and the $\widehat{x}$ direction is along the density gradient. The $\widehat{y}$ direction is perpendicular to both $\widehat{z}$ and $\widehat{x}$ and corresponds to the

poloidal direction in a tokamak. We assume that the magnetic field is constant to give $\vec{B} = B_0\widehat{z}$. In order to simplify the equations we assume that ions are cold, $T_i = 0$, and the electron temperature is isothermal, $T_e = T =$ constant.

Perpendicular Ion Momentum

We begin by calculating the ion momentum perpendicular to the magnetic field. To do this we use the Braginskii equation for the conservation of momentum, equation (1.47). The cold ion assumption means that there is no pressure gradient. We neglect collisions and assume there are no sources, so that equation (1.47) becomes

$$mn\left(\partial_t + \vec{v} \bullet \nabla_\perp\right)\vec{v} = ne(-\nabla_\perp\phi + \vec{v} \times \vec{B}).$$

To find the lowest order velocity we set the left hand side to to 0, take the curl with $\vec{B}$ and use the vector identity

$$(\vec{c} \times \vec{b}) \times \vec{a} = (\vec{a} \bullet \vec{c})\vec{b} - (\vec{a} \bullet \vec{b})\vec{c}$$

to give

$$\begin{gathered} 0 = (-\nabla_\perp\phi + \vec{v} \times \vec{B}) \times \vec{B} \Rightarrow \\ 0 = \vec{B} \times \nabla_\perp\phi + (\vec{B} \cdot \vec{v})\vec{B} - (\vec{B}\vec{B})\vec{v} \Rightarrow \\ \vec{B} = B_0\hat{z}. \end{gathered}$$

As we are considering the perpendicular momentum, $\vec{B} \cdot \vec{v} = 0$ and therefore we obtain the $\vec{E} \times \vec{B}$ velocity

$$\vec{v_E} = \frac{\vec{B} \times \nabla_\perp\phi}{B_0^2} = \frac{\hat{z} \times \nabla_\perp\phi}{B_0}.$$

Substituting this back into the ion momentum equation in a procedure identical to that used for the Hasegawa-Mima equation gives

$$\vec{v}_{\perp,i} = \tfrac{m}{\mathrm{eB}_0^2}\{\partial_t(\nabla_\perp\phi) + (\overrightarrow{v_E}\nabla)(\nabla_\perp\phi)\} + \tfrac{1}{B_0}(\hat{z} \times \nabla_\perp\phi),$$

where the total perpendicular ion velocity $\vec{v}_{\perp,i}$ is the sum of the polarisation drift velocity,

$$\vec{v_p} = \frac{m}{\mathrm{eB}_0^2}\{\partial_t(\nabla_\perp\phi) + (\overrightarrow{v_E}\nabla)(\nabla_\perp\phi)\}$$

and the $\vec{E} \times \vec{B}$ velocity.

Perpendicular Electron Momentum

As for the perpendicular ion momentum, the perpendicular electron momentum is calculated from the Braginskii equation for conservation of momentum. We use the same assumptions as for the ion case, neglect electron inertia and keep a non-zero electron temperature to obtain

$$0 = -ne(-\nabla_\perp \phi + \vec{v} \times \vec{B}) - T\nabla_\perp n.$$

Taking the cross product with $\vec{B}$ as before, and neglecting the polarisation drift of the electrons due to their small mass gives

$$\overrightarrow{v}_{\perp,e} = \vec{v}_E - \frac{\hat{z} \times T\nabla_\perp n}{\mathrm{neB}_0} = \vec{v}_E + \vec{v}_{de}, \tag{3.50}$$

the final term, $\vec{v}_{de} = -\frac{\hat{z}\times T\nabla_\perp n}{\mathrm{neB}_0}$, is the electron diamagnetic drift velocity.

Parallel momentum

Electrons and ions can move freely in the direction of the magnetic field. The electron/ion mass ratio means that electrons move significantly faster than ions, which we therefore model as stationary, $v_{i,\parallel} = 0$. We use an electrostatic description of the electric field and model electron-ion collisions as

$$\eta e^2 n^2 (v_i - v_e) = -\eta e^2 n^2 \vec{v_{e\|}},$$

where η is a resistivity. The Braginskii momentum equation, (1.47), therefore becomes

$$0 = ne\nabla_\parallel \phi - T\nabla_\parallel n - \eta e^2 n^2 \vec{v}_{e\|},$$

which can be rewritten as a current density,

$$\vec{J}_\parallel = \frac{T}{e\eta}\left[\frac{\nabla_\parallel n}{n} - \frac{e\nabla_\parallel \phi}{T}\right]. \tag{3.51}$$

Continuity Equations

We now take the Braginskii continuity equation, (1.46), and substitute using the quantities derived above. Firstly, for electrons we have

$$\partial_t n + (\overrightarrow{v}_{\perp,e}\nabla_\perp)n + n(\nabla_\perp \overrightarrow{v}_{\perp,e}) - \tfrac{1}{e}\nabla_\parallel \vec{J}_\parallel = 0,$$

and, as $\nabla_\perp \cdot \overrightarrow{v}_E = 0$, $\nabla_\perp \cdot \overrightarrow{v}_{\rm de} = 0$ and $\vec{v}_{\rm de} \cdot \nabla n = 0$, this becomes

$$(\partial_t + \overrightarrow{v}_E \nabla_\perp) n - \tfrac{1}{e} \nabla_\parallel \vec{J}_\parallel = 0. \tag{3.52}$$

The ion continuity equation is obtained by following a similar procedure to the electron case but also neglecting $\vec{v}_p \nabla n$, the Braginskii continuity equation becomes

$$(\partial_t + \overrightarrow{v}_E \nabla_\perp) n + n \nabla_\perp \vec{v}_p = 0.$$

The continuity equations are are equated using quasineutrality, equation (1.7), to give

$$n \nabla_\perp \vec{v}_p = -\tfrac{1}{e} \nabla_\parallel \vec{J}_\parallel,$$

the left hand side of which can be expanded to

$$n \nabla_\perp \left(\tfrac{m}{\mathrm{eB}_0^2} \{ \partial_t (\nabla_\perp \phi) + (\overrightarrow{v_E} \nabla)(\nabla_\perp \phi) \} \right) = -\tfrac{1}{e} \nabla_\parallel \vec{J}_\parallel,$$

which can be rearranged as

$$(\partial_t + \overrightarrow{v_E} \nabla)(\nabla_\perp^2 \phi) = -\frac{\mathrm{eB}_0^2}{\mathrm{nm}} \frac{1}{e} \nabla_\parallel \vec{J}_\parallel. \tag{3.53}$$

Reduction

Further simplifications are now made to change to a completely two-dimensional system. First we say that n and ϕ are in fact fluctuations around a constant background:

$$n = n_0 + \tilde{n},$$
$$\phi = \phi_0 + \tilde{\phi}.$$

We also assume there is no background potential, $\phi_0 = 0$; the background density is constant, $\partial_t n_0 = 0$; and there is no background density gradient along the magnetic field, $\nabla_\parallel n_0 = 0$. This means that the parallel current equation can be rewritten as

$$\vec{J}_\parallel = \frac{T}{e\eta} \left[\frac{\nabla_\parallel \tilde{n}}{n_0} - \frac{e \nabla_\parallel \tilde{\phi}}{T} \right].$$

To close this set of equations, a parallel closure, that will allow us to calculate parallel gradients of n and phi, is needed. The simplest closure procedure considers a single monochromatic fluctuation, with wavevector k in the parallel direction, so that

$$\nabla_{\parallel}^2 = -k^2.$$

To simplify the notation **we now suppress the tildes**, hence,

$$\nabla_{\parallel}\vec{J}_{\parallel} = \frac{\mathrm{Tk}^2}{e\eta}\left[\frac{n}{n_0} - \frac{e\phi}{T}\right].$$

At this point we depart from the traditional HW derivation. We are interested in tokamaks, in which case the zonal components of density and potential do not contribute to the parallel current [Dorland and Hammett, 1993]. Therefore we write

$$\tilde{\phi} = \phi - <\phi>,$$
$$\tilde{n} = n - <n>,$$

where <> denotes an average in the poloidal direction, as given by equation (3.27), and $\tilde{\phi}$ **and ñ now represent the fluctuating potential and density with the surface averaged component removed.** This means that the parallel current gradient is

$$\nabla_{\parallel}\vec{J}_{\parallel} = \frac{\mathrm{Tk}^2}{e\eta}\left[\frac{\tilde{n}}{n_0} - \frac{e\tilde{\phi}}{T}\right]. \tag{3.54}$$

Using the slab geometry defined at the beginning of the derivation we write the density gradient as $\nabla_{\perp}n_0 = -\hat{x}\frac{n_0}{L_n}$ where L_n is the lengthscale of the gradient. This means that equations (3.52) and (3.53) can be written as

$$(\partial_t + \overrightarrow{v}_E\nabla_{\perp})(n_0 + n) - \tfrac{1}{e}\nabla_{\parallel}\vec{J}_{\parallel} = 0,$$
$$(\partial_t + \overrightarrow{v_E}\nabla)(\nabla_{\perp}^2\phi) = -\tfrac{B_0^2}{(n_0+n)m}\nabla_{\parallel}\vec{J}_{\parallel}$$

and expanded to

$$\partial_t n - \tfrac{1}{B_0}\partial_y\phi\partial_x n_0 + (\overrightarrow{v}_E\nabla_{\perp})n - \tfrac{1}{e}\nabla_{\parallel}\vec{J}_{\parallel} = 0, \tag{3.55}$$
$$\partial_t(\nabla_{\perp}^2\phi) + (\overrightarrow{v_E}\nabla)(\nabla_{\perp}^2\phi) = -\tfrac{B_0^2}{(n_0+n)m}\nabla_{\parallel}\vec{J}_{\parallel}. \tag{3.56}$$

Using Poisson brackets as defined in equation (3.23), substituting for $\nabla_{\parallel}\vec{J}_{\parallel}$

with equation (3.54), and rearranging gives

$$\partial_t \tfrac{n}{n_0} - \tfrac{1}{B_0}\tfrac{T}{e}\partial_y \tfrac{e\phi}{T}\tfrac{\partial_x n_0}{n_0} + \tfrac{T}{e}\tfrac{1}{B_0}\left[\tfrac{e\phi}{T}, \tfrac{n}{n_0}\right] - \tfrac{\mathrm{Tk}^2}{n_0 e^2 \eta}\left(\tfrac{\tilde{n}}{n_0} - \tfrac{e\tilde{\phi}}{T}\right) = 0,$$
$$\tfrac{T}{e}\partial_t\left(\nabla_\perp^2 \tfrac{e\phi}{T}\right) + \left(\tfrac{T}{e}\right)^2 \tfrac{1}{B_0}\left[\tfrac{e\phi}{T}, \nabla_\perp^2 \tfrac{e\phi}{T}\right] = -\tfrac{B_0^2}{n_0 m}\tfrac{\mathrm{Tk}^2}{e\eta}\left(\tfrac{\tilde{n}}{n_0} - \tfrac{e\tilde{\phi}}{T}\right).$$

The normalisations

$$\frac{e\phi}{T} \to \phi, \qquad \frac{e\tilde{\phi}}{T} \to \tilde{\phi}, \qquad \frac{n}{n_0} \to n, \qquad \frac{\tilde{n}}{n_0} \to \tilde{n}, \qquad \omega_{ci} t \to t, \qquad \frac{x, y}{\rho_s} \to x, y$$

and the definitions

$$\omega_{\mathrm{ci}} = \tfrac{\mathrm{eB_0}}{m}, \qquad \rho_s^2 = \frac{\mathrm{mT}}{e^2 B_0^2},$$

$$\alpha = \frac{\mathrm{Tk}^2}{n_0 e^2 \eta \omega_{\mathrm{ci}}}, \tag{3.57}$$

and

$$\kappa = -\frac{\partial \ln(n_0)}{\partial x} \tag{3.58}$$

leave us with

$$\partial_t n + \kappa \partial_y \phi + [\phi, n] - \alpha(\tilde{n} - \tilde{\phi}) = 0$$
$$\partial_t(\nabla_\perp^2 \phi) + [\phi, \nabla_\perp^2 \phi] = -\alpha(\tilde{n} - \tilde{\phi}).$$

Due to the normalisations used, all quantities in these equations are dimensionless, including α and κ. In the style of the Extended-Hasegawa-Mima equation (section 3.1.3) we define a switching parameter s to select the extended, $s = 1$, and non extended, $s = 0$, versions of the equations, which are finally written as

$$\partial_t n + \kappa \partial_y \phi + [\phi, n] - \alpha(n - \delta_{s,1} < n > -\phi + \delta_{s,1} < \phi >) = 0, \tag{3.59}$$
$$\partial_t(\nabla_\perp^2 \phi) + [\phi, \nabla_\perp^2 \phi] = -\alpha(n - \delta_{s,1} < n > -\phi + \delta_{s,1} < \phi >). \tag{3.60}$$

3.2.3 Fourier Space Representation

Writing the Fourier transforms of density and potential as

$$\phi = \sum_{\vec{k}} \Phi_{\vec{k}} e^{-i\vec{k}\cdot\vec{x}} \tag{3.61}$$

and

$$n = \sum_{\vec{k}} \mathcal{N}_{\vec{k}} e^{-i\vec{k}\cdot\vec{x}}, \tag{3.62}$$

along with their corresponding surface averages,

$$< \phi >= \frac{1}{2\pi} \sum_{\vec{k}} \Phi_{\vec{k}} \int_0^{2\pi} e^{-i\vec{k}\cdot\vec{x}} dy = \sum_{\vec{k}} \Phi_{\vec{k}} \delta_{k_y,0} e^{-i\vec{k}\cdot\vec{x}} \tag{3.63}$$

and

$$< n >= \frac{1}{2\pi} \sum_{\vec{k}} \mathcal{N}_{\vec{k}} \int_0^{2\pi} e^{-i\vec{k}\cdot\vec{x}} dy = \sum_{\vec{k}} \mathcal{N}_{\vec{k}} \delta_{k_y,0} e^{-i\vec{k}\cdot\vec{x}}, \tag{3.64}$$

leads to Fourier space versions of equations (3.59) and (3.60):

$$\partial_t \mathcal{N}_{\vec{k}} = -i(1+k^2)\Omega_k \Phi_{\vec{k}} + z\alpha(\Phi_{\vec{k}} - \mathcal{N}_{\vec{k}}) - \sum_{k_1,k_2} R(k_1,k_2) \Phi_{\overrightarrow{k_2}} \mathcal{N}_{\overrightarrow{k_1}} \delta_{\vec{k},\overrightarrow{k_1}+\overrightarrow{k_2}}, \tag{3.65}$$

$$\partial_t \Phi_{\vec{k}} = -\frac{\alpha z}{k^2}(\Phi_{\vec{k}} - \mathcal{N}_{\vec{k}}) - \sum_{k_3,k_4} T(k,k_3,k_4) \Phi_{\overrightarrow{k_3}} \Phi_{\overrightarrow{k_4}} \delta_{\vec{k},\overrightarrow{k_3}+\overrightarrow{k_4}}, \tag{3.66}$$

where $z = 1 - \delta_{s,1}\delta_{k_y,0}$.

The frequency and coupling parameters are

$$\Omega_k = \frac{\kappa k_y}{1+k^2}, \tag{3.67}$$

$$R(k_1,k_2) = (k_{1x}k_{2y} - k_{2x}k_{1y}), \tag{3.68}$$

and

$$T(k,k_3,k_4) = \frac{k_3^2(k_{3x}k_{4y} - k_{4x}k_{3y})}{k^2}. \tag{3.69}$$

In this case they are not symmetrised.

3.2.4 The Hasegawa-Wakatani linear dispersion relation

A linear dispersion relation can be obtained for the Extended-Hasegawa-Wakatani equations,(3.59) and (3.66), by considering potential and density as fluctuations around some constant value, hence,

$$\phi(x,y,t) = \phi_c + \varepsilon\phi_1(x,y,t), \tag{3.70}$$

$$n(x,y,t) = n_c + \varepsilon n_1(x,y,t), \tag{3.71}$$

$$< \phi(x,y,t) > = \phi_c + \varepsilon < \phi_1(x,y,t) >, \tag{3.72}$$

$$< n(x,y,t) > = n_c + \varepsilon < n_1(x,y,t) >, \tag{3.73}$$

where ε is a small parameter.

Substituting equations (3.70) to (3.73) into (3.59) gives

$$\partial_t(n_c + \varepsilon n_1) = -\kappa\partial_y(\varphi_c + \varepsilon\varphi_1) + \alpha(\varphi_c + \varepsilon\varphi_1 - \varepsilon\delta_{s,1} < \varphi_1 > -n_c - \varepsilon n_1 + \varepsilon\delta_{s,1} < n_1 >) + [n_c, \varphi_c] + [n_c, \varepsilon\varphi_1] + [\varepsilon n_1, \varphi_c] + [\varepsilon n_1, \varepsilon\varphi_1]. \tag{3.74}$$

Dropping terms $\mathcal{O}(\varepsilon^2)$ and simplifying leaves us with

$$\partial_t(\varepsilon n_1) = -\kappa\partial_y(\varepsilon\varphi_1) + \alpha(\varphi_c + \varepsilon\varphi_1 - \varepsilon\delta_{s,1} < \varphi_1 > -n_c - \varepsilon n_1 + \varepsilon\delta_{s,1} < n_1 >). \tag{3.75}$$

In the limit $\varepsilon \to 0$ we have $\phi_c \approx n_c$ and equation (3.75) becomes

$$\partial_t(n_1) = -\kappa\partial_y(\varphi_1) + \alpha(\varphi_1 - \delta_{s,1} < \varphi_1 > -n_1 + \delta_{s,1} < n_1 >). \tag{3.76}$$

Repeating the same procedure for the EHW potential equation, (3.60), gives

$$\partial_t(\nabla^2\varphi_1) = \alpha(\varphi_1 - \delta_{s,1} < \varphi_1 > -n_1 + \delta_{s,1} < n_1 >). \tag{3.77}$$

Using the single mode versions of (3.61) to (3.64), writing $\mathcal{N}_{\vec{k}} = N_{\vec{k}}e^{-i\omega t}$, $\Phi_{\vec{k}} = \varphi_{\vec{k}}e^{-i\omega t}$ and substituting into (3.76) and (3.77) gives

$$-i\omega N_k = -\,\mathrm{i}k_y\,\kappa\varphi_k + \alpha(\varphi_k - \varphi_k\delta_{s,1}\delta_{k_y,0} - N_k + N_k\delta_{s,1}\delta_{k_y,0}) \tag{3.78}$$

and

$$i\omega k^2\varphi_k = \alpha(\varphi_k - \varphi_k\delta_{s,1}\delta_{k_y,0} - N_k + N_k\delta_{s,1}\delta_{k_y,0}), \tag{3.79}$$

where the 1 subscript has been dropped. Rewriting each of these equations to contain $\frac{\varphi_k}{N_k}$ and substituting to eliminate this new term gives a dispersion relation for the extended Hasegawa-Wakatani system:

$$\omega^2k^2 - \mathrm{i}k_y\,\kappa\alpha + i\alpha\omega(k^2+1)(1 - \delta_{s,1}\delta_{k_y,0}) = 0. \tag{3.80}$$

This reduces to the normal Hasegawa-Wakatani dispersion relation when $s = 0$ or $k_y \neq 0$. The $\alpha \to \infty$ limit represents the recovery of an adiabatic electron response and reproduces the Hasegawa-Mima drift wave dispersion relation, equation (3.40). In fact, in this limit the EHW equations, (3.59) and (3.60), can be combined to produce the Extended-Hasegawa-Mima equation, (3.32).

Here, and in chapter 6, we will refer to (3.80) as the 'primary' dispersion

a) b)

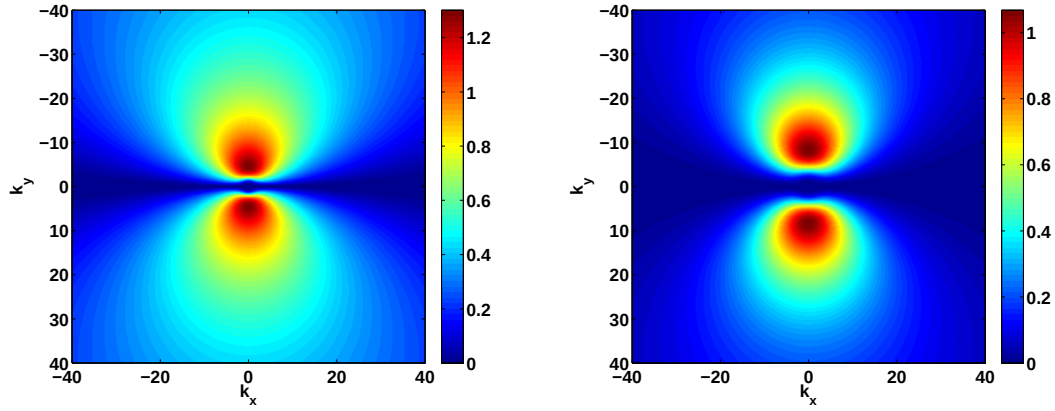

Figure 3.1: The imaginary part of ω when solving the EHW primary dispersion relation, equation (3.80), for a) $\alpha = 0.7,\ \kappa = 10$ and b) $\alpha = 10,\ \kappa = 10$.

relation and its associated growth rate and instability will also be labelled 'primary'.

An example is shown in figure 3.2.4, where the positive imaginary part of the solution to equation (3.80) is plotted for two different sets of parameters. Panel a) shows a case with a low value of α, where the parallel electron response is adiabatic, and panel b) shows a high α case. It can be seen that the dispersion relation has a similar shape for both cases and rapidly decays with k. However, the high α case is centred around a higher value of k_y. Equation (3.80) is a quadratic and has solutions

$$\omega = \frac{-i\alpha(k^2+1)(1-\delta_{s,1}\delta_{k_y,0}) \pm \sqrt{-\alpha^2(k^2+1)^2(1-\delta_{s,1}\delta_{k_y,0}) - 4i\kappa\alpha k^2 k_y}}{2k^2}. \quad (3.81)$$

An important feature is that both cases in figure 3.2.4 show no growth for $k_y = 0$. In this situation the extended version of equation (3.81) indicates $\omega = 0$ and the non-extended version gives a decaying solution,

$$\omega = \frac{-i\alpha(k_x^2+1)}{k_x^2}.$$

This demonstrates that this primary instability can not grow zonal modes, which are defined to have $k_y = 0$ in our slab model, therefore nonlinear processes must be involved in the generation of zonal flows in the Hasegawa-Wakatani system.

3.3 Summary

This chapter has introduced the two reduced models of plasma turbulence that will be used throughout this work, namely the Extended-Hasegawa-Mima and Extended-Hasegawa-Wakatani equations. They have been written in such a way that the non-extended versions can be easily recovered by changing a simple switching parameter, s. The numerical codes developed to solve these equations, discussed in chapter 4, and the analytical models described in chapters 5 to 7 also include this switching parameter and can therefore be used to study both the extended and non-extended systems.

The Fourier space version of the equations was also presented. This is used in the derivation of the four-mode truncated models presented later. Finally, the dispersion relations for each system of equations was derived. These show how a drift wave in the Extended-Hasegawa-Mima system is stable and will simply propagate, whereas the Extended-Hasegawa-Wakatani equations will linearly grow unstable drift waves. It was also highlighted that this primary instability in the EHW equations cannot grow zonal flows. In both system they must be produced by secondary instabilities such as cascades or resonant interactions. Four-mode truncated models are derived in 5 to 7 to study these resonant interactions.

Chapter 4

Numerical Methods

4.1 Introduction

One of the reasons for using the reduced models discussed in section 3 is the relative simplicity with which they can be solved numerically. Nevertheless to ensure a stable code that produces accurate results a number of techniques must be used. These are discussed in this chapter, along with a summary of how they are combined for use in the pseudospectral codes used later.

In general the Haseagawa-Mima and Hasegawa-Wakatani equations have the form

$$\frac{d}{dt}u = f(u, \frac{du}{dx}, \frac{du}{dy}), \tag{4.1}$$

where $f(u, \frac{du}{dx}, \frac{du}{dy})$ is a nonlinear function. Here we use finite difference techniques to evolve the quantity 'u' in time. The derivations given in chapter 3 are for a two dimensional Cartesian system and therefore the quantities being evolved are represented on a two-dimensional grid. Each cell in the grid is labelled with indices i and j, representing the x and y directions respectively.

Under this finite difference approximation time derivatives must also be discretised, equation (4.1) is then written

$$\frac{u_{i,j}^{n+1} - u_{i,j}^{n}}{\Delta t} = f(u_{i,j}^{n}, \frac{du_{i,j}^{n}}{di}, \frac{du_{i,j}^{n}}{dj}), \tag{4.2}$$

where superscript n represents the value at the current time and Δt is the small time increment between time n and time $n+1$. This however is potentially numerically unstable and solving it directly will produce solutions that grow exponentially, this is discussed further in section 4.2 and a stable time integration solution is presented in section 4.4. To discretise spatial derivatives, centred difference approximations

are used, in this case

$$\frac{\partial}{\partial x}u$$

becomes

$$\frac{u^n_{i+1,j} - u^n_{i-1,j}}{2\Delta x}$$

where Δx is the space between grid points in the x direction. The two-dimensional Laplacian,

$$\nabla^2 u$$

becomes

$$\frac{1}{\Delta^2}(u^n_{i+1,j} + u^n_{i-1,j} - 4u^n_{i,j} + u^n_{i,j+1} + u^n_{i,j-1}),$$

where we have assumed that the grid spacing is the same in the x and y directions to give $\Delta = \Delta x = \Delta y$.

The nonlinear spacial derivatives, the Poisson bracket terms, cannot be represented so simply. They are discussed in section 4.5.

4.2 The Courant-Friedrichs-Lewy condition

von Neumann Stability

When writing finite difference codes the stability of a particular numerical solution must always be considered. This is a complex subject and here we restrict ourselves to demonstrating the problem using von Neumann stability analysis with a simple example based on [Press, 1988].

A general one dimensional flux conservative equation,

$$\frac{\partial p(y,t)}{\partial t} = -\nu \frac{\partial p(y,t)}{\partial y}, \tag{4.3}$$

can be written in finite difference form as

$$\frac{p^{n+1}_j - p^n_j}{dt} = -\nu \left(\frac{p^n_{j+1} - p^n_{j-1}}{2dy} \right). \tag{4.4}$$

This is known as the forward time centred space (FTCS) approximation. Von Neumann stability analysis makes the assumption that the eigenmodes of a finite difference equation are of the form

$$p^n_j = \varepsilon(k)^n e^{\mathrm{i}kjdy},$$

where ε is an amplification factor and, for this example, $\mathrm{i} = \sqrt{-1}$ rather than a grid index. It can easily be seen that if $|\varepsilon(k)| > 1$, p will grow as n increases. This is what is meant by instability, for example, using this definition and solving equation (4.4) for $\varepsilon(k)$ gives

$$\varepsilon(k) = 1 - \mathrm{i}\frac{\nu dt}{dx}\sin(kdy),$$

whose modulus is greater than one for all k. This means that any attempt to solve this equation using the FTCS finite differencing scheme will result in a solution which grows exponentially. In practice this means that the FTCS is never used for numerical integration as numerous other integration schemes with better stability properties exit. The precise scheme used in this work for the time integration of the Hasegawa-Mima and Hasegawa-Wakatni equations will be described in section 4.4.

The CFL condition

The Courant-Friedrichs-Lewy (CFL) condition is a condition which must normally be met to ensure stability in explicit numerical schemes. For an N dimensional flux conservative problem on a square grid the CFL condition can be written[Press, 1988, p.663]

$$dt \leq \frac{\Delta}{\sqrt{N}|\nu|} \tag{4.5}$$

where the grid is made of cells of size $\Delta \times \Delta$. It appears in the stability analysis of many finite difference schemes, and is a statement that information must not propagate at such a rate that it is unavailable to a certain grid point when needed. The fastest information can propagate in a flux conservative equation such as (4.3) is ν, so ensuring the inequality in equation (4.5) is true means that in a single time step dt, information can only move by one grid point.

This is in fact an oversimplification as the precise conditions for stability depend on the specific equation and finite differencing scheme being used. However, it is a good guideline for deciding on step size. The codes used in this work use it as a safety check on the largest permissible time step size with ν replaced by $v\star$, equation 3.31, and κ, equation 3.58 for the EHM and EHW cases respectively.

4.3 Numerical schemes

4.3.1 Explicit schemes

Explicit schemes for solving differential equations are those that solve equation (4.1) by approximating it as

$$\frac{u^{n+1} - u^n}{dt} = f(u^n),$$

which can be rearranged to give

$$u^{n+1} = u^n + dt * f(u^n).$$

In this type of scheme all the information needed to calculate the value at time $n+1$ is known at the current time n. While this is perhaps the most straightforward scheme to use is suffers from problems with numerical stability. To get an accurate result in highly nonlinear systems this can require the use of an infeasibly small timestep dt.

4.3.2 Implicit schemes

Implicit schemes avoid problems with numerical stability by calculating the right hand side of (4.1) at timestep $n + 1$. This results in an equation of the form

$$u^{n+1} - dt * f(u^{n+1}) = u^n.$$

Rather than a straightforward iteration as was necessary for the explicit case, this involves solving a linear algebra problem at each timestep. This can be seen by rewriting the left hand side as an operator, A, to give

$$Au^{n+1} = u^n.$$

For a two dimensional finite difference code, u becomes a vector describing values at each grid point and A becomes a matrix describing the gradients taken. This shows the shortcoming of implicit schemes, they are unconditionally stable[Press, 1988] but often involve inverting large matrices at each timestep. Fortunately, matrix inversion is a common problem in physics and mathematics and a number of techniques have been developed to expedite it. The method used for this work will be described in section 4.6.

4.3.3 Pseudospectral schemes

Spectral schemes solve equation (4.1) by transforming to Fourier space so that $u(\vec{x}) \rightarrow u(\vec{k})$ where $\vec{k}$ is a wavevector. Linear terms are represented as $F(k) * u(k)$ where gradients are simply k raised to an appropriate power, these can be solved very rapidly. However, nonlinear terms will involve a complex coupling parameter that can potentially involve summing contributions from all mode numbers. Such a sum is difficult to parallelise effectively and calculating it can outweigh the performance increase gained by the simplicity of the linear terms.

Pseudospectral schemes aim to get the best performance by evaluating linear terms and timesteps in Fourier space whilst evaluating nonlinear terms directly in real space. Fast Fourier transforms are used to combine the real and Fourier space calculations. The pseudospectral scheme used for this work will be discussed in section 4.4.

4.4 The Karniadakis method

The Karniadakis method[Karniadakis et al., 1991] was initially developed for the incompressible Navier-Stokes equations. The Karniadakis recursion relation for solving Navier-Stokes style equations is given by

$$\frac{\gamma_0 \overrightarrow{v}^{n+1} - \sum_{q=0}^{J_i-1} \alpha_q \overrightarrow{v}^{n-q}}{\Delta t} = -\nabla p^{n+1} + \sum_{q=0}^{J_i-1} \beta_q \overrightarrow{N}(\overrightarrow{v}^{n-q}) + \nu \overrightarrow{L}(\overrightarrow{v}^{n+1}) \qquad (4.6)$$

where $\overrightarrow{v}$ is the velocity vector describing the flow of a fluid element, J_i is the order to which the equation is being solved, γ_0, α_q and β_q are numerical coefficients given in Table 4.1.

In the codes written for this work, $\vec{v}$ is replaced by the quantities being differentiated with respect to time in equations (3.32), (3.59) and (3.60). There are no pressure gradients in the EHM or EHW equations so the ∇p term is dropped and $\vec{N}$ is replaced with finite difference representations of the gradients in the system. Poisson brackets are evaluated using the technique discussed in section 4.5. Linear dissipation and the additional forcing added in chapter 7 replace the final term in equation (4.6).

It should be noted here that the $\vec{L}$ term is evaluated at timestep $n+1$, therefore its inclusion requires implicit techniques to advance the numerical solution. This means that the terms under summations are evaluated in real space, whereas

Coefficient	1st order	2nd Order	3rd Order
γ_0	1	3/2	11/6
α_0	1	2	3
α_1	0	-1/2	-3/2
α_2	0	0 1/3	
β_0	1	2	3
β_1	0	-1	-3
β_2	0	0	1

Table 4.1: Coefficients for use in the Karniadakis method

dissipation and the time step is done in Fourier space using spectral methods. Fast Fourier transforms are used to change between real and Fourier space as needed.

4.5 The Arakawa Poisson bracket

The problem with Poisson brackets in finite difference algorithms is that when written directly in finite difference form they are inherently unstable. The solution breaks down in to long thin eddies that are only a few grid spacings in size[Arakawa, 1966].

In order to avoid this it is necessary to specially design a finite difference expansion for Poisson brackets. In [Arakawa, 1966] three finite difference representations of a Poisson brackets are derived, $J(A,B)^{++}$, $J(A,B)^{\times +}$ and $J(A,B)^{+\times}$. The previous definition of a Poisson bracket, equation (3.23), is related to $J(A,B)$ via $J(A,B) = [A,B]$.

Each of the forms of J meet a necessary requirement of a Poisson bracket,

$$J(A,B)^{++} \text{ satisfies } J(A,B) = -J(B,A),$$

$$J(A,B)^{\times +} \text{ conserves square vorticity, and}$$

$$J(A,B)^{+\times} \text{ conserves kinetic energy.}$$

To satisfy all of the requirements the various forms can be combined as

$$\frac{1}{3}\left\{J(A,B)^{++} + J(A,B)^{+\times} + J(A,B)^{\times +}\right\}$$

to give

$$J_{i,j} = \tag{4.7}$$
$$\frac{1}{12\Delta^2}\{(A_{i+1,j} - A_{i-1,j})(B_{i,j+1} - B_{i,j-1}) - (A_{i,j+1} - A_{i,j-1})(B_{i+1,j} - B_{i-1,j})$$
$$+ A_{i+1,j}(B_{i+1,j+1} - B_{i+1,j-1}) - A_{i-1,j}(B_{i-1,j+1} - B_{i-1,j-1})$$
$$- A_{i,j+1}(B_{i+1,j+1} - B_{i-1,j+1}) + A_{i,j-1}(B_{i+1,j-1} - B_{i-1,j-1})$$
$$+ A_{i+1,j+1}(B_{i,j+1} - B_{i+1,j}) - A_{i-1,j-1}(B_{i-1,j} - B_{i,j-1})$$
$$- A_{i-1,j+1}(B_{i,j+1} - B_{i-1,j}) + A_{i+1,j-1}(B_{i+1,j} - B_{i,j-1})\}$$

where the i,j subscript denotes a value at gridpoint i,j. This is the form used in the numerical codes developed for this work.

4.6 Fourier Decomposition

To solve the final timestep of the Karniadakis method Fourier decomposition[Potter, 1973, p.92] is used. To demonstrate this we first rewrite equation (4.6). Dropping the pressure term and rearranging gives

$$\gamma_0 \overrightarrow{v}^{n+1} - \nu\Delta t \overrightarrow{L}(\overrightarrow{v}^{n+1}) = \sum_{q=0}^{J_i-1} \alpha_q \overrightarrow{v}^{n-q} + \Delta t \sum_{q=0}^{J_i-1} \beta_q \overrightarrow{N}(\overrightarrow{v}^{n-q}), \tag{4.8}$$

the right hand side of which relies on information from the current and previous timesteps and is therefore known. For simplicity we rewrite it as a source term. Explicitly writing out the gridpoint indices, equation (4.8) becomes

$$\gamma_0 v_{i,j}^{n+1} - \nu L(v_{i,j}^{n+1}) = S_{i,j}, \tag{4.9}$$

which can be written as

$$P v_{i,j}^{n+1} = S_{i,j}, \tag{4.10}$$

where P is an operator describing the left hand side of (4.8).

To describe Fourier synthesis we now switch to the CHM case and neglect any linear forcing or damping described by the L term, the numerical code used in this work then evolves the quantity $\phi - \rho_s^2\nabla^2\phi$ in time. The finite difference representation of this is

$$-\frac{\rho_s^2}{\Delta^2}(\phi_{i+1,j} + \phi_{i-1,j} - 4\phi_{i,j} + \phi_{i,j+1} + \phi_{i,j-1}) + \phi_{i,j},$$

which means that we can write (4.10) as

$$-\rho_s^2(\phi_{i+1,j}^{n+1}+\phi_{i-1,j}^{n+1}-4\phi_{i,j}^{n+1}+\phi_{i,j+1}^{n+1}+\phi_{i,j-1}^{n+1})+\Delta^2\phi_{i,j}^{n+1}=\Delta^2 S_{i,j}^n, \tag{4.11}$$

where S is the source term described earlier. The left hand side of (4.11) is used to define P, it is the operator that gives

$$P\phi_{i,j}=-\rho_s^2(\phi_{i+1,j}+\phi_{i-1,j}-4\phi_{i,j}+\phi_{i,j+1}+\phi_{i,j-1})+\Delta^2\phi_{i,j},$$

and we therefore have

$$P\phi_{i,j}^{n+1}=\Delta^2 S_{i,j}^n. \tag{4.12}$$

P can then be applied to the double Fourier harmonic[Potter, 1973],

$$s_{i,j}(k,l)=\hat{\phi}(k,l)sin(\frac{\pi kj}{J})sin(\frac{\pi li}{I}), \tag{4.13}$$

where I and J are the maximum values of i and j. This gives

$$Ps_{i,j}(k,l)=\alpha_{k,l}s_{i,j}(k,l), \tag{4.14}$$

where α is an eigenvalue given by

$$\alpha_{k,j}=\rho_s^2(2cos(\frac{\pi l}{I})+2cos(\frac{\pi k}{J}-4))-2\Delta^2.$$

Using the transform

$$F(\phi_{i,j})=\sum_{i,j}\hat{\phi}(k,l)sin(\frac{\pi kj}{J})sin(\frac{\pi li}{I})=\sum_{i,j}s_{i,j}$$

and

$$F(S_{i,j})=\sum_{i,j}\hat{S}(k,l)sin(\frac{\pi kj}{J})sin(\frac{\pi li}{I}),$$

equation (4.12) indicates

$$PF(\phi_{i,j})=P\sum_{i,j}s_{i,j}=\Delta^2F(S_{i,j}).$$

This means that, for each individual mode, the value of $\hat{\phi}(k,l)^{n+1}$ can be calculated as

$$\hat{\phi}(k,l)^{n+1}=\frac{\Delta^2\hat{S}(k,l)^n}{\alpha_{k,j}}. \tag{4.15}$$

Different sets of boundary conditions will require a different sets of Fourier harmonics. A different operator P will lead to different eigenvalues ($\alpha_{k,j}$), as will including the linear term L. Each equation solved by the numerical codes used in this work has had the relevant formula for eigenvalues calculated analytically.

The steps listed above are a demonstration of the mathematics behind the Fourier decomposition technique. In practice $\hat{S}^n$ is calculated from S using a fast Fourier transform library, then equation (4.15) is solved for $\hat{\phi}^{n+1}$, and finally an inverse fast Fourier transform is used to find ϕ^{n+1}.

4.7 Summary

The techniques listed above were used to create C++ codes for solving the extended and non-extended versions of the Hasegawa-Mima and Hasegawa-Wakatani equations. The combination of the Arakawa Poisson bracket and the Karniadakis time stepping technique was described in [Naulin, 2003] and tested in [Naulin and Nielsen, 2003], a detailed discussion is given in [Scott, 2008]. Throughout this work they will referred to as 'full simulations' or 'partial differential equation (PDE) simulations'. Both codes have been parallelised using a message passing interface (MPI) library.

The basic structure of the two codes is identical, first the initial values needed to set up the simulations is read from a setup file, this includes constants from the equations as well as constants relevant to the code such as the timestep and grid spacing. All the PDE simulations in this work were carried on on a square domain discretised into 512x512 grid spaces. For the EHM equations solved in chapter 5 the box had sides of length 2π, with the domain running from $-\pi$ to π. As the Larmor radius is retained in this chapter the length scales are in SI units. The smallest Larmor radius investigated is $\rho_s = 0.35m \sim 0.06L$ where L is the length of the box, it is approximately 30 times larger than the grid spacing. The largest Larmor radius investigated is $\rho_s = 4m \sim 0.64L$ In chapters 6 and 7, simulations of the Extended-Hasegawa-Wakatani and driven-Hasegawa-Mima equations respectively, the domain ran from -20 to 20 and lengths were normalised to the Larmor radius. In chapter 6 time was normalised to ω_i. The initial values for potential and density can be read in from an input file, or, in the case of the modulational instability used in chapter 5, specified in the first setup file.

Once the initial setup is complete quantities that are not part of the time derivative term in equations (3.32) or (3.59) and (3.60) are calculated. Nonlinear terms are calculated using the Arakawa method described in section 4.5. These

newly calculated values are added to versions calculated on the previous time step to calculate the terms under summations in the Karnadakis method, equation (4.6) and hence the source term in equation (4.9).

A fast Fourier transform is then applied to the source term to calculate its k-space representation. The Fourier-decomposition technique described in section 4.6 is then used to step the solution forward in time , find values of potential from vorticity, and in the Hasegawa-Wakatani case, density. An inverse fast Fourier transform is used to calculate new values in real space.

Finally pointers to arrays are moved to store data for use as 'previous timesteps' in the Karniadakis method. Output files are generated as specified in the initial setup file and the process is repeated.

Aliasing is not a problem due to the nature of the simulations performed. In 5 the system is initialised with modes that all have $k \ll \frac{512}{2}$. Even though resonant interactions and energy cascades can produce modes with larger k values, these do not approach the $\frac{512}{2}$ before the simulation is stopped and aliasing is therefore not a concern. For the simulations performed in chapters 6 and 7 the instability and driving profile drops off rapidly with $|k|$ and therefore only causes the growth of modes with $k \ll \frac{512}{2}$. However, as these systems are initialised with white noise, viscosity is applied to suppress higher mode numbers.

Chapter 5

The Modulational Instability in the Hasegawa-Mima System

5.1 Introduction

It has long been known that the modulational instability (MI) provides a mechanism by which a plasma can transition from drift wave dominated turbulence to a zonal flow[Chen et al., 2000]. Non-local interactions transfer energy from a driving drift wave to modes with k-numbers in the zonal direction via resonant interactions in the presence of one or more 'sidebands'. In tokamaks this is investigated using techniques such as heavy ion beam probes, Langmuir probes and beam emission spectroscopy[Fujisawa, 2009]. Statistical analysis techniques such as averaged bispectra are then used to analyse the data. For example, Langmuir probes have been used to measure the velocity power spectrum at the edge of the HT-7 tokamak. A low freqency peak can be found indicating a zonal flow[Fujisawa, 2009]. For further examples see [Fujisawa, 2009; Diamond et al., 2000; van Milligen et al., 1995]. The other approach is the use of numerical simulations where the time and length scales of interest are directly accessible. Here, we do this using a pseudospectral code that was developed to solve the Extended-Hasegawa-Mima equation, as described in chapter 4.

The EHM system was chosen as a model of plasma behaviour as it contains enough physics to investigate the transition from drift wave dominated turbulence to zonal flows, yet is simple enough to allow an analytical investigation. This simplicity however has its shortcomings; drift waves do not develop naturally in simulations and therefore must be introduced as an initial condition.

This chapter begins with an analytical investigation of the Extended-Hasegawa-

Mima equation. A simplification is made where the system is truncated to contain only the four modes necessary to create a modulational instability, this is a common procedure for investigating the MI, for examples see[Manfredi et al., 2001; Lashmore-Davies et al., 2001; Guzdar et al., 2001; McCarthy et al., 2004] . Under this this assumption a series of ODEs are developed to model the behaviour of the driving wave, zonal perturbation and sidebands.

A linearised version of the ODEs is then used to produce a dispersion relation from which a prediction of the growth rate of the zonal mode can be calculated. At the end of the chapter the pseudospectral code is used to investigate the effect of varying ρ_s and the behaviour of 'off-zonal' perturbations. Comparisons are made with the analytical models derived at the start of the chapter.

5.2 A truncated four-mode system

To derive the four-mode truncated (4MT) system describing the modulational instability we use the EHM system but define $\Phi_{\vec{k}}$ as a sum of four modes, $\vec{p}$,$\vec{q}$,$\vec{p_+}$,$\vec{p_-}$, where

$$\Phi_{\vec{k}} = \phi_{\vec{p}}\left(t\right)\delta_{\vec{k},\vec{p}} + \phi_{\vec{q}}\left(t\right)\delta_{\vec{k},\vec{q}} + \phi_{\vec{p_+}}\left(t\right)\delta_{\vec{k},\vec{p_+}} + \phi_{\vec{p_-}}\left(t\right)\delta_{\vec{k},\vec{p_-}} \tag{5.1}$$

and

$$\vec{p_\pm} = \vec{p} \pm \vec{q}. \tag{5.2}$$

It should be noted that when initialising the PDE simulations the waves were initialised in real space with $\Phi_{\vec{k}}(\vec{x}) = A_{\vec{k}} sin(\frac{2\pi}{L}\vec{k}\vec{x})$, so $\vec{k}$ represents integer wave numbers.

These modes can then be substituted in to equation (3.49) to give

$$\begin{aligned}\partial_t\phi_{\vec{p}}\left(t\right)\delta_{\vec{k},\vec{p}} + \partial_t\phi_{\vec{q}}\left(t\right)\delta_{\vec{k},\vec{q}} + \partial_t\phi_{\vec{p_+}}\left(t\right)\delta_{\vec{k},\vec{p_+}} + \partial_t\phi_{\vec{p_-}}\left(t\right)\delta_{\vec{k},\vec{p_-}} = \\ - i\Omega_{\vec{k}}\left(\phi_{\vec{p}}\left(t\right)\delta_{\vec{k},\vec{p}} + \phi_{\vec{q}}\left(t\right)\delta_{\vec{k},\vec{q}} + \phi_{\vec{p_+}}\left(t\right)\delta_{\vec{k},\vec{p_+}} + \phi_{\vec{p_-}}\left(t\right)\delta_{\vec{k},\vec{p_-}}\right) \\ + \frac{1}{2}\sum_{\vec{k_1},\vec{k_2}} T\left(\vec{k},\vec{k_1},\vec{k_2}\right)\phi_{\vec{k_2}}\left(t\right)\phi_{\vec{k_1}}\left(t\right)\delta_{\vec{k},\vec{k_1}+\vec{k_2}}.\end{aligned} \tag{5.3}$$

Then with $\vec{k}$ defined as each of the four modes in the system in turn, the sum is expanded over the four modes and their counter-propagating solutions for both $\vec{k_1}$ and $\vec{k_2}$. Most of the terms produced will be zero due to either the Kronecker

Delta or cancellations in the coupling parameter,

$$T(\vec{k},\vec{k_1},\vec{k_2}) = -\frac{(k_{1_y}k_{2_x} - k_{1_x}k_{2_y})(\rho_s^2(k_2^2 - k_1^2) + \delta_{s,1}(\delta_{k_{1_y},0} - \delta_{k_{2_y},0}))}{(1 + \rho_s^2 k^2 - \delta_{k_y,0}\delta_{s,1})}, \tag{5.4}$$

leaving the following equations

$$\begin{aligned}
\partial_t \phi_{\vec{p}}(t) &= T\left(\vec{p},\vec{p_-},\vec{q}\right)\phi_{\vec{q}}(t)\,\phi_{\vec{p_-}}(t) \\
&\quad + T\left(\vec{p},\vec{-q},\vec{p_+}\right)\phi_{\vec{p_+}}(t)\,\phi_{\vec{-q}}(t) - i\Omega_{\vec{p}}\phi_{\vec{p}}(t) && (5.5)\\
\partial_t \phi_{\vec{q}}(t) &= T\left(\vec{q},-\vec{p_-},\vec{p}\right)\phi_{\vec{p}}(t)\,\phi_{-\vec{p_-}}(t) \\
&\quad + T\left(\vec{q},-\vec{p},\vec{p_+}\right)\phi_{\vec{p_+}}(t)\,\phi_{-\vec{p}}(t) - i\Omega_{\vec{q}}\phi_{\vec{q}}(t) && (5.6)\\
\partial_t \phi_{\vec{p_+}}(t) &= T\left(\vec{p_+},\vec{q},\vec{p}\right)\phi_{\vec{p}}(t)\,\phi_{\vec{q}}(t) - i\Omega_{\vec{p_+}}\phi_{\vec{p_+}}(t) && (5.7)\\
\partial_t \phi_{\vec{p_-}}(t) &= T\left(\vec{p_-},-\vec{q},\vec{p}\right)\phi_{\vec{p}}(t)\,\phi_{-\vec{q}}(t) - i\Omega_{\vec{p_-}}\phi_{\vec{p_-}}(t) && (5.8)
\end{aligned}$$

Using the definition $\phi_{\vec{k}} = \psi_{\vec{k}}(t)e^{-i\Omega_{\vec{k}}t}$ and its conjugate $\overline{\phi_{\vec{k}}} = \overline{\psi_{\vec{k}}}(t)e^{i\Omega_{\vec{k}}t}$ equations (5.5) to (5.8) can be expanded to

$$\begin{aligned}
&\mathrm{e}^{-i\Omega_{\vec{p}}t}\partial_t\psi_{\vec{p}}(t) - \psi_{\vec{p}}(t)\,i\Omega_{\vec{p}}\mathrm{e}^{-i\Omega_{\vec{p}}t} = && (5.9)\\
&T\left(\vec{p},\vec{p_-},\vec{q}\right)\psi_{\vec{q}}(t)\,\mathrm{e}^{-i\Omega_{\vec{q}}t}\psi_{\vec{p_-}}(t)\,\mathrm{e}^{-i\Omega_{\vec{p_-}}t} + T\left(\vec{p},-\vec{q},\vec{p_+}\right)\psi_{\vec{p_+}}(t)\,\mathrm{e}^{-i\Omega_{\vec{rp}}t}\overline{\psi_{\vec{q}}(t)}\mathrm{e}^{i\Omega_{\vec{q}}t}\\
&-\psi_{\vec{p}}(t)\,i\Omega_{\vec{p}}\mathrm{e}^{-i\Omega_{\vec{p}}t},
\end{aligned}$$

$$\begin{aligned}
&\mathrm{e}^{-i\Omega_{\vec{q}}t}\partial_t\psi_{\vec{q}}(t) - \psi_{\vec{q}}(t)\,i\Omega_{\vec{q}}\mathrm{e}^{-i\Omega_{\vec{q}}t} = && (5.10)\\
&T\left(\vec{q},-\vec{p_-},\vec{p}\right)\psi_{\vec{p}}(t)\,\mathrm{e}^{-i\Omega_{\vec{p}}t}\overline{\psi_{\vec{p_-}}(t)}\mathrm{e}^{i\Omega_{\vec{p_-}}t} + T\left(\vec{q},-\vec{p},\vec{p_+}\right)\psi_{\vec{p_+}}(t)\,\mathrm{e}^{-i\Omega_{\vec{p_+}}t}\overline{\psi_{\vec{p}}(t)}\mathrm{e}^{i\Omega_{\vec{p}}t}\\
&-\psi_{\vec{q}}(t)\,i\Omega_{\vec{q}}\mathrm{e}^{-i\Omega_{\vec{q}}t},
\end{aligned}$$

$$\begin{aligned}
&\mathrm{e}^{-i\Omega_{\vec{p_+}}t}\partial_t\psi_{\vec{p_+}}(t) - \psi_{\vec{p_+}}(t)\,i\Omega_{\vec{p_+}}\mathrm{e}^{-i\Omega_{\vec{p_+}}t} = T\left(\vec{p_+},\vec{q},\vec{p}\right)\psi_{\vec{p}}(t)\,\mathrm{e}^{-i\Omega_{\vec{p}}t}\psi_{\vec{q}}(t)\,\mathrm{e}^{-i\Omega_{\vec{q}}t}\\
&-\psi_{\vec{p_+}}(t)\,i\Omega_{\vec{p_+}}\mathrm{e}^{-i\Omega_{\vec{p_+}}t}, && (5.11)
\end{aligned}$$

$$\begin{aligned}
&\mathrm{e}^{-i\Omega_{\vec{p_-}}t}\partial_t\psi_{\vec{p_-}}(t) - \psi_{\vec{p_-}}(t)\,i\Omega_{\vec{p_-}}\mathrm{e}^{-i\Omega_{\vec{p_-}}t} = T\left(\vec{p_-},-\vec{q},\vec{p}\right)\psi_{\vec{p}}(t)\,\mathrm{e}^{-i\Omega_{\vec{p}}t}\overline{\psi_{\vec{q}}(t)}\mathrm{e}^{i\Omega_{\vec{q}}t}\\
&-\psi_{\vec{p_-}}(t)\,i\Omega_{\vec{p_-}}\mathrm{e}^{-i\Omega_{\vec{p_-}}t}, && (5.12)
\end{aligned}$$

which can then be simplified using

$$\begin{aligned}
\Delta_- &= \Omega_{\vec{p}} - \Omega_{\vec{q}} - \Omega_{\vec{p_-}},\\
\Delta_+ &= \Omega_{\vec{p}} + \Omega_{\vec{q}} - \Omega_{\vec{p_+}}.
\end{aligned} \tag{5.13}$$

The system is in resonance when $\Delta_{\pm} = 0$.

This gives a set of ordinary differential equations (ODEs):

$$\partial_t \psi_{\vec{p}}(t) = e^{it(\Delta_-)} T(\vec{p}, \vec{p_-}, \vec{q})\, \psi_{\vec{q}}(t)\, \psi_{\vec{p_-}}(t) + e^{it(\Delta_+)} T(\vec{p}, -\vec{q}, \vec{p_+})\, \psi_{\vec{p_+}}(t)\, \overline{\psi_{\vec{q}}(t)}, \tag{5.14}$$

$$\partial_t \psi_{\vec{q}}(t) = e^{-it(\Delta_-)} T(\vec{q}, -\vec{p_-}, \vec{p})\, \psi_{\vec{p}}(t)\, \overline{\psi_{\vec{p_-}}(t)} + e^{it(\Delta_+)} T(\vec{q}, -\vec{p}, \vec{p_+})\, \psi_{\vec{p_+}}(t)\, \overline{\psi_{\vec{p}}(t)}, \tag{5.15}$$

$$\partial_t \psi_{\vec{p_-}}(t) = e^{-it(\Delta_-)} T(\vec{p_-}, -\vec{q}, \vec{p})\, \psi_{\vec{p}}(t)\, \overline{\psi_{\vec{q}}(t)}, \tag{5.16}$$

$$\partial_t \psi_{\vec{p_+}}(t) = e^{-it(\Delta_+)} T(\vec{p_+}, \vec{q}, \vec{p})\, \psi_{\vec{p}}(t)\, \psi_{\vec{q}}(t)\,, \tag{5.17}$$

which can model the EHM system if it is initialized with four appropriate waves. An example of this is shown in figure 5.1 for a system initialised with a driving wave with modenumber $\vec{p} = (0, 10)$ and a zonal perturbing wave with $\vec{q} = (1, 0)$. The driving wave is alternately referred to as the pump wave. Satellite modes, alternately referred to as sidebands, are initialised with the same amplitude as the zonal mode. The growth and subsequent oscillation of the zonal mode can be seen.

The oscillations seen in this system in fact shows similarities to those in [Manfredi et al., 2001], where a spectral simulation was used to solve the EHM system. It should be noted that in [Manfredi et al., 2001] all modes except those involved in the four-wave interactions were suppressed, therefore the saturation of the zonal flow seen in our PDE simulations is not seen.

The effect of the extension to the CHM model is demonstrated in figure 5.2, which compares the amplitude of the perturbing mode, $\vec{q}$, from ODE simulations of the EHM and CHM cases. It is clear that the EHM system grows more rapidly. This is an expected effect from the modification of the coupling term, equation (5.4), where it can be seen that enabling the extension enhances coupling to modes with $k_y = 0$.

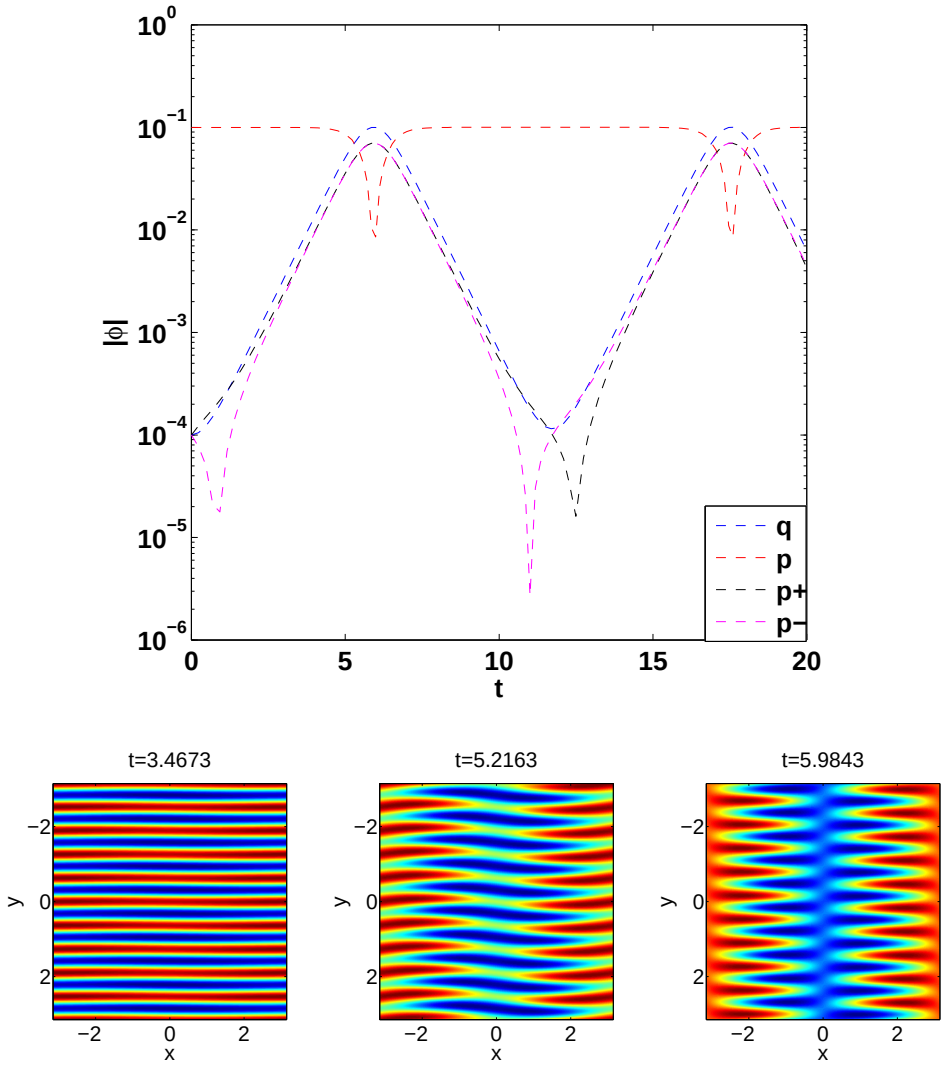

Figure 5.1: An example of the ODE system showing the satellite and zonal modes growing linearly at the same rate and then oscillating. Pictures of potential created by inverse Fourier transforming the amplitudes described by the ODEs are shown in the bottom panels. A change in the importance of modes with $k_x = 1$ can clearly be seen, although the satellite modes ensure that waves with $k_y = 10$ remain clearly visible.

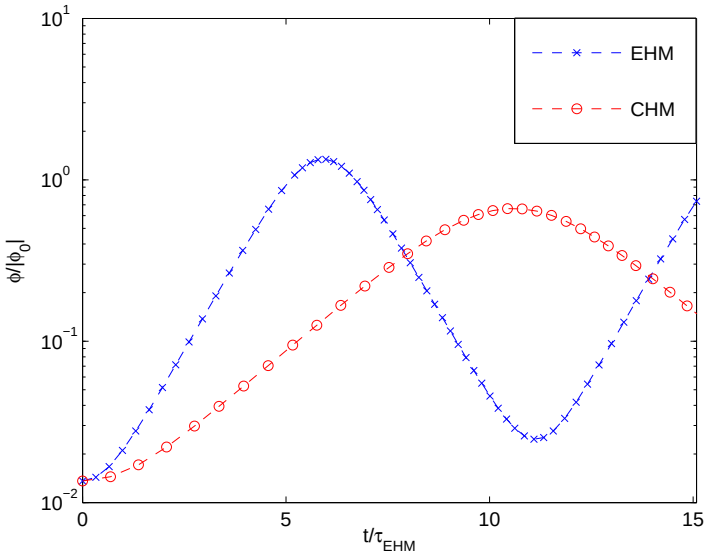

Figure 5.2: The growth of the zonal mode for identical initial conditions in ODE simulations of the EHM and CHM systems for the case $\vec{p} = (0, 10)$, $\rho_s = 0.6m$, $\psi_0 = 0.01\frac{m^2}{s}$ and $v_\star = 10\frac{m}{s}$. Both have been normalised using the analytical linear growth time of the EHM system. It can clearly be seen that the zonal mode grows faster for the EHM system.

5.3 A linear dispersion relation for the truncated system

5.3.1 Derivation

Linearised equations

The ODE equations (5.14) to (5.17) can be linearised by treating modes $\vec{q}, \vec{p_+}, \vec{p_-}$ as first order perturbations of the system with $\vec{p} \sim \mathcal{O}(0)$. We write this as

$$\vec{\psi} = \begin{pmatrix} \psi_{\vec{p}} \\ \psi_{\vec{q}} \\ \psi_{\vec{p_+}} \\ \psi_{\vec{p_-}} \end{pmatrix} = \begin{pmatrix} \psi_0 \\ 0 \\ 0 \\ 0 \end{pmatrix} + \epsilon \begin{pmatrix} 0 \\ \psi_{\vec{q}} \\ \psi_{\vec{p_+}} \\ \psi_{\vec{p_-}} \end{pmatrix} \tag{5.18}$$

where ϵ is a small parameter.

First equation (5.14) gives:

$$\partial_t \psi_0 = \varepsilon^2 e^{it(\Delta_-)} T\left(\vec{p}, \vec{p_-}, \vec{q}\right) \psi_{\vec{q}} \psi_{\vec{p_-}} + \varepsilon^2 e^{it(\Delta_+)} T\left(\vec{p}, -\vec{q}, \vec{p_+}\right) \psi_{\vec{p_+}} \overline{\psi_{\vec{q}}} \tag{5.19}$$

where keeping only terms $O(\varepsilon)$ and larger means

$$\partial_t \psi_0 = 0. \tag{5.20}$$

Then using equations (5.20) and(5.18) in each of equations (5.15),(5.16) and (5.17) in turn gives

$$\partial_t \psi_{\vec{q}} = e^{-it(\Delta_-)} T\left(\vec{q}, -\vec{p_-}, \vec{p}\right) \psi_0 \overline{\psi_{\vec{p_-}}} + e^{it(\Delta_+)} T\left(\vec{q}, -\vec{p}, \vec{p_+}\right) \psi_{\vec{p_+}} \overline{\psi_0}, \tag{5.21}$$

$$\partial_t \psi_{\vec{p_-}} = e^{-it(\Delta_-)} T\left(\vec{p_-}, -\vec{q}, \vec{p}\right) \psi_0 \overline{\psi_{\vec{q}}}, \tag{5.22}$$

$$\partial_t \psi_{\vec{p_+}} = e^{-it(\Delta_+)} T\left(\vec{p_+}, \vec{q}, \vec{p}\right) \psi_0 \psi_{\vec{q}}. \tag{5.23}$$

The Dispersion Relation

To obtain a dispersion relation for the MI we seek solutions to the linearised equations, (5.21) to (5.23), of the form

$$\begin{aligned} \psi_{\vec{q}}(t) &= A_{\vec{q}} e^{-i\omega_{\vec{q}} t}, \\ \psi_{\vec{p_+}}(t) &= A_{\vec{p_+}} e^{-i\omega_{\vec{p_+}} t}, \\ \psi_{\vec{p_-}}(t) &= A_{\vec{p_-}} e^{-i\omega_{\vec{p_-}} t}, \end{aligned} \tag{5.24}$$

which gives us

$$\begin{aligned}
\partial_t A_{\vec{q}} e^{-i\omega_{\vec{q}} t} &= e^{-it(\Delta_-)} T\left(\vec{q}, -\vec{p_-}, \vec{p}\right) \psi_0 \overline{A_{\vec{p_-}} e^{-i\omega_{\vec{p_-}} t}} \\
&\quad + e^{it(\Delta_+)} T\left(\vec{q}, -\vec{p}, \vec{p_+}\right) \overline{\psi_0} A_{\vec{p_+}} e^{-i\omega_{\vec{p_+}} t} \\
&\Rightarrow \\
-i\omega_{\vec{q}} A_{\vec{q}} &= T\left(\vec{q}, -\vec{p_-}, \vec{p}\right) \psi_0 \overline{A_{\vec{p_-}}} e^{i(\omega_{\vec{p_-}} + \omega_{\vec{q}} - \Delta_-)t} \\
&\quad + T\left(\vec{q}, -\vec{p}, \vec{p_+}\right) \overline{\psi_0} A_{\vec{p_+}} e^{-i(\omega_{\vec{p_+}} - \omega_{\vec{q}} - \Delta_+)t}, \qquad (5.25)
\end{aligned}$$

$$\begin{aligned}
\partial_t A_{\vec{p_-}} e^{-i\omega_{\vec{p_-}} t} &= e^{-it(\Delta_-)} T\left(\vec{p_-}, -\vec{q}, \vec{p}\right) \psi_0 \overline{A_{\vec{q}} e^{-i\omega_{\vec{q}} t}} \\
&\Rightarrow \\
-i\omega_{\vec{p_-}} A_{\vec{p_-}} &= T\left(\vec{p_-}, -\vec{q}, \vec{p}\right) \psi_0 \overline{A_{\vec{q}}} e^{i(\omega_{\vec{q}} + \omega_{\vec{p_-}} - \Delta_-)t}, \qquad (5.26)
\end{aligned}$$

$$\begin{aligned}
\partial_t A_{\vec{p_+}} e^{-i\omega_{\vec{p_+}} t} &= e^{-it(\Delta_+)} T\left(\vec{p_+}, \vec{q}, \vec{p}\right) \psi_0 A_{\vec{q}} e^{-i\omega_{\vec{q}} t} \\
&\Rightarrow \\
-i\omega_{\vec{p_+}} A_{\vec{p_+}} &= T\left(\vec{p_+}, \vec{q}, \vec{p}\right) \psi_0 A_{\vec{q}} e^{-i(\omega_{\vec{q}} + \Delta_+ - \omega_{\vec{p_+}})t}. \qquad (5.27)
\end{aligned}$$

We now remove the time dependence of these equations by requiring

$$\omega_{\vec{p_-}} + \omega_{\vec{q}} = \Delta_- \qquad (5.28)$$

and

$$-\omega_{\vec{q}} + \omega_{\vec{p_+}} = \Delta_+ \qquad (5.29)$$

so that equations (5.25) to (5.27) can be simplified to give

$$\begin{aligned}
-i\omega_{\vec{q}} A_{\vec{q}} &= T\left(\vec{q}, -\vec{p_-}, \vec{p}\right) \psi_0 \overline{A_{\vec{p_-}}} + T\left(\vec{q}, -\vec{p}, \vec{p_+}\right) \overline{\psi_0} A_{\vec{p_+}}, \\
-i\omega_{\vec{p_-}} A_{\vec{p_-}} &= T\left(\vec{p_-}, -\vec{q}, \vec{p}\right) \psi_0 \overline{A_{\vec{q}}}, \\
-i\omega_{\vec{p_+}} A_{\vec{p_+}} &= T\left(\vec{p_+}, \vec{q}, \vec{p}\right) \psi_0 A_{\vec{q}}.
\end{aligned}$$

This can be written as

$$A \begin{pmatrix} A_{\vec{q}} \\ A_{\vec{p_+}} \\ \overline{A_{\vec{p_-}}} \end{pmatrix} = 0 \qquad (5.30)$$

where

$$A = \begin{pmatrix} -i\omega_{\vec{q}} & -T\left(\vec{q}, -\vec{p}, \vec{p_+}\right)\overline{\psi_0} & -T\left(\vec{q}, -\vec{p_-}, \vec{p}\right)\psi_0 \\ -T\left(\vec{p_-}, -\vec{q}, \vec{p}\right)\overline{\psi_0} & 0 & i\omega_{\vec{p_-}} \\ -T\left(\vec{p_+}, \vec{q}, \vec{p}\right)\psi_0 & -i\omega_{\vec{p_+}} & 0 \end{pmatrix}. \tag{5.31}$$

Equation (5.30) has a non trivial solution when

$$\det(A) = 0, \tag{5.32}$$

hence

$$\begin{aligned} \det(A) =& i\omega_{\vec{q}}\omega_{\vec{p_-}}\omega_{\vec{p_+}} + i\omega_{\vec{p_-}}|\psi_0|^2 T\left(\vec{q}, -\vec{p}, \vec{p_+}\right) T\left(\vec{p_+}, \vec{q}, \vec{p}\right) \\ & - i\omega_{\vec{p_+}}|\psi_0|^2 T\left(\vec{q}, -\vec{p_-}, \vec{p}\right) T\left(\vec{p_-}, -\vec{q}, \vec{p}\right) = 0. \end{aligned} \tag{5.33}$$

Using equations (5.28), (5.29) and (5.13), we can rewrite equation (5.33) as

$$\begin{aligned} & \omega_{\vec{q}}(\Omega_{\vec{p}} - \Omega_{\vec{q}} - \Omega_{\vec{p_-}} - \omega_{\vec{q}})(\Omega_{\vec{p}} + \Omega_{\vec{q}} - \Omega_{\vec{p_+}} + \omega_{\vec{q}}) \\ & + (\Omega_{\vec{p}} - \Omega_{\vec{q}} - \Omega_{\vec{p_-}} - \omega_{\vec{q}})|\psi_0|^2 T\left(\vec{q}, -\vec{p}, \vec{p_+}\right) T\left(\vec{p_+}, \vec{q}, \vec{p}\right) \\ & - (\Omega_{\vec{p}} + \Omega_{\vec{q}} - \Omega_{\vec{p_+}} + \omega_{\vec{q}})|\psi_0|^2 T\left(\vec{q}, -\vec{p_-}, \vec{p}\right) T\left(\vec{p_-}, -\vec{q}, \vec{p}\right) = 0, \end{aligned} \tag{5.34}$$

which can be rearranged to give a dispersion relation for the 4MT system,

$$(\Omega - \Omega_{\vec{q}}) + \frac{|\psi_0|^2 T\left(\vec{q}, -\vec{p}, \vec{p_+}\right) T\left(\vec{p_+}, \vec{q}, \vec{p}\right)}{(\Omega + \Omega_{\vec{p}} - \Omega_{\vec{p_+}})} - \frac{|\psi_0|^2 T\left(\vec{q}, -\vec{p_-}, \vec{p}\right) T\left(\vec{p_-}, -\vec{q}, \vec{p}\right)}{(-\Omega + \Omega_{\vec{p}} - \Omega_{\vec{p_-}})} = 0, \tag{5.35}$$

where $\Omega = \Omega_{\vec{q}} + \omega_{\vec{q}}$.

5.3.2 The linear growth rate

Analytical predictions of growth rates

Solving equation (5.35), whilst holding all parameters other than $\vec{q}$ and ρ_s constant, allows maps of predicted growth rates to be produced. This is shown if figure 5.3 for increasing ρ_s. It can be seen that as ρ_s is increased the number of growing modes increases and they begin to extend off the resonant curve seen in figure 5.3(a). This is due to the ρ_s terms in the coupling parameter, equation (5.4). As $\rho_s \to \infty$ the coupling between modes will be enhanced and the additional terms from the extension to the CHM equation will become negligible. This leads to larger numerators in equation (5.35) and an increased growth rate. This trend has

been observed previously in simulations of the CHM equation [Connaughton et al., 2010] where increasing ψ_0 also leads to larger numerators in equation (5.35). We treat ρ_s and $v_\star$ as independent parameters here, though it should be noted that equation (3.33) indicates that this in reality requires an adjustment to the density gradient to keep $v_\star$ constant.

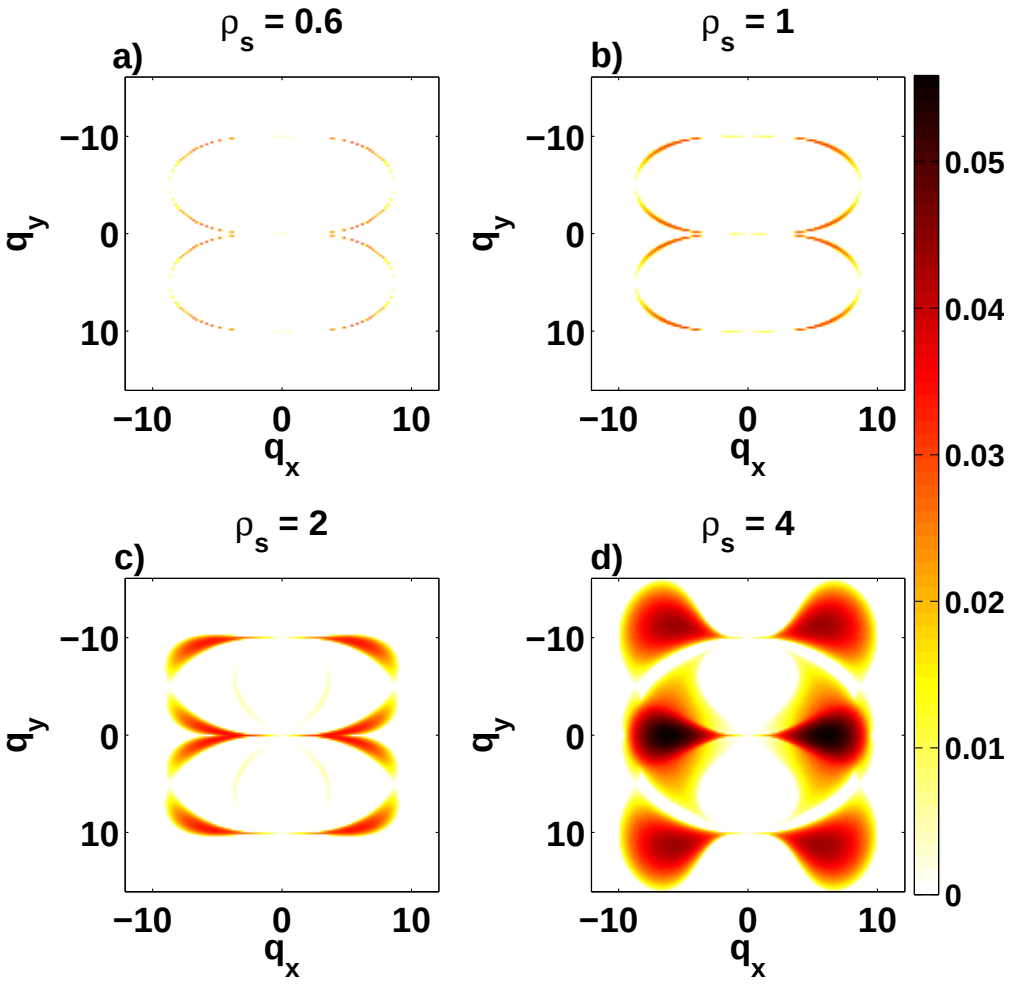

Figure 5.3: The analytical linear growth rate maps for various ρ_s with $\vec{p} = (0, 10)$, $v_\star = 10\frac{m}{s}$ and $\psi_0 = 0.001\frac{m^2}{s}$. It can be seen that as ρ_s is increased growth is predicted for modes further away from the resonant curve.

These maps allow for an informed selection of modes when running full MI simulations. However, as the derivation presented in section 5.3.1 makes assumptions about the resonances of the modes in the system, equations (5.28) and (5.29),

that may not necessarily be satisfied at all in the full simulation, or may be better satisfied by a different set of modes, it is not always accurate. An example is presented in figure 5.4. The system was initialised with $\vec{p} = (0, 10)$ and $\vec{q} = (1, 10)$. Solving equation (5.35) produces an incorrect linear growth rate prediction, shown in figure 5.4 as the line labelled 'linear $q = (1, 10)$'. In this case the PDE system rapidly grows an extra mode $\vec{k} = (-1, 10)$, by $t \sim 10\tau$ its amplitude is comparable to that of the zonal mode. This completes the set of four modes that would be formed by a system initialised with $\vec{p} = (0, 10)$ and $\vec{q} = (1, 0)$. In this new system $\Delta_{\pm}$ is closer to 0 and resonance conditions (5.28) and (5.28) ensure that $\vec{q}$,$\vec{p_+}$ and $\vec{p_-}$ all grow at the rate given by assuming $\vec{q} = (1, 0)$ which is shown in figure 5.4 as the line labelled 'linear $q = (1, 0)$'. It can be seen that the zonal mode grows at this new growth rate. [Connaughton et al., 2010] showed how the 4MT was a better model for zonal flow transition than a 3 mode truncation as a full simulation would rapidly grow the additional fourth mode. This result was reported earlier in [Manfredi et al., 2001] where the link between the drift-wave to zonal-flow transition in [Smolyakov et al., 2000a,b] and the three wave interactions in Terry and Horton [1982]; Waltz [1983]; Biskamp and Kaifen [1985] was discussed. Combined with the situation presented here, this demonstrates the limitations of these truncated models. Full systems can grow additional modes, and in certain circumstances they can interact more strongly than the modes prescribed in the initial conditions. In this case the 4MT model will produce incorrect predictions.

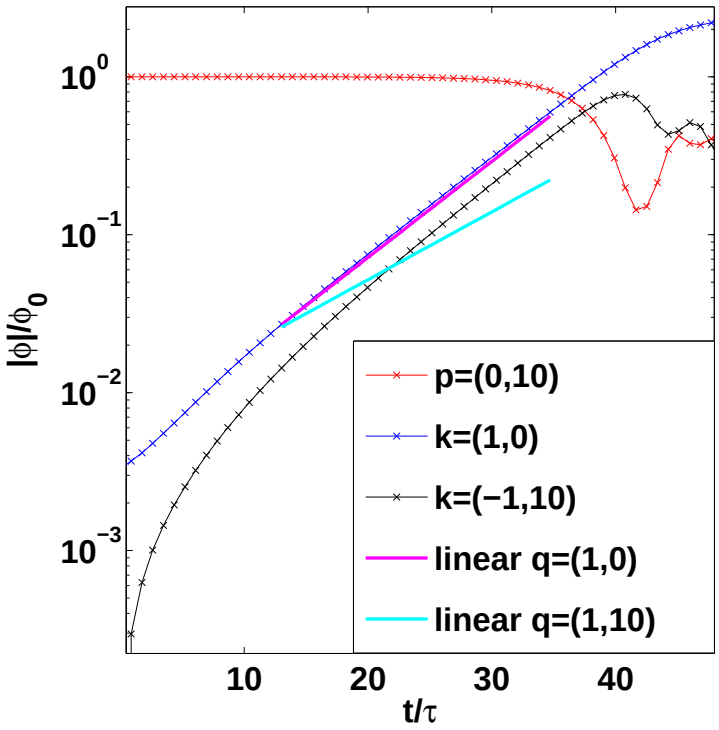

Figure 5.4: The growth of an additional mode ($\vec{k} = (-1, 10)$) as mesured from a full PDE simulation in a system seeded with $\vec{p} = (0, 10)$ and $\vec{q} = (1, 10)$. This completes the set of modes that would be seeded in a system with $\vec{q} = (1, 0)$. The linear growth predicted for these two systems is indicated with straight lines.

The effect of the EHM equation

It can be seen from the coupling parameter, equation (3.48), that the extension to the CHM equation enhances coupling to modes with $k_y = 0$. This can be demonstrated by plotting a map of the predicted growth rate for an equivalent set of parameters for both the extended and non-extended cases. This is done by solving equation (5.35) for every q_x and q_y pair whilst keeping all other parameters constant. As equation (5.35) is cubic only the largest negative imaginary solution is plotted. For the set of parameters chosen to produce figure 5.5 the mode $\vec{q} = (1, 0)$ has a 0, and therefore oscillatory, solution for the CHM but not the EHM case. In situations where both the EHM and CHM are expected to grow the growth rate of modes with $k_y = 0$ is larger for the EHM system.

a)

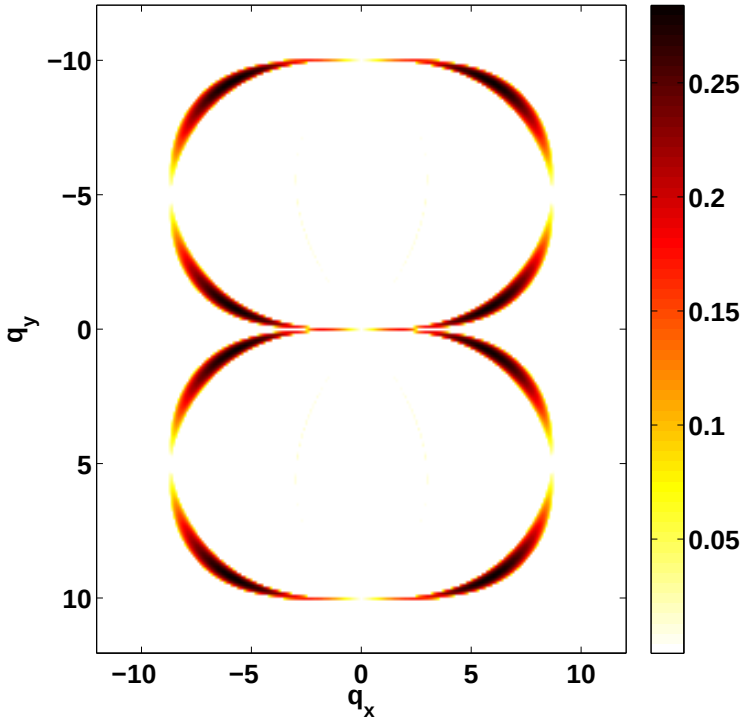

b)

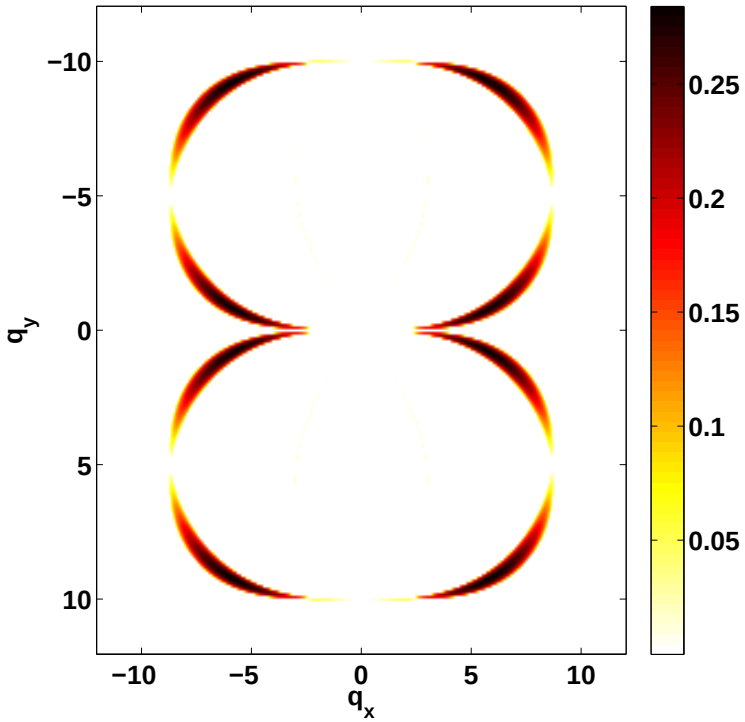

Figure 5.5: Maps of the analytical linear growth rate for the case $\vec{p} = (0, 10)$, $\rho_s = 0.4m$, $\psi_0 = 0.01\frac{m^2}{s}$ and $v_\star = 10\frac{m}{s}$. Unlike the EHM (a) the CHM (b) has no predicted growth for values near $\vec{q} = (0, 0)$.

The linear growth time

To allow for comparisons between different simulations we define a linear growth time

$$\tau = \frac{1}{\gamma}$$

where γ is the growth rate calculated by solving equation (5.35) . As the system is in SI units for this chapter this is measured in seconds

5.4 Results

5.4.1 The two dynamical regimes accessible by varying ρ_s

We begin this section by demonstrating the development of zonal flows from the initial conditions described earlier in this chapter, namely a driving mode $\vec{p} = (0, p_y)$, a zonal perturbing mode $\vec{q} = (q_x, 0)$ and two satellite modes $\vec{p_\pm} = \vec{p} \pm \vec{q}$ where $p \gg q$.

Firstly figure 5.6 shows a case where the system transitions to a strong persistent zonal flow. The overlaid velocity profiles in this figure show that even once the bands of potential have begun to break apart a zonal flow is still present.

Next a case where a zonal flow forms, but then transitions back to a drift wave, is shown in figure 5.7. In this case a Kármán like vortex street is formed, before stretching to form a more drift wave like structure, and finally compressing again to form another broader set of vortex streets. It should be noted that the limits on the velocity axis are not fixed and that the initial set of streets had the strongest zonal flow.

These two regimes have previously been identified for the 4MT system and related to a dimensionless parameter, M_ρ, that measures the strength of the nonlinearity of the system[Connaughton et al., 2010]. Following [Connaughton et al., 2010] and [Gill, 1974] we define

$$M_\rho = \frac{\rho_s^2 \psi_0 p^3}{v_*} \tag{5.36}$$

such that larger values of M_ρ indicate a more nonlinear system. The $v_\star$ term in equation (5.36) is proportional to the β term in [Manfredi, 1999] where it was found that increasing β, hence lowering M_ρ lead to the inhibition of turbulent energy transfer.

This relation can most easily be demonstrated by rewriting equation (5.35) in terms of dimensionless parameters. To do this we note that $T(k, k_1, k_2)$ has units length^{-2} and that Ω and $\Omega_{\vec{k}}$ have units time^{-1}. We therefore write $T(k, k_1, k_2) =$

$p^2T'(k,k_1,k_2)$, $\Omega = \frac{v_\star}{p\rho_s^2}\Omega'$ and $\Omega_{\vec{k}} = \frac{v_\star}{p\rho_s^2}\Omega'_{\vec{k}}$ where quantities with a prime are unitless. Substituting these into equation (5.35) gives

$$\frac{v_\star}{p\rho_s^2}(\Omega' - \Omega'_{\vec{q}}) + \frac{|\psi_0|^2 p^2 T'\left(\vec{q},-\vec{p},\vec{p_+}\right) p^2 T'\left(\vec{p_+},\vec{q},\vec{p}\right)}{\frac{v_\star}{p\rho_s^2}(\Omega' + \Omega'_{\vec{p}} - \Omega'_{\vec{p_+}})} - \frac{|\psi_0|^2 p^2 T'\left(\vec{q},-\vec{p_-},\vec{p}\right) p^2 T'\left(\vec{p_-},-\vec{q},\vec{p}\right)}{\frac{v_\star}{p\rho_s^2}(-\Omega' + \Omega'_{\vec{p}} - \Omega'_{\vec{p_-}})} = 0 \tag{5.37}$$

which can be rearranged to give

$$(\Omega' - \Omega'_{\vec{q}}) + M_\rho^2 \left(\frac{T'\left(\vec{q},-\vec{p},\vec{p_+}\right) T'\left(\vec{p_+},\vec{q},\vec{p}\right)}{(\Omega' + \Omega'_{\vec{p}} - \Omega'_{\vec{p_+}})} - \frac{T'\left(\vec{q},-\vec{p_-},\vec{p}\right) T'\left(\vec{p_-},-\vec{q},\vec{p}\right)}{(-\Omega' + \Omega'_{\vec{p}} - \Omega'_{\vec{p_-}})} \right) = 0. \tag{5.38}$$

This clearly shows that the dimensionless parameter M_ρ directly controls the strength of the nonlinear coupling terms relative to the other parameters in the system. The first situation demonstrated above, in figure 5.6, when the system saturates with the bulk of its energy being transferred to the zonal mode occurs for large values of M_ρ and is described in this work as a 'strongly nonlinear' case. The second, figure 5.7, is a 'weakly nonlinear' case, where the system oscillates with energy being passed between the pump and zonal modes. These oscillations are similar to those seen in predator prey models of drift-wave and zonal-flow interaction[Diamond et al., 1994; Chen et al., 2000; Berionni and Gürcan, 2011].

In the past [Connaughton et al., 2010] demonstrated these two regimes by adjusting ψ_0, however the same selection can be achieved by adjusting ρ_s. This is shown in figure 5.8 where the amplitude of the zonal mode for several different values of ρ_s is plotted. It should be noted that we have chosen this expression for M_ρ so that it contains all the parameters in equation (3.32). The $v_\star$ term could be written as $v_\star = \rho_s^2\beta$ in which case M_ρ would reduce to M as given in [Connaughton et al., 2010].

The weakly nonlinear case was investigated first and is shown in figure 5.8(a). The systems all have a linear phase in which the zonal mode grows at the rate predicted by equation (5.35), yet increasing ρ_s gradually changes the behaviour so that the zonal mode saturates rather than oscillates. The change between regimes occurs between $\rho_s = 1.5m$ and $\rho_s = 2m$, which corresponds to a value of M_ρ between 0.23 and 0.31. We recognise that this range of parameters does not directly apply to tokamaks. A range of spatial scales from $10^{-2} < k\rho_s < 10^0$ is suggested by[Scott, 2006], evidently the cases presented here fall outside this range.

The second case investigated had the initial pump wave amplitude ten times

larger, $\psi_0 = 0.01\frac{m^2}{s}$, leading to strong nonlinear dynamics. In this case the opposite procedure was applied and decreasing ρ_s led to a switch from saturating to oscillating behaviour, as shown in figure 5.8(b). The change in behaviour now corresponds to a value of M_ρ between 0.16 and 0.25. Despite the two sets of simulations beginning with very different drift wave amplitudes, the switch between regimes occurs at roughly the same value of M_ρ. This is as expected. As M_ρ is dimensionless and includes all the parameters of the system it controls the state of the system, rather than the individual parameters in equation (3.33).

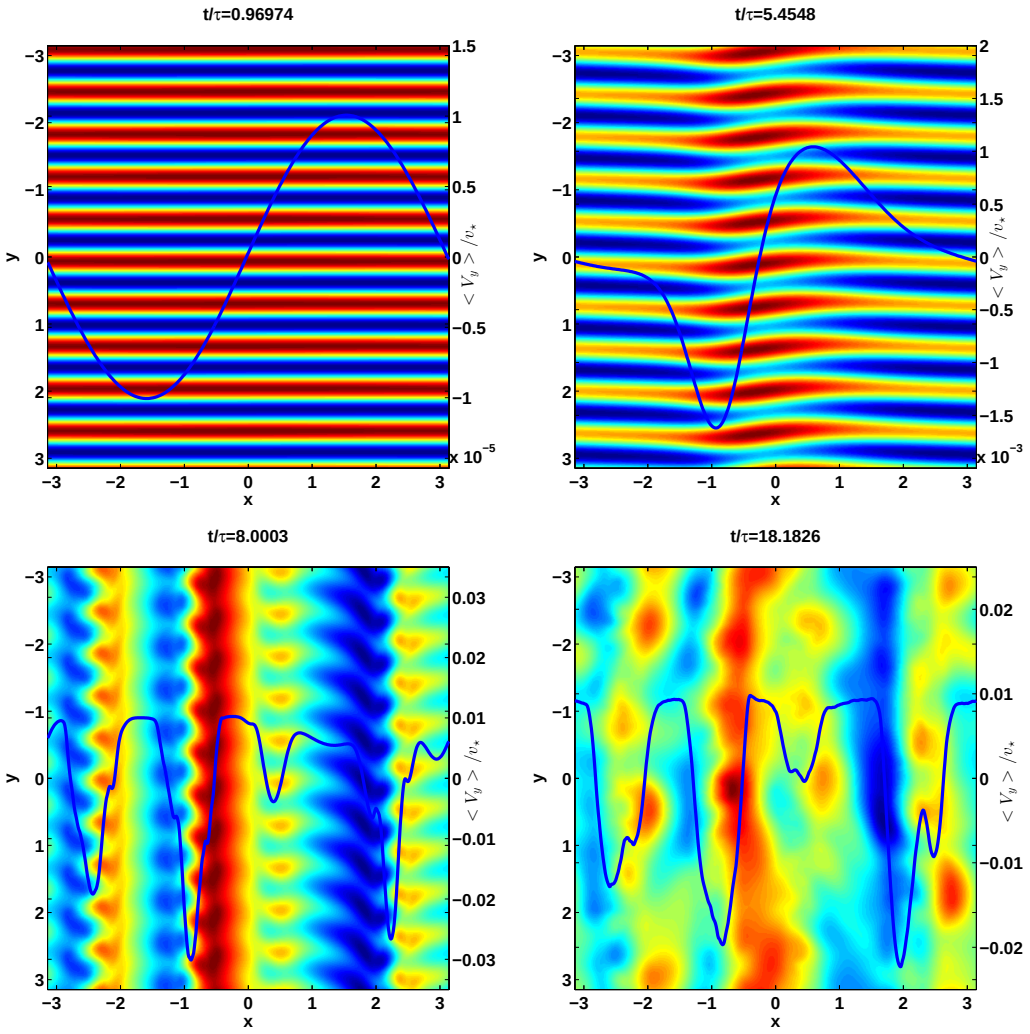

Figure 5.6: The potential at various times in a simulation initialised with $\vec{p} = (0, 10)$, $\vec{q} = (1, 0)$, $\rho_s = 1.0m$, $v_\star = 10\frac{m}{s}$ and $\phi_0 = 0.01\frac{m^2}{s}$. It is strongly nonlinear with $M_\rho = 1$, therefore a transition to a zonal flow that saturates can be seen. The average velocity in the y (vertical) direction is shown overlaid.

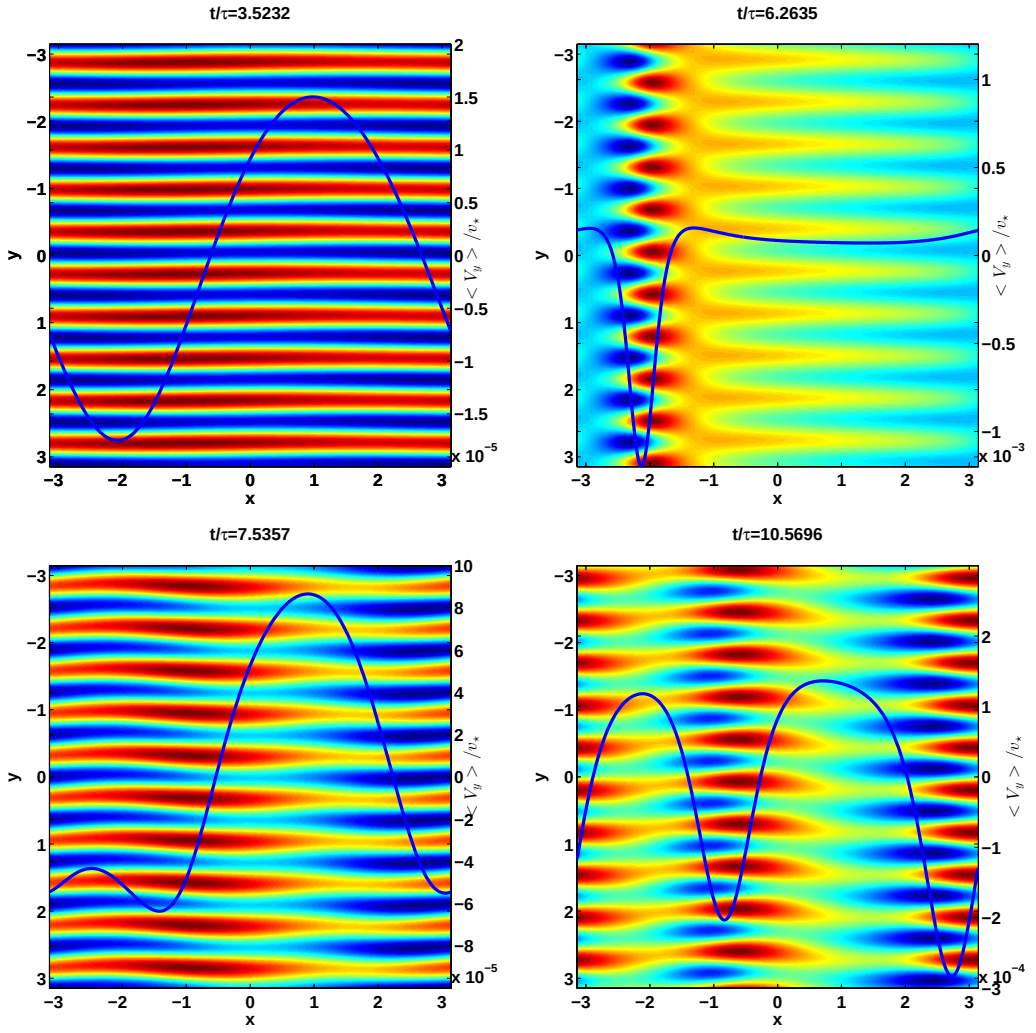

Figure 5.7: The potential at various times in a simulation initialised with $\vec{p} = (0, 10)$, $\vec{q} = (1, 0)$, $\rho_s = 1.25m$, $v_\star = 10\frac{m}{s}$ and $\phi_0 = 0.001\frac{m^2}{s}$. It is weakly nonlinear with $M_\rho \approx 0.16$. A transition to a zonal flow that stretches back to a drift wave dominated system can be seen. The average velocity in the y (vertical) direction is shown overlaid.

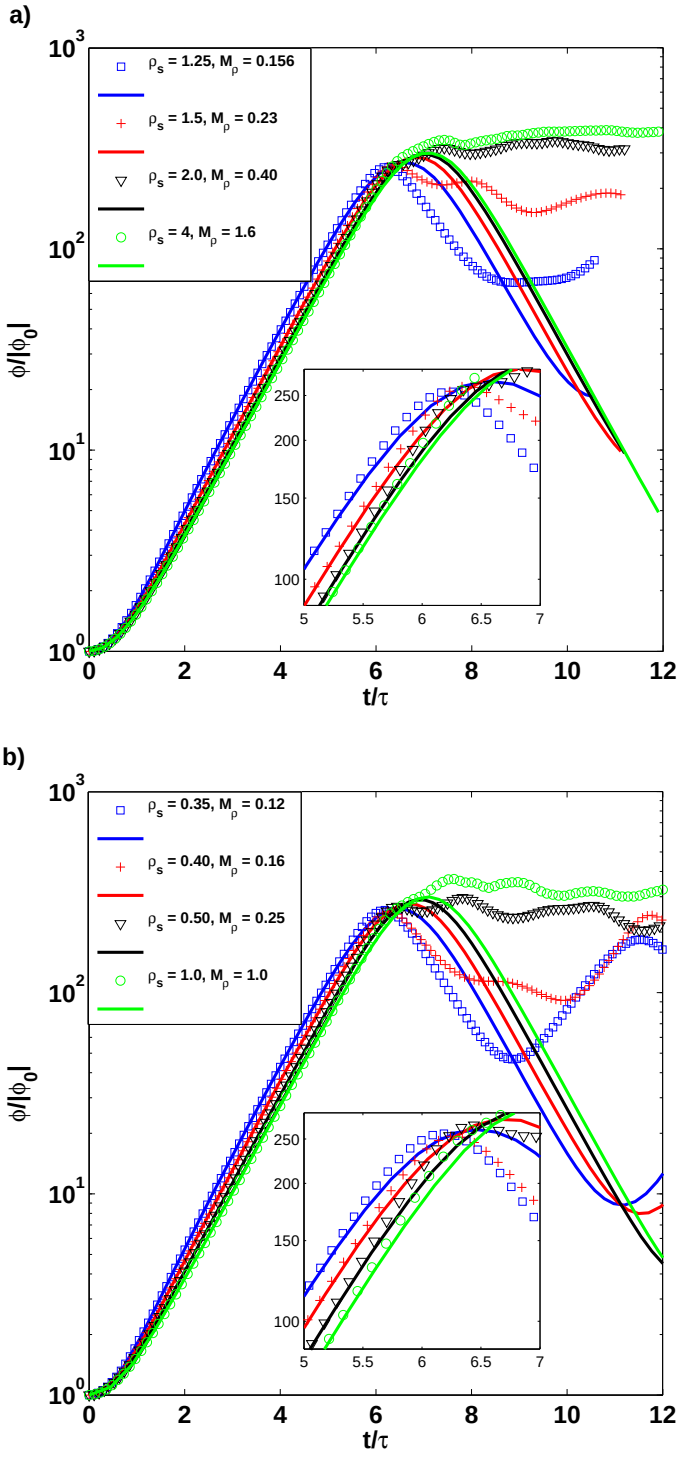

Figure 5.8: The amplitude of the zonal mode for various ρ_s (in metres) with (a) $\psi_0 = 0.001\frac{m^2}{s}$ and (b) $\psi_0 = 0.01\frac{m^2}{s}$, other parameters were identical, $v_\star = 10\frac{m}{s}$, $p = (0, 10)$, $q = (1, 0)$. Each case has been scaled by its own linear growth time. ODE predictions are shown with solid lines, full simulations with markers.

5.4.2 Oscillations in off-axis modes

The oblique case, where the perturbation $\vec{q}$ is not perpendicular to the pump wave vector, $\vec{p}$, is fundamentally different from purely zonal one. Off-axis modes often show rapid oscillations, rather than linear amplitude growth, from the beginning of their evolution. Figure 5.9 demonstrates this for the case of perturbing wave vector $\vec{q} = (2, 2)$, a moderate value of Larmor radius $\rho_s = 1m$ and a nonlinearity parameter $M_\rho = 1$. In this case a rapid oscillation of the perturbing mode is clearly seen. The frequency of these oscillations is correctly captured by the ODE solution, equations (5.14) to (5.17).

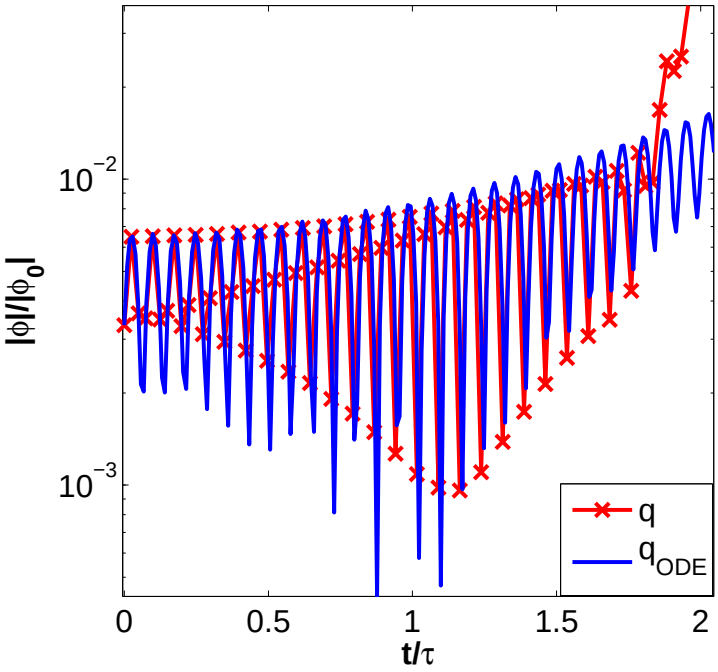

Figure 5.9: The amplitudes of the perturbing mode, $\vec{q}$, in an off axis simulation. The line with markers shows the full numerical simulation, the other is the prediction made by the ODE equations, (5.14) to (5.17). The initial conditions were $\psi_0 = 0.01\frac{m^2}{s}$, $\vec{p} = (0, 10)$ $\vec{q} = (2, 2)$, $\rho_s = 1m$, $v_\star = 10\frac{m}{s}$, and $M_\rho = 1$.

A similar situation can be seen in figure 5.10 where the perturbing mode was $\vec{q} = (3, 2)$. At first the system is initially dominated by oscillations, however, at around 2 linear growth times the system begins growing at roughly the linear

growth rate. It continues to oscillate, although the oscillations become increasingly less important as the PDE simulation begins to diverge from the ODE predictions. Real space images of potential for this system are shown in figure 5.11. The roll up of the system to Kármán like vortex streets, at an angle to the density gradient, can be seen.

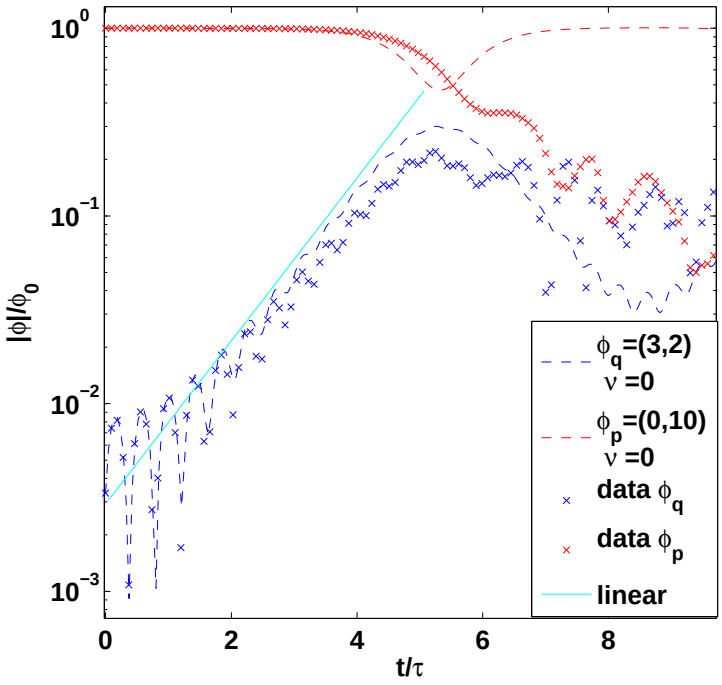

Figure 5.10: The amplitudes of the perturbing mode, $\vec{q} = (3, 2)$, and the driving mode $\vec{p}$ in an off axis simulation. The markers show the full numerical simulation and the dashed lines the predictions made by the ODE equations. A line demonstrating the linear growth rate is shown. The initial conditions were $\psi_0 = 0.01\frac{m^2}{s}$, $\rho_s = 1m$, $v_\star = 10\frac{m}{s}$, and $M_\rho = 1$. A combination of oscillations and linear growth can be seen.

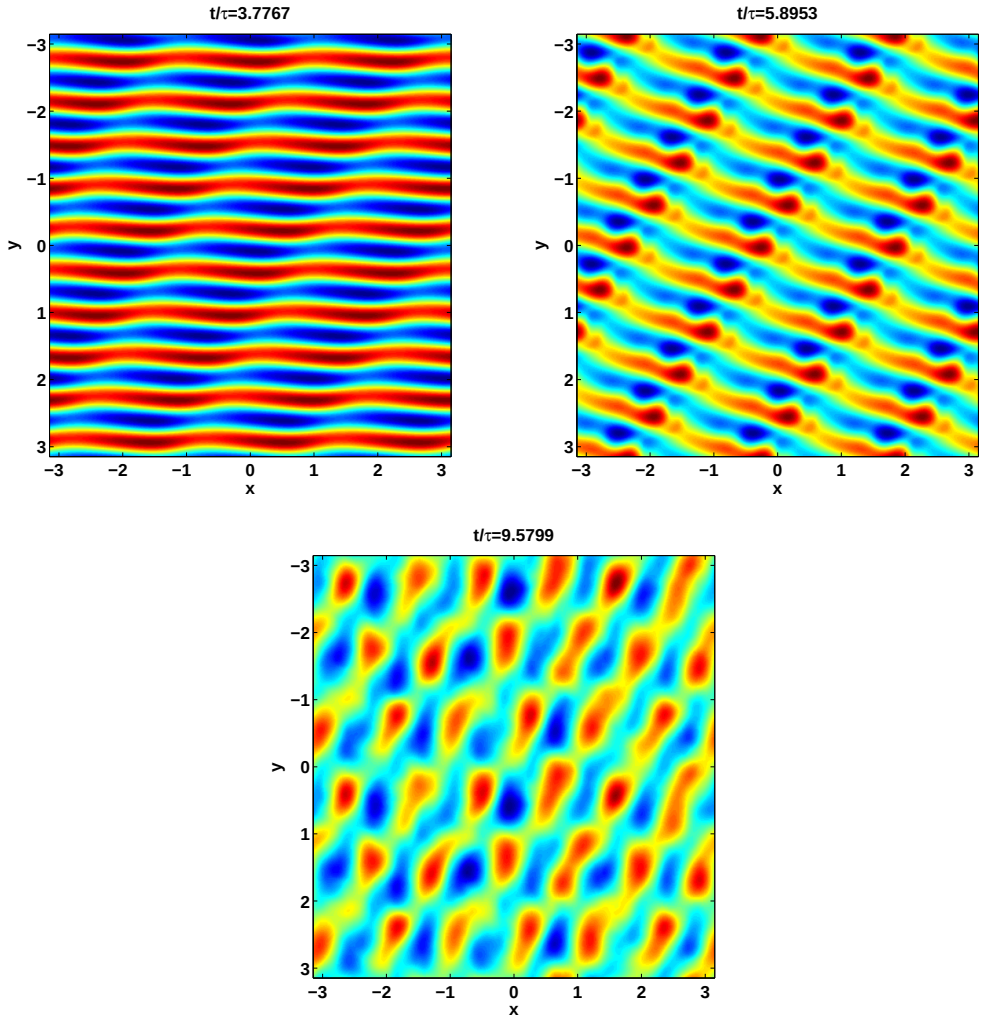

Figure 5.11: Real space images of potential for the system in figure 5.10. The formation of vortex streets at an angle to the axes can be seen.

This rapid oscillation was not present for all of cases studied. Figure 5.12 shows a case where the system was seeded with $\vec{p} = (0, 10)$ and $\vec{q} = (6, 1)$, in this case the initial rapid oscillation is not present and the system grows at roughly the linear growth rate. A sight deviation from linear growth is correctly captured by the ODE model. The analytical predictions suggest that this should be one of the fastest growing modes in the system, so dominant linear growth is not unexpected. Real space images of this system are shown in figure 5.13. It can be seen that the potential forms vortices, but that as the perturbing mode saturates these merge to form an off axis drift wave with a strong zonal component.

In these off-axis systems additional modes can be rapidly grown which can interact more strongly than the initial seed modes. This is explored further in section 5.4.3.

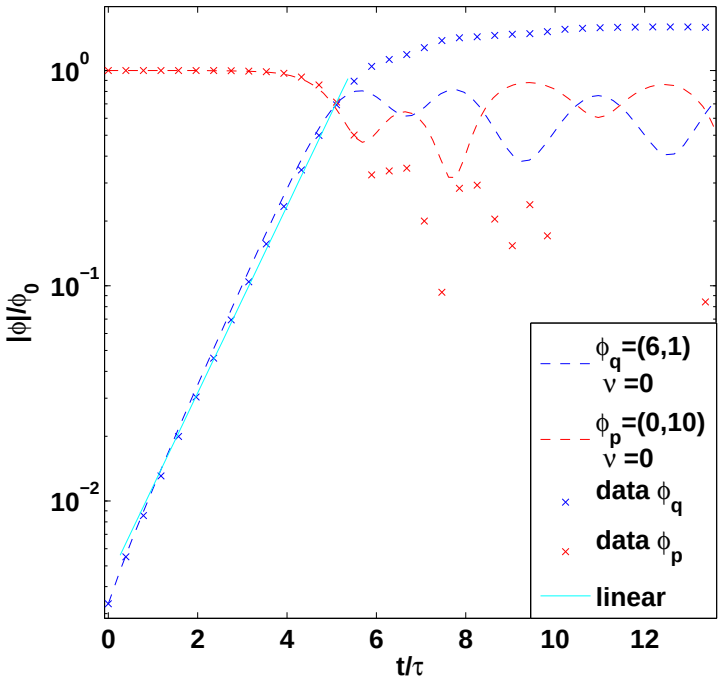

Figure 5.12: The amplitudes of the perturbing mode, $\vec{q} = (6, 1)$, and the driving mode $\vec{p}$ in an off axis simulation. The markers show the full numerical simulation and the dashed lines the predictions made by the ODE equations. A line demonstrating the growth rate is shown. The initial conditions were $\psi_0 = 0.01\frac{m^2}{s}$, $\rho_s = 1m$, $v_\star = 10\frac{m}{s}$, and $M_\rho = 1$. The system grows at approximately the linear growth rate before saturating.

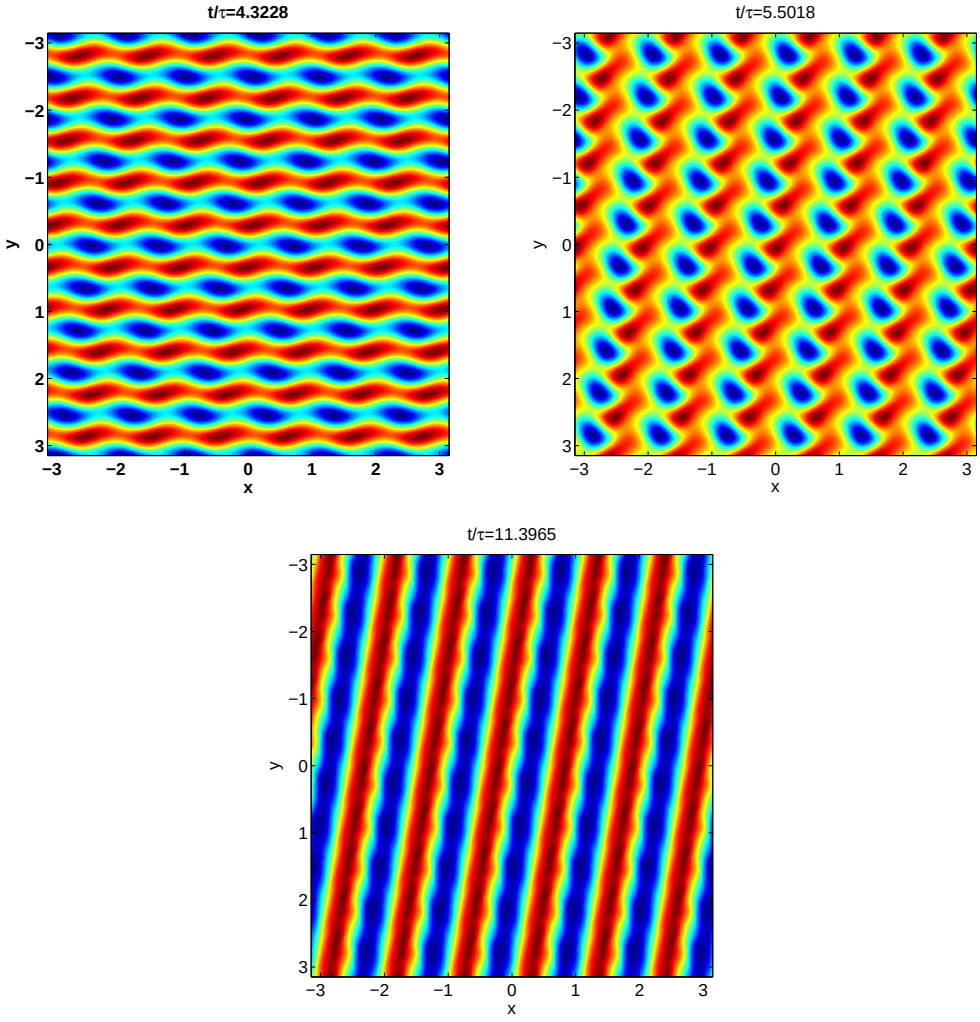

Figure 5.13: Real space images of potential for the system in figure 5.12. The formation of vortex streets at an angle to the axes can be seen before they merge to form an off axis drift wave.

5.4.3 The effect of additional modes in off axis simulations

We now examine numerical simulations of the CHM and the EHM equations for an off axis, $\vec{q} = (2, 2)$, small Larmor radius case. Real space images of potential for the EHM case are shown in figure 5.14, where a change the in angle of the vortex streets formed can be seen . Figure 5.15 shows the evolution of several selected modes for this case, which has $\rho_s = 0.6m$, and $M_\rho = 0.36$. These were obtained from a DNS of the CHM and the EHM equations, shown in figures 5.15 (a) and (b) respectively.

It is clear that the behaviour is very different. While both cases grow modes not included in the initial conditions, the EHM case grows a number of modes with $k_y = 0$ more rapidly than in the CHM case. Once the system is saturated these zonal modes have a larger amplitude than in the CHM case. Of particular note is $\vec{q} = (3, 0)$, this is the fastest growing mode in the EHM case and even becomes the dominant mode in the system for a period of time. Eventually both system are dominated by the same mode, $\vec{q} = (6, 1)$, which is the analytically predicted fastest growing mode for the CHM case. The change in the angle of the vortex streets seen in figure 5.14 occurs when the dominant mode in the system switches from $\vec{q} = (3, 0)$ to $\vec{q} = (6, 1)$. In [McCarthy et al., 2004] an additional instability was described, where waves growing due to the modulational instability were able to interact nonlinearly and produce a long wavelength zonal flow. In figure 5.15 the mode $\vec{q} = (1, 0)$ shows behaviour similar to that described in [McCarthy et al., 2004] where the long wavelength mode initially grows slowly before transitioning to a rapid growth state.

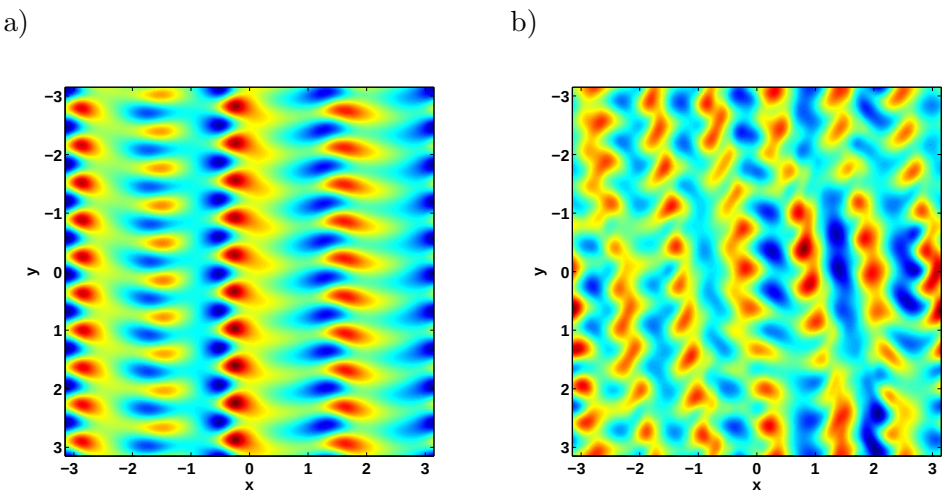

Figure 5.14: Real space images of potential for an EHM simulation with $\psi_0 = 0.01\frac{m^2}{s}$, $\vec{p} = (0, 10)$ $\vec{q} = (2, 2)$, $\rho_s = 0.6m$, $v_\star = 10\frac{m}{s}$, and $M = 0.36$. The growth of selected modes from this system is shown in figure 5.15(b). The images of potential are taken at times a), $t/\tau = 2.26$, and b), t/τ=2.58. A change in angle of the vortex streets can be seen.

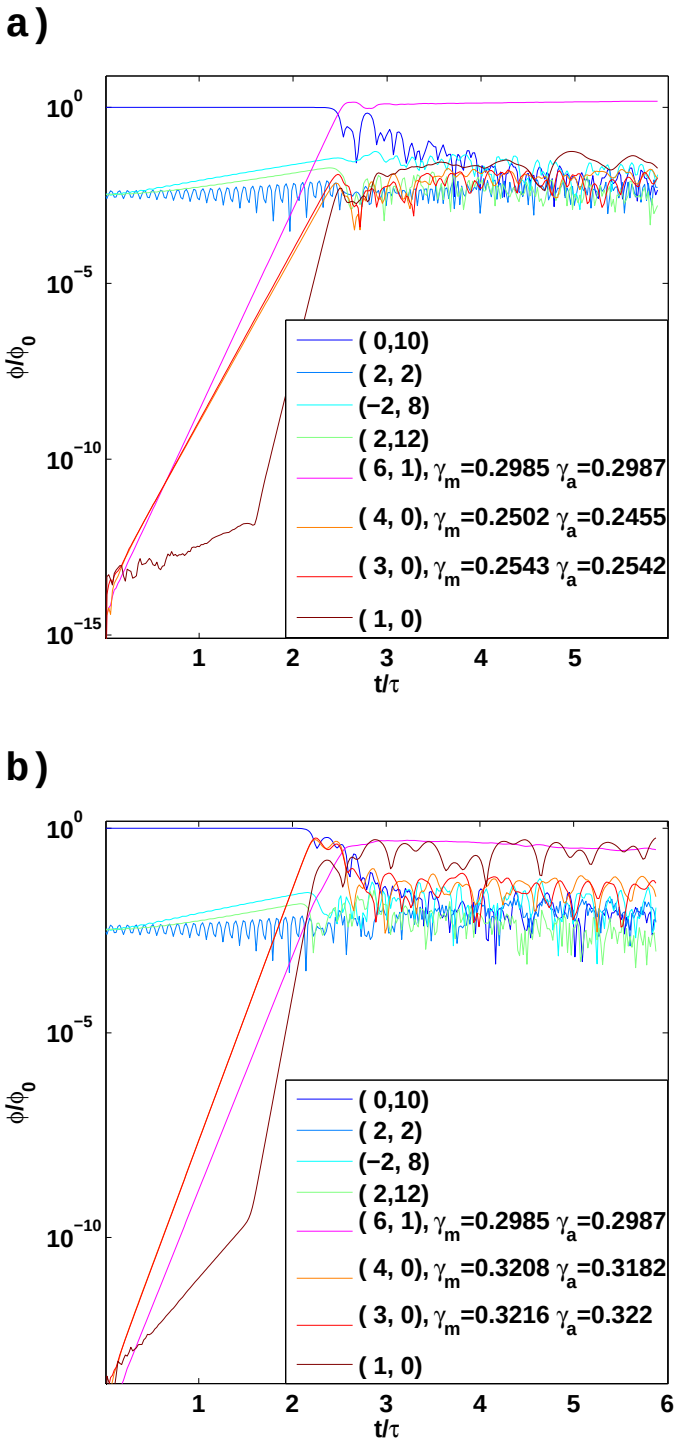

Figure 5.15: A comparison of the growth of various modes for the off axis system shown in figure 5.14. For the EHM case, b), on axis modes clearly grow faster than in the corresponding CHM, a), case. The initial conditions were $\psi_0 = 0.01\frac{m^2}{s}$, $\vec{p} = (0, 10)$ $\vec{q} = (2, 2)$, $\rho_s = 0.6m$, $v_\star = 10\frac{m}{s}$, and $M = 0.36$

5.5 Streamers

Streamers are radially extended flows. In the context of the EHM solution they may be viewed as the 'opposite' of zonal flows as they have $k_x = 0$ and $k_y \sim 1$. The radially extension of streamers could lead to large amounts of radial transport. We begin investigating streamers here with an analytical growth map generated with $\vec{p} = (10, 11)$, shown in figure 5.16. This map takes a form similar to those presented in section 5.3.2 but rotated around a point at $\vec{k} = (0, 0)$. In general maps generated for cases where $p_x \neq 0$ can be more complicated than those presented earlier in this chapter. We designate the streamer as the mode with $\vec{k} = (0, 1)$, figure 5.16 shows that this mode is far from the region where strong growth is indicated. This will become important for explaining the failure of the 4MT model later in this section.

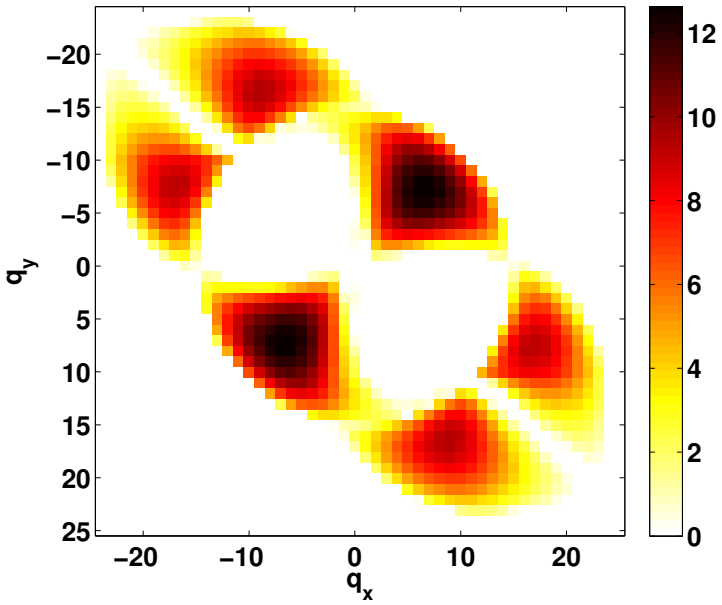

Figure 5.16: A map of the growth rate of perturbing mode $\vec{q}$ for a system with $\vec{p} = (10, 11)$, $\rho_s = 0.6m$, $v_\star = 10\frac{m}{s}$ and $\phi_0 = 0.1\frac{m^2}{s}$.

First we present the growth of the mode $\vec{q} = (0, 1)$ in a system initialised with $\vec{p} = (10, 11)$, $\vec{q} = (0, 1)$ and $\vec{p_\pm} = \vec{p} \pm \vec{q}$ in figure 5.17. All figures in this

section are normalised to the linear growth time of this streamer. It can be seen that at very early times the ODEs capture the oscillations of the streamer, but at $t/\tau \sim 0.25$ the full simulation rapidly diverges from the predictions. This can be better appreciated in the real space images presented in figure 5.18 where it can be seen that the system in fact transitions from an off axis drift-wave to a largely zonal configuration at this time.

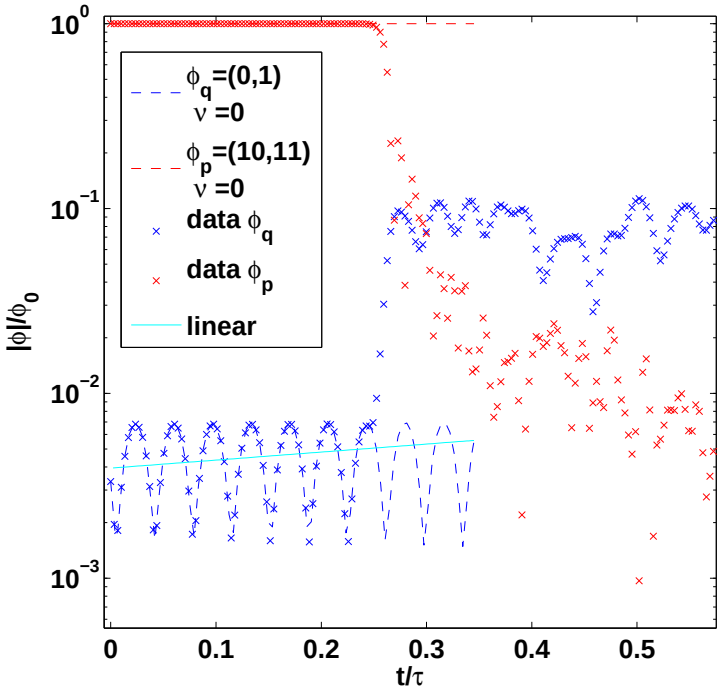

Figure 5.17: A streamer case initialied with $\vec{p} = (10, 11)$, $\vec{q} = (0, 1)$, $\rho_s = 0.6m$, $v_\star = 10\frac{m}{s}$ and $\phi_0 = 0.05\frac{m^2}{s}$. It can be seen that at $t \sim 0.25\tau$ the real system rapidly diverges from both the ODEs and the linear prediction.

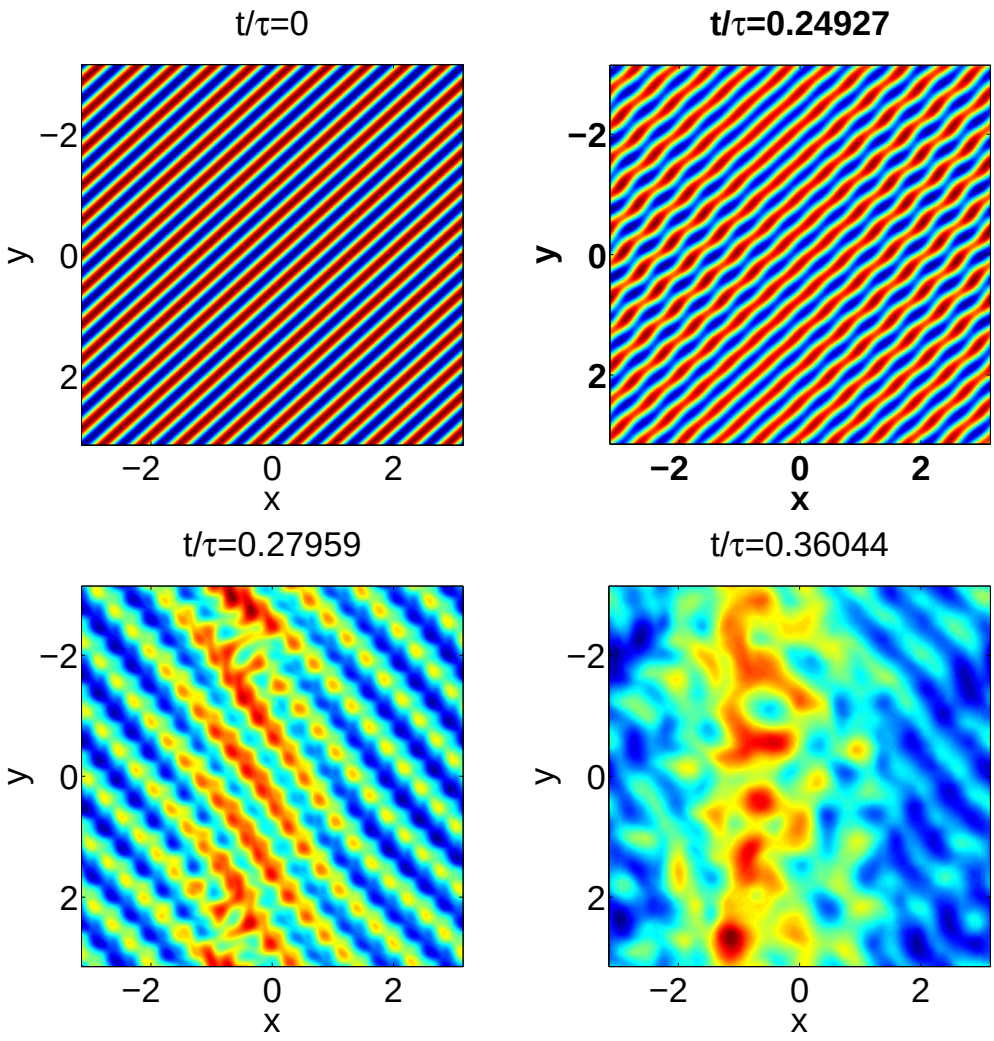

Figure 5.18: Real space images of potential corresponding to the case presented in figure 5.17. Dispite being intiallised with a perturbation designed to form a streamer, the system develops a mostly zonal configuration.

Investigating the Fourier space images of this system, for example figure 5.19, it can be seen that the mode $\vec{k} = (7, -6)$ has been grown by the system. This mode is near the maximum growth rate shown in the analytical growth map 5.16. Assuming that this mode is in fact $\vec{q}$ gives a system with $\vec{p} = (10, 11), \vec{q} = (7, -6), \vec{p_+} = (17, 5), \vec{p_-} = (3, 17)$. This is significant as the mode $\vec{k} = (17, 5)$ can couple strongly to the zonal flow $\vec{q}_{\text{zonal}} = (1, 0)$.

The behaviour of the system is more complex than the zonal flow cases discussed before in this chapter. Near to resonance ($\Delta_\pm \approx 0$) equations (5.28) and (5.29) require that the satellite modes grow at the same rate as perturbing mode $\vec{q}$, hence $\vec{p_+} = (17, 5)$ must grow at the same rate as $\vec{q} = (7, -6)$. In total this means that the growth of $\vec{q}_{\text{zonal}}$ can be described by a system with $\vec{p} = (17, 5)$ where $\frac{\partial}{\partial t}\varphi_{\vec{p}} = \frac{\partial}{\partial t}\varphi_0 \neq 0$.

To take this growth into account a linear forcing term can be added to the ODEs and the dispersion relation. The derivation of this is left until chapter 7 but the results are shown here in figure 5.20, an appropriate forcing term has been added to the driving mode and both satellite modes. It can be seen that the ODEs and the linear prediction, now calculated using the technique discussed in section 7.3, capture the correct growth rate. By $t/\tau \sim 0.26$, where τ is still the linear growth time of the initial system studied in this section, the system has finished growing and begun to saturate. This explains the rapid departure from the ODE predictions for the streamer at this point; the system is already saturating and is influenced by far more than four modes so that the ODE model is no longer applicable. We were unable to reproduce the growth of streamers seen in [Manfredi et al., 2001]. As we do not suppress the growth of modes outside of the initial conditions the system always grew modes that caused a transition to a zonal flow.

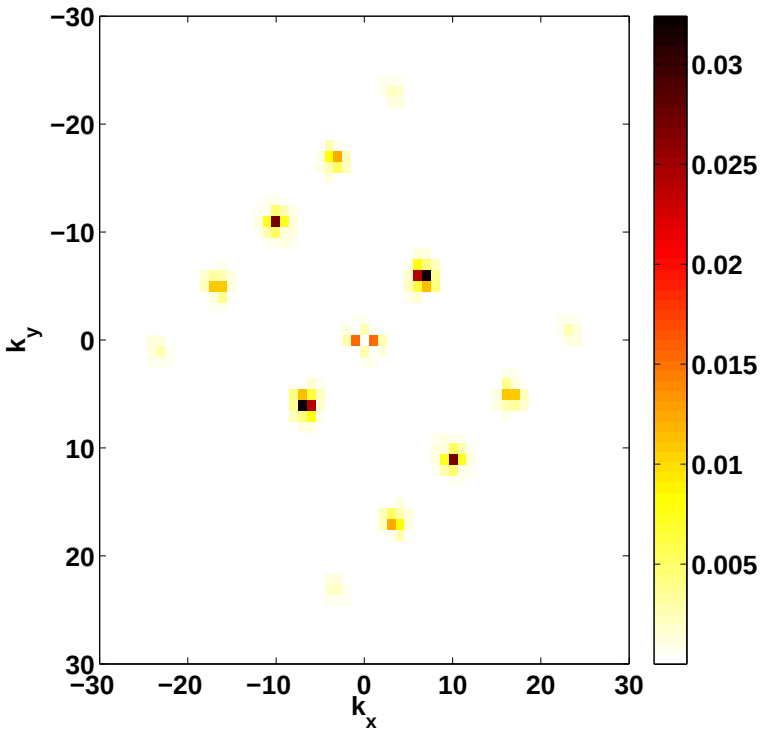

Figure 5.19: A fourier transform of the same simulation as figures 5.17 and 5.18 at $t = 0.26\tau$. It can be seen that a number of modes not in the initial conditions have been grown.

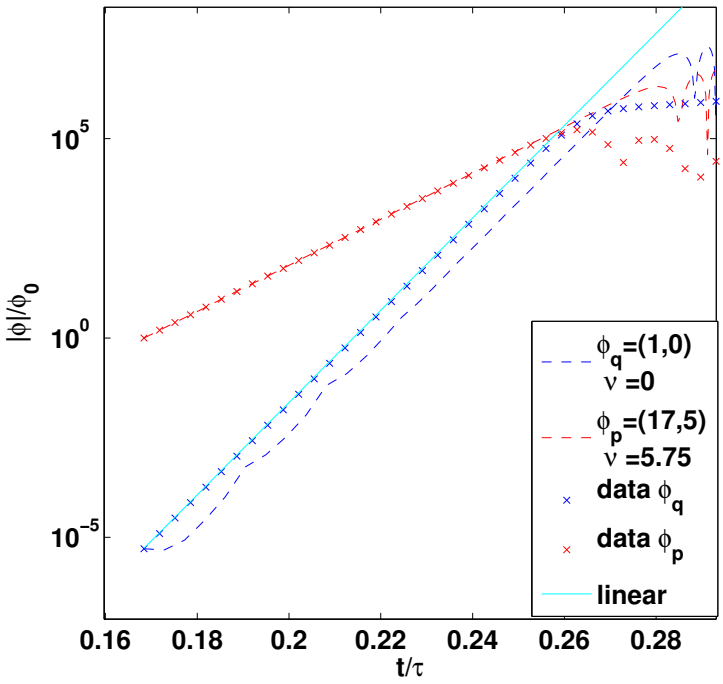

Figure 5.20: ODE and linear predictions for the growth of the zonal mode by treating the system as if it has $\vec{p} = (17, 5)$ and $\vec{q} = (1, 0)$. The satellite modes, $\vec{p}_{\pm}$, and the pump wave, $\vec{p}$, have been driven to simulate their growth in the real system.

5.6 Conclusions

We have presented a systematic analysis of the finite Larmor radius effects on the modulational instability of the Extended-Hasegawa-Mima equation. Our approach was to directly compare predictions of the fully nonlinear four mode truncated model with pseudospectral simulations of the full EHM equation. We have examined not only the case where the modulating wave is perpendicular to a purely meridional ($k_x = 0$) pump wave, but also a more generic oblique case. The main methodology is that based on comparing linear growth rates of the analytical four mode system and modes observed in numerical PDE simulations. We have used linear growth rate maps to demonstrate a broadening of growing modes when the Larmor radius, ρ_s, is varied.

It should be noted that, despite the accuracy of the analytical predictions, in all full simulation cases, higher harmonics of the initial modes and, in the later stage of the evolution, a broadband spectrum of modes are produced via nonlinear interactions. This ability to grow additional modes that are not part of the initial conditions is of particular relevance to the streamer case. We were unable to grow a streamer in the EHM system as additional modes were grown which coupled strongly to zonal flows. Once these additional modes were present the growth rate of the zonal flow was significantly faster than the streamer, and the final state of the system was therefore predominantly zonal.

A key control parameter M_ρ, dependent on the Larmor radius, has been constructed and it allowed us to alternate between different dynamical regimes of the MI evolution. For large values of M_ρ we find a saturating state that ultimately settles on a zonal configuration, even if the initial perturbing wave is oblique to the vector of the pump wave. For small M_ρ, the oblique case often deviates from analytical predictions and shows rapid oscillations. For a weak nonlinearity in the CHM case, the oblique modes are sometimes the fastest growing modes in the system and this leads to a final state which is off-axis with respect to the zonal direction. Interestingly, for the equivalent EHM case the zonal modes grow most rapidly, yet the system settles on a similar off-zonal final configuration.

Chapter 6

Four-Mode Interactions in the Hasegawa-Wakatani System

6.1 Introduction

The major shortcoming of the Hasegawa-Mima model, used in chapter 5, is its inability to spontaneously generate drift-waves and large turbulent fluctuations, making prescribed initial conditions necessary. This initial value approach is not ideal for describing fusion plasma behaviour, which is always measured in its fully nonlinear state. The lack of instability in the EHM equation is a result of the adiabatic electron response to electrostatic perturbations, which can instantaneously enforce an ideal Boltzmann relation between density and the electrostatic potential, as given by equations (3.2) and (3.26) for the non extended and extended cases respectively. The Hasegawa-Wakatani model relaxes this restraint and assumes that the density response is coupled to the potential via electron dynamics in the direction parallel to the magnetic field as described in chapter 3. In this work the 'Extended'-Hasegawa-Wakatni equation refers to the case where the zonal components of density and potential have been removed from the current describing the parallel electron dynamics[Dorland and Hammett, 1993; Numata et al., 2007], not the addition of a curvature term as is seen in [Dewhurst et al., 2009].

The removal of the adiabatic assumption leads to a two field model – the Hasegawa-Wakatani equations – consisting of a coupled set of equations for density and potential. In addition these now describe fluctuations around a mean value. This is a much more 'physical' model and is considerably more complex than the one field Hasegawa-Mima model.

The separation of density and potential fluctuations allows their relative

phases to be shifted, as described in sections 1.4 and 1.7.1, and as such each mode in the EHW system is linearly unstable. This means that, unlike the Hasegawa-Mima system, it is neither reasonable nor desirable to consider an initial condition consisting of four modes. The growth of a spectrum of drift waves by the Hasegawa-Wakatani equations, as described by equation 3.80, is more applicable to real systems. Nevertheless, four-wave interactions do occur and are important in describing the evolution of the system. In the past this model has been used to study the generation and stability of zonal flows[Numata et al., 2007] as well as the interaction between zonal-flows and drift-waves[Scott, 2005].

This chapter begins with the derivation of an analytical ODE model. In this case a truncation to four modes was made for both the density and potential equations in the EHW system, which results in eight coupled ODEs. As for the EHM system, these describe the behaviour of a driving wave, zonal perturbation, and sidebands, however for each of these there is now an equation for density and potential. Unlike the model used in chapter 5, we do not specify these modes beforehand in our PDE simulations. Instead we allow the system to grow a drift wave spectrum and select a resonant set of waves to compare with our ODE equations. In practice the wave selected for use as the pump wave is one of the most unstable waves in the system. In this case stationary solutions for the ODEs cannot be found, but a linear approximation is made by considering the case where the satellites grow at the same rate as the pump wave.

Finally, a numerical code to solve the Extended-Hasegawa-Wakatani equations was developed using the techniques described in chapter 4. Predictions from the ODEs and the linear growth rate were compared to this full PDE simulation.

6.2 A truncated model for the Hasegawa-Wakatani equations

As with the EHM system the derivation of the 4 mode truncated extended Hasegawa-Wakattani system starts from the Fourier space representation of the EHW equations, (3.59) and (3.60), which takes the form:

$$\partial_t \mathcal{N}_{\vec{k}} = -i(1+k^2)\Omega_k \Phi_{\vec{k}} + z\alpha(\Phi_{\vec{k}} - \mathcal{N}_{\vec{k}}) - \sum_{k_1,k_2} R(k_1,k_2)\Phi_{\overrightarrow{k_2}}\mathcal{N}_{\overrightarrow{k_1}}\delta_{\vec{k},\overrightarrow{k_1}+\overrightarrow{k_2}} \tag{6.1}$$

$$\partial_t \Phi_{\vec{k}} = -\frac{\alpha z}{k^2}(\Phi_{\vec{k}} - \mathcal{N}_{\vec{k}}) - \sum_{k_3,k_4} T(k,k_3,k_4)\Phi_{\overrightarrow{k_3}}\Phi_{\overrightarrow{k_4}}\delta_{\vec{k},\overrightarrow{k_3}+\overrightarrow{k_4}} \tag{6.2}$$

where $z = 1 - \delta_{s,1}\delta_{k_y,0}$ and s is a switching parameter, so that s=1 represents the EHW case and s=0 the non-extended case. Due to the normalisations used in section 3.2.2 this equation is unitless. As with the EHM simulations, the PDE simulations themselves were initialised in real space and had the form $\Phi_{\vec{k}}(\vec{x}) = A_{\vec{k}} sin(\frac{2\pi}{L}\vec{k}\vec{x})$, so $\vec{k}$ represents integer wave numbers.

For clarity we rewrite the frequency and coupling parameters in equations (6.2) and (6.1) here as

$$\Omega_k = \frac{\kappa k_y}{1 + k^2}, \tag{6.3}$$

$$R(k_1, k_2) = (k_{1x}k_{2y} - k_{2x}k_{1y}) \tag{6.4}$$

and

$$T(k, k_3, k_4) = \frac{k_3^2(k_{3x}k_{4y} - k_{4x}k_{3y})}{k^2}, \tag{6.5}$$

Again we write

$$\Phi = \Phi_{\vec{p}} + \Phi_{\vec{q}} + \Phi_{\vec{p_+}} + \Phi_{\vec{p_-}},$$

$$\mathcal{N} = \mathcal{N}_{\vec{p}} + \mathcal{N}_{\vec{q}} + \mathcal{N}_{\vec{p_+}} + \mathcal{N}_{\vec{p_-}},$$

with

$$\vec{p_\pm} = \vec{p} \pm \vec{q}, \tag{6.6}$$

and substitute these into equations (6.1) and (6.2). Following the same procedure as in section 5.2, defining

$$\Phi_{\vec{k}} = \varphi_{\vec{k}}(t)e^{-i\Omega_k t} \tag{6.7}$$

and

$$\mathcal{N}_{\vec{k}} = N_{\vec{k}}(t)e^{-i\Omega_k t}, \tag{6.8}$$

we write ODE equations for the Fourier mode amplitudes of electrostatic potential

fluctuations as

$$\frac{d}{dt}\varphi_p(t) = \varphi_p(t)\, i\Omega_p + \frac{z\alpha\left(N_p(t) - \varphi_p(t)\right)}{p^2} \tag{6.9}$$
$$- \left(T(p,p_-,q)\,\varphi_q(t)\,\varphi_{p_-}(t) + T(p,q,p_-)\,\varphi_{p_-}(t)\,\varphi_q(t)\right) \mathrm{e}^{it\Delta_-}$$
$$- \left(T(p,-q,p_+)\,\varphi_{p_+}(t)\,\overline{\varphi_q(t)} + T(p,p_+,-q)\,\overline{\varphi_q(t)}\varphi_{p_+}(t)\right) \mathrm{e}^{it\Delta_+}$$
$$\frac{d}{dt}\varphi_q(t) = \varphi_q(t)\, i\Omega_q + \frac{z\alpha\left(N_q(t) - \varphi_q(t)\right)}{q^2} \tag{6.10}$$
$$- \left(T(q,-p_-,p)\,\varphi_p(t)\,\overline{\varphi_{p_-}(t)} + T(q,p,-p_-)\,\overline{\varphi_{p_-}(t)}\varphi_p(t)\right) \mathrm{e}^{-it\Delta_-}$$
$$- \left(T(q,p_+,-p)\,\overline{\varphi_p(t)}\varphi_{p_+}(t) + T(q,-p,p_+)\,\varphi_{p_+}(t)\,\overline{\varphi_p(t)}\right) \mathrm{e}^{it\Delta_+}$$
$$\frac{d}{dt}\varphi_{p_-}(t) = \varphi_{p_-}(t)\, i\Omega_{p_-} + \frac{z\alpha\left(N_{p_-}(t) - \varphi_{p_-}(t)\right)}{{p_-}^2} \tag{6.11}$$
$$- \left(T(p_-,-q,p)\,\varphi_p(t)\,\overline{\varphi_q(t)} + T(p_-,p,-q)\,\overline{\varphi_q(t)}\varphi_p(t)\right) \mathrm{e}^{-it\Delta_-}$$
$$\frac{d}{dt}\varphi_{p_+}(t) = \varphi_{p_+}(t)\, i\Omega_{p_+} + \frac{z\alpha\left(N_{p_+}(t) - \varphi_{p_+}(t)\right)}{{p_+}^2} \tag{6.12}$$
$$- \left(T(p_+,q,p)\,\varphi_p(t)\,\varphi_q(t) + T(p_+,p,q)\,\varphi_q(t)\,\varphi_p(t)\right) e^{it\Delta_+}.$$

Similarly, for density fluctuations we have:

$$\begin{aligned}\frac{d}{dt}N_p(t) &= \left(z\alpha - i\Omega_p\left(1+p^2\right)\right)\varphi_p(t) \\ &+ \left(i\Omega_p - z\alpha\right)N_p(t) \\ &- \left(R(-q,p_+)\,\varphi_{p_+}(t)\,\overline{N_q(t)} + R(p_+,-q)\,\overline{\varphi_q(t)}N_{p_+}(t)\right)\mathrm{e}^{i\Delta_+ t} \\ &- \left(R(p_-,q)\,\varphi_q(t)\,N_{p_-}(t) + R(q,p_-)\,\varphi_{p_-}(t)\,N_q(t)\right)\mathrm{e}^{i\Delta_- t},\end{aligned} \tag{6.13}$$

$$\begin{aligned}\frac{d}{dt}N_q(t) &= \left(z\alpha - i\Omega_q\left(1+q^2\right)\right)\varphi_q(t) \\ &+ \left(i\Omega_q - z\alpha\right)N_q(t) \\ &- \left(R(-p_-,p)\,\varphi_p(t)\,\overline{N_{p_-}(t)} + R(p,-p_-)\,\overline{\varphi_{p_-}(t)}N_p(t)\right)\mathrm{e}^{-it\Delta_-} \\ &- \left(R(p_+,-p)\,\overline{\varphi_p(t)}N_{p_+}(t) + R(-p,p_+)\,\varphi_{p_+}(t)\,\overline{N_p(t)}\right)\mathrm{e}^{it\Delta_+},\end{aligned} \tag{6.14}$$

$$\begin{aligned}\frac{d}{dt}N_{p_-}(t) &= \left(z\alpha - i\Omega_{p_-}\left(1+{p_-}^2\right)\right)\varphi_{p_-}(t) \\ &+ \left(i\Omega_{p_-} - z\alpha\right)N_{p_-}(t) \\ &- \left(R(p,-q)\,\overline{\varphi_q(t)}N_p(t) + R(-q,p)\,\varphi_p(t)\,\overline{N_q(t)}\right)\mathrm{e}^{-it\Delta_-},\end{aligned} \tag{6.15}$$

$$\begin{aligned}\frac{d}{dt}N_{p_+}(t) &= \left(z\alpha - i\Omega_{p_+}\left(1+{p_+}^2\right)\right)\varphi_{p_+}(t) \\ &+ \left(i\Omega_{p_+} - z\alpha\right)N_{p_+}(t) \\ &- \left(R(q,p)\,\varphi_p(t)\,N_q(t) + R(p,q)\,\varphi_q(t)\,N_p(t)\right)\mathrm{e}^{-it\Delta_+}.\end{aligned} \tag{6.16}$$

Symbols Δ_+ and Δ_- are again given by equation (5.13), and, in this case are:

$$\begin{aligned}\Delta_- &= \Omega_p - \Omega_q - \Omega_{p_-}, \\ \Delta_+ &= \Omega_p + \Omega_q - \Omega_{p_+}.\end{aligned} \tag{6.17}$$

For all of the ODEs, the vector notation for the subscripts and coupling coefficient arguments has been dropped.

6.3 The linear growth rate

Unlike chapter 5 it is not possible to derive a linear solution for this ODE model. The primary instability of the Extended-Hasegawa-Wakatani system means that the pump wave and sidebands are all time dependant and resonance conditions such as (5.28) and (5.29) cannot be used to produce an eigenvalue problem.

Instead we consider the smooth form of the primary dispersion relation, in particular the imaginary part, examples of which were shown in figure 3.2.4.

Restricting ourselves to cases where $q \ll p$ we make the statement that $p_\pm = p \pm q \sim p$. In this case the growth rate due to the primary instability, ν_k, is the same for the satellite modes as the driving mode, from here on we will label it G.

Using this assumption we state that every wave except the zonal perturbations, φ_q and N_q, grows as

$$\varphi_k(t) = \psi_k e^{-i\omega_k t} e^{Gt},$$
$$N_k(t) = n_k e^{-i\omega_k t} e^{Gt},$$

where $\omega_k \in \mathbb{R}$, $G \in \mathbb{R}$, $\frac{d}{dt}G = 0$ and $G > 0$.

Substituting these definitions into equations (6.10) and (6.14) leads to

$$\frac{d}{dt}\varphi_q(t) = \varphi_q(t)\, i\Omega_q + \frac{z\alpha\left(N_q(t) - \varphi_q(t)\right)}{q^2} - \left(C_- e^{-it\Delta_-} + C_+ e^{it\Delta_+}\right) e^{2Gt} \quad (6.18)$$

and

$$\frac{d}{dt}N_q(t) = \left(z\alpha - i\Omega_q\left(1+q^2\right)\right)\varphi_q(t) + \left(i\Omega_q - z\alpha\right) N_q(t) - \left(D_- \mathrm{e}^{-it\Delta_-} + D_+ \mathrm{e}^{it\Delta_+}\right) e^{2Gt}, \quad (6.19)$$

where the nonlinear coupling terms and the ψ_k and n_k constants have been collected into the $C_\pm$ and $D_\pm$ terms. In section 3.2.4 it was shown that a zonal mode with $k_y = 0$ could not be grown from the linear terms, therefore only the last term in each of equations (6.18) and (6.19) will cause the mode to grow. Keeping only this term, and assuming the system is in resonance ($\Delta_\pm = 0$), the only time dependence remaining on the right hand side is e^{2Gt}. This indicates that φ_q and N_q must grow linearly, with linear growth rate $\gamma = 2G$, as time is normalised in this system γ is unitless . As with the EHM case discussed in chapter 5, we define a linear growth time $\tau = \frac{1}{\gamma}$.

6.4 Numerical Results

As with the Hasegawa-Mima four mode truncation, the reduced model for the EHW system was compared to numerical simulations of the full system. It should be emphasised that we do not truncate the full simulations. All modes are allowed to evolve and we select sets that fit resonance condition (5.2) for comparison with the analytical predictions. The simulations are split into two classes, simulations carried out in the HW regime where $\alpha < 1$ and the EHM limit where $\alpha \gg 1$.

6.4.1 The EHM limit

In phase initial conditions

Firstly a case with $\kappa = 10$ and $\alpha = 10$ was considered in the EHW system. Low amplitude random noise was generated at the grid scale and used as the initial condition for both density and potential. Artificial viscosity was applied to the higher modenumbers to avoid aliasing problems. The development of the system in real space is shown in figure 6.1. Three stages are shown, the first is where the system has developed drift waves, the second is a transitional phase where the system has begun rolling into vortices, and the final panel shows a zonal state. Individual vortices are still present, as is particularly visible in the density panel, but the overall form of the system has bands in the vertical (poloidal) direction.

The potential in a drift wave dominated stage is shown in figure 6.2 (left). At this point of the dynamical evolution the Fourier transform of potential was computed and the results are shown in figure 6.2 (right). From this Fourier space picture a set of modes, namely $\vec{p} = (0, -\frac{2\pi}{L} \times 9) = (0, -1.414)$ and $\vec{q} = (\frac{2\pi}{L}, 0) = (0.157, 0)$, were chosen for comparison to the reduced model as they satisfied the condition $q \ll p$, had both satellite modes present, and had a relatively strong amplitude. The driving mode, $\vec{p}$, is close to the most unstable mode from the primary instability, which is at $\vec{k}_{max} = (0, \pm\frac{2\pi}{L} \times 8)$.

As with the EHM system the ODEs were solved with a built in Matlab Rungge-Kutta (RK45) solver. Their values at $t = 0$ in the full system were used as initial conditions. The results of these simulations can be seen in figure 6.3 where amplitudes measured from the full simulation are compared with solutions of the ODE equations, (6.9) to (6.16). It can be see that at very early times density grows more rapidly than potential, until a phase difference has been established between them, at which point the pump waves, φ_0 and N_0, grow linearly. The zonal modes, φ_q and N_q, show very little growth until $t \sim 5\tau$, where τ is the inverse of the linear growth rate defined in section 6.3, at which point they begin to grow at approximately twice the primary growth rate of φ_p. The linear growth phase continues until $t \sim 11\tau$.

The ODEs predict the correct growth rate for density and potential for mode $\vec{p}$, which matches the primary growth rate predicted by equation (3.81), as well as capturing the small adjustment they make at $t \approx 0$.

For mode $\vec{q}$ the initial agreement is again good, however the time at which the zonal mode starts to grow differs. Despite this the ODEs capture approximately the correct growth rate for the system. As with the EHM case the ODEs for the

zonal modes take some time to begin growing linearly. Considering section 6.3 and the M_ρ parameter discussed in chapter 5 this can be considered as a threshold problem. The system must be sufficiently nonlinear that its evolution is dominated by the nonlinear terms in equations (6.18) and (6.19), at which point it will grow linearly with growth rate γ. Unlike the ODE predictions for the EHM equation, the full system begins to saturate and oscillate considerably earlier than the ODE predictions. This is not surprising as the full system in this case has significant contributions from modes that are not included in the truncated model.

A line denoting twice the primary growth grate of φ_p is also shown in figure 6.3. It shows good agreement suggesting that during the linear growth phase the approximations made in section 6.3 are valid.

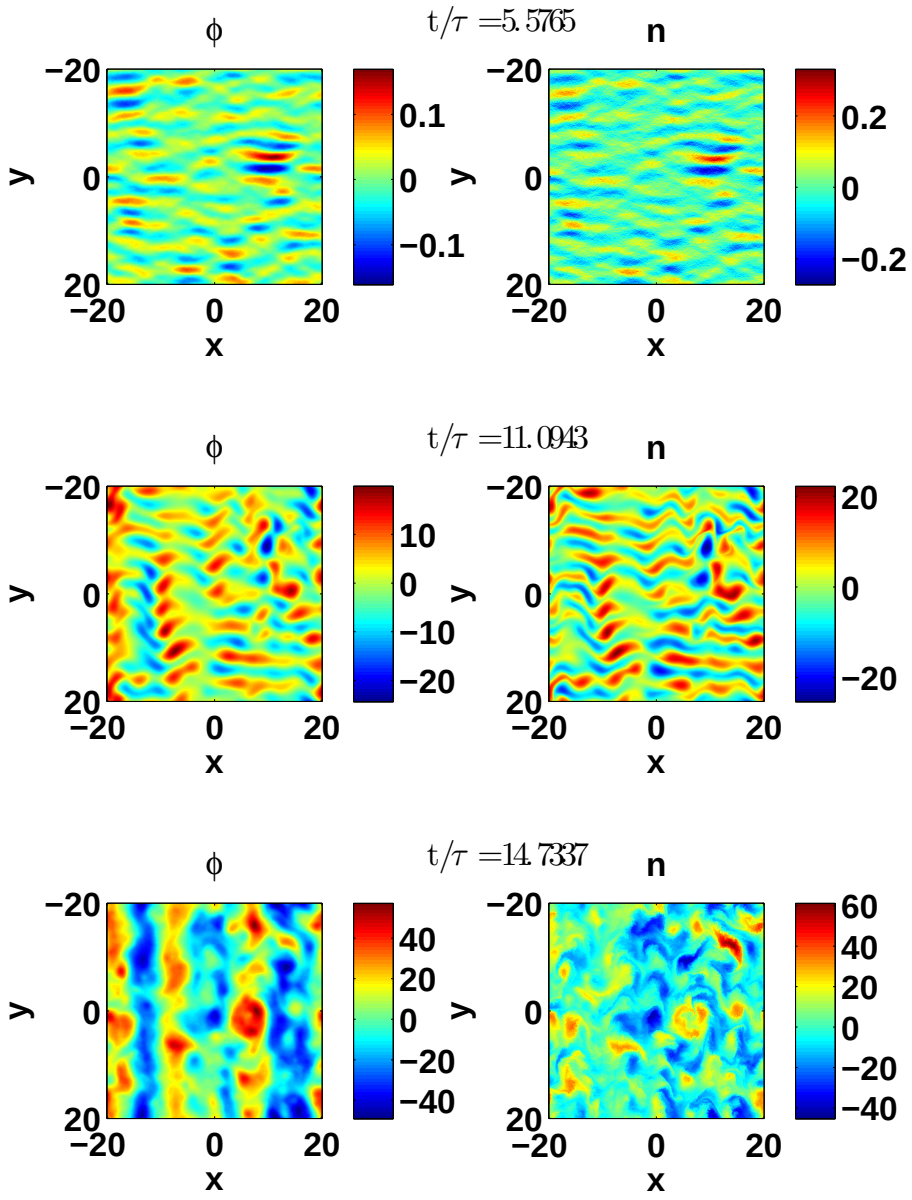

Figure 6.1: The evolution of potential and density in a system with with $\alpha = 10$ and $\kappa = 10$. The roll up of drift waves to form zonal flows can be seen most clearly in potential.

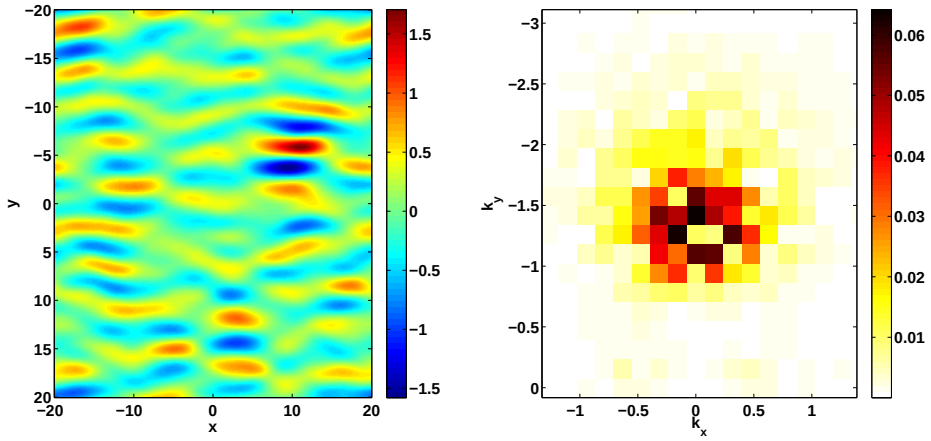

Figure 6.2: The potential in a EHW simulation with $\alpha = 10$ and $\kappa = 10$ at $\frac{t}{\tau} \sim 8.1$. From the potential (left) it can be seen that the system has developed drift waves. From the Fourier transform of this potential (right) it can be seen that the set of modes formed with $\vec{p} = (0, -1.41)$ and $\vec{q} = (0.157, 0)$ form a possible resonant set for use in the ODE equations.

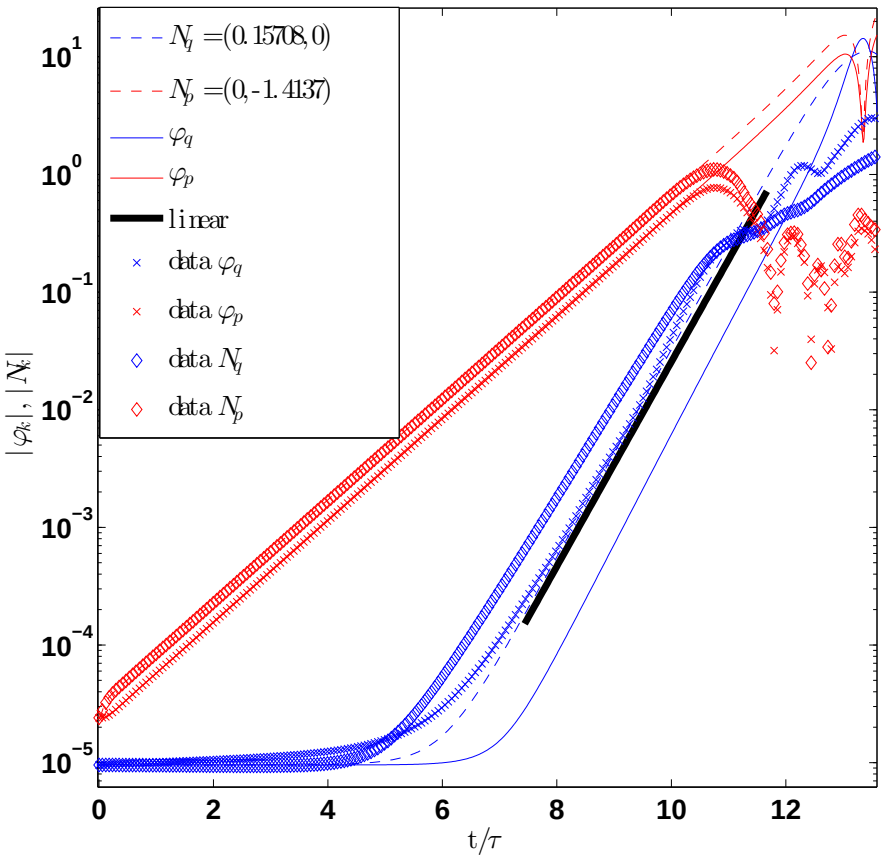

Figure 6.3: A comparison between the ODE predictions (lines) and the PDE simulation (markers) for a high $\alpha = 10$ case. The line labelled linear is positioned arbitrarily but grows at the twice the rate predicted by the primary dispersion relation for φ_p.

Random initial condition

The system was next initialised with white noise that was generated for potential and density independently. The primary instability was allowed to develop drift waves as before, and examining the Fourier space images of potential suggested that this time the set of waves with $\vec{p} = (0, -\frac{2\pi}{L} \times 8) = (0, -1.2566)$ and $\vec{q} = (\frac{2\pi}{L}, 0) = (0.157, 0)$ were most appropriate for investigating the MI.

Figure 6.4 shows the development of the modes $\vec{p}$ and $\vec{q}$ as the simulation progresses, again measurements taken from the full simulation (markers) are compared with results from the ODE equations (lines). It can be seen that at early times the system rapidly adjusts so that the pump waves, φ_0 and N_0, are simply phase shifted, at which point they begin to grow linearly. The ODEs capture this behaviour well. The zonal modes however take ~ 6 linear growth times to adjust, and even when they have done so the density deviates from pure linear growth, due to interactions with modes not considered in the four-wave truncation. The ODEs still capture the correct linear growth rate, which is approximately twice the primary growth rate of φ_p as demonstrated by the line labelled 'linear' in the figure.

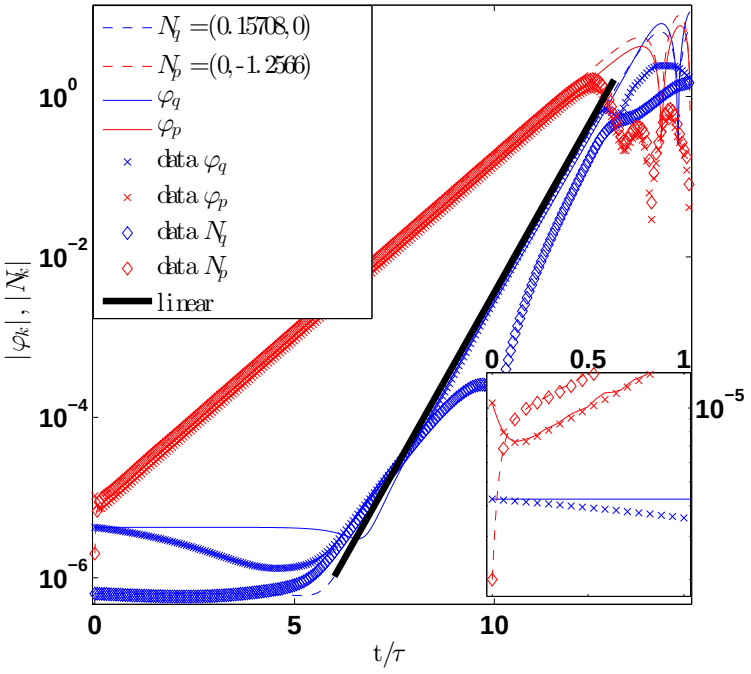

Figure 6.4: A comparison between the ODE predictions (lines) and the PDE simulation (markers) for a high $\alpha = 10$ case. Density and potential were seeded independently with white noise. The line labelled linear is positioned arbitrarily but grows at twice the primary growth rate of φ_p. The inset figure shows the evolution at early times.

6.4.2 The EHW regime

In phase initial conditions

The same procedure as section 6.4.1 was carried out, only this time with $\alpha = 0.5$ and $\kappa = 10$. This range of parameters is known to give a reasonable qualitative agreement between simulated turbulence and that observed in fusion plasma[Horton, 1999; Dudok de Wit et al., 1995].

The development of the system in real space is shown in figure 6.5. As for the high α case three stages are shown. This time the drift waves developed are broader as the system is driven at lower k numbers. The transition still shows the system rolling into vortices, only now they are large, and the final panel shows a zonal state with broad zones. As before individual vortices are still present.

Figure 6.6 again shows the potential at a time when drift waves have become dominant ($\frac{t}{\tau} \sim 6.2$) and its Fourier transform. This time the centre of the Fourier space potential profile is closer to $|k| = 0$ and the best candidates to explore the 4MT are $\vec{p} = (0, -\frac{2\pi}{L} \times 3) = (0, -0.471)$ and $\vec{q} = (\frac{2\pi}{L}, 0) = (0.157, 0)$.

Again the ODEs are initialised using values from the full simulation at $t = 0$ and compared to the full simulation, shown in figure 6.7. As before mode $\vec{p}$ shows the correct growth rate and behaviour at early times, however the agreement for $\vec{q}$ is not as good. Again the system takes a short while (~ 5 linear growth times) to settle on the correct eigenvector and whilst this is happening the amplitude of potential for mode $\vec{q}$ decreases whilst its density amplitude increases. Even during the linear growth phase the potential for $\vec{q}$ does not grow entirely linearly.

As before the real system begins to oscillate before the ODEs and, while it is in the linear phase, the zonal wave grows at approximately twice the rate of the pump wave.

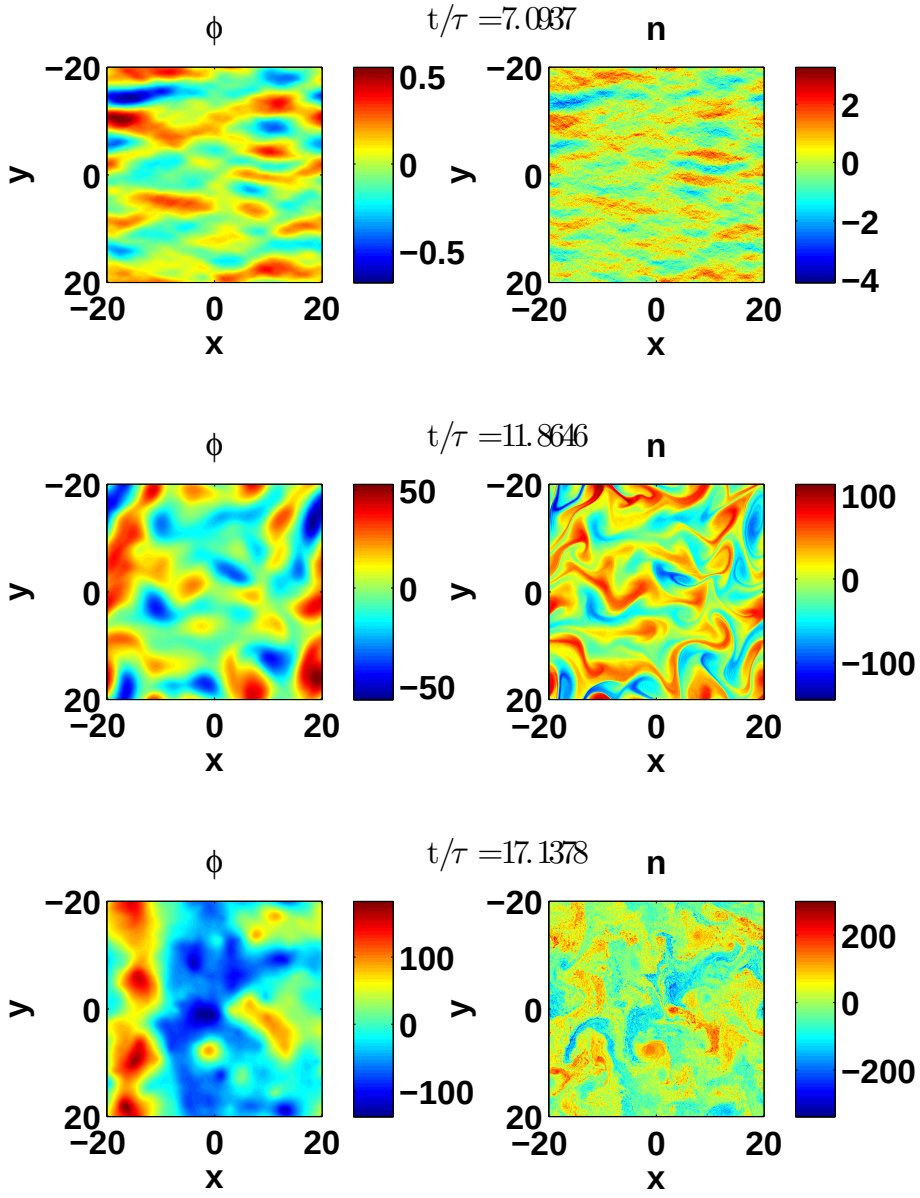

Figure 6.5: The evolution of potential and density in a system with with $\alpha = 0.5$ and $\kappa = 10$. The roll up of broad drift waves to form wide zonal flows can be seen.

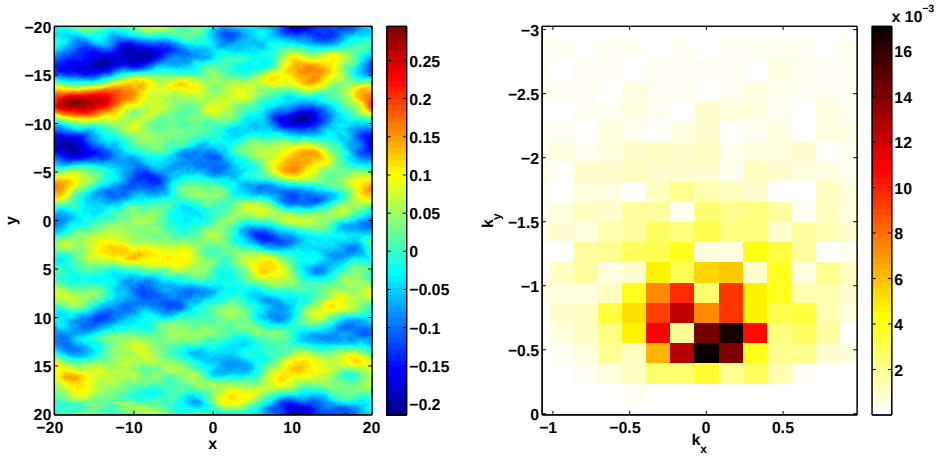

Figure 6.6: The potential in a EHW simulation with $\alpha = 0.5$ and $\kappa = 10$ at $\frac{t}{\tau} \sim 6.2$. From the potential (left) it can be seen that the system has developed drift waves. From the Fourier transform of this potential (right) it can be seen that the set of modes formed with $\vec{p} = (0, -0.471)$ and $\vec{q} = (0.157, 0)$ form a possible resonant set for use in the ODE equations.

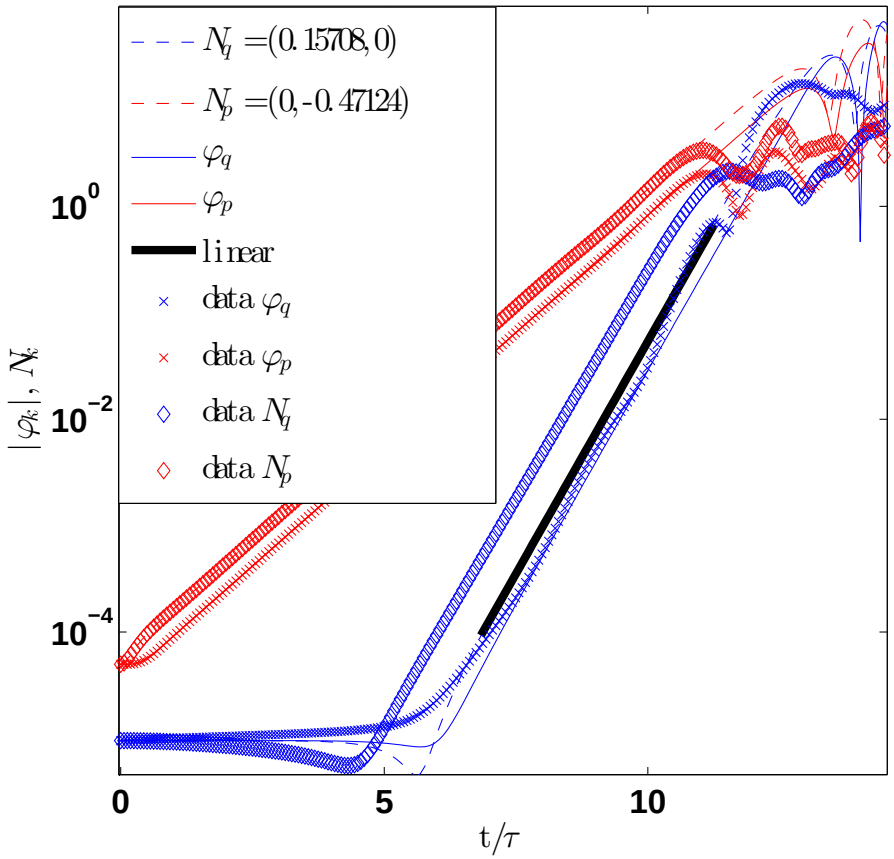

Figure 6.7: A comparison between the ODE predictions (lines) and the PDE simulation (markers) for a low $\alpha = 0.5$ case. The line labelled linear is positioned arbitrarily but grows twice the rate predicted by the primary dispersion relation for φ_p.

Random initial condition

As for the high α EHM limit case, the system is now initialised with white noise generated independently for density and potential. The Fourier space images suggested that the best system to investigate was formed by $\vec{p} = (0, -\frac{3\times 2\pi}{L}) = (0, -0.4712)$ and $\vec{q} = (\frac{2\pi}{L}, 0) = (0.157, 0)$. The results are shown in figure 6.8. As for the previous case with random initial conditions the system very rapidly adjusts until the density and potential pump waves are simply phase shifted, at which point they begin to grow linearly. The exact progression of the zonal modes is different at early times ($\frac{t}{\tau} \sim 1 - 7$), but once they become of comparable amplitude they grow at approximately the linear growth rate. As before the full system saturates before the ODEs finish growing linearly. In this case the line labelled 'linear' is only a good fit for the ODE for density. The real system grows at approximately this rate, but deviates from linear growth and the ODE for potential has a strong oscillating component. This is perhaps unsurprising as the primary instability is more compressed for the $\alpha = 0.5$ case, so there will be a greater difference in the primary growth rate of the driving and satellite modes.

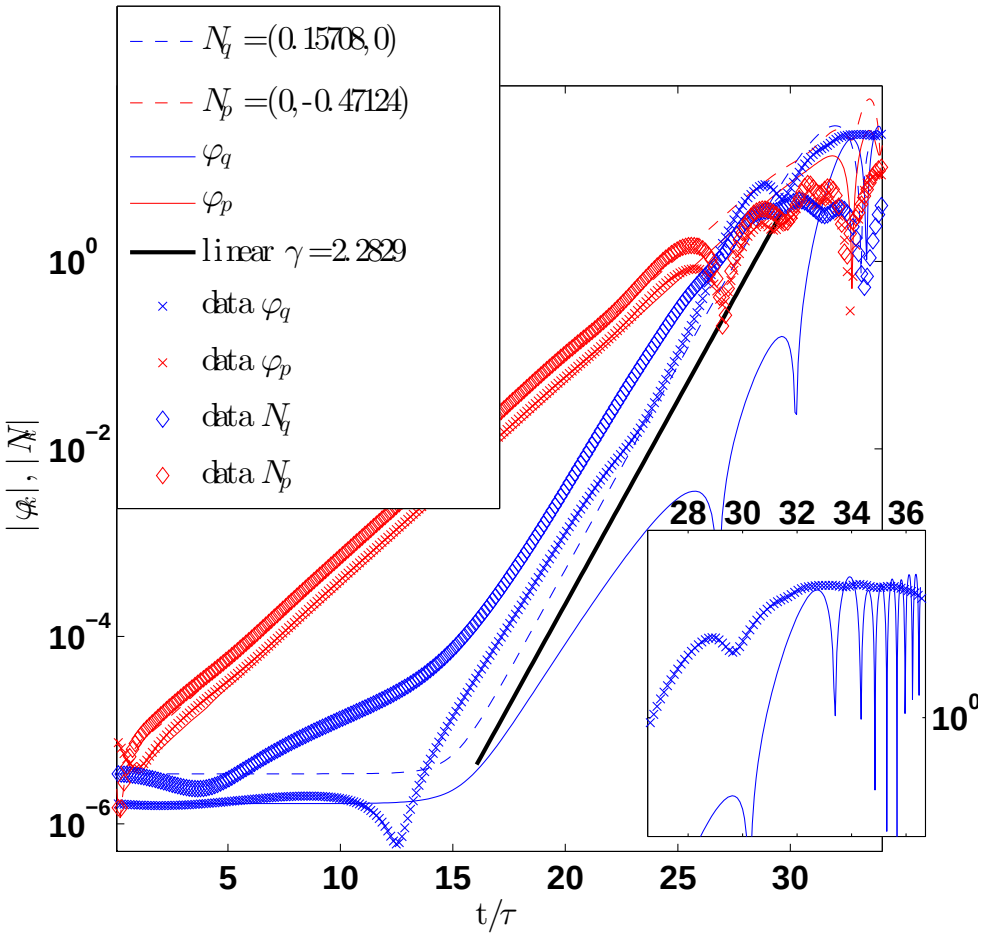

Figure 6.8: A comparison between the ODE predictions (lines) and the PDE simulation (markers) for a low $\alpha = 0.5$ case. Density and potential were seeded independently with white noise. The line labelled linear grows at twice the primary growth rate of φ_p. The inset figure shows the saturation of potential, φ_q, in more detail.

6.5 Energy Transfer functions

While investigating the ODE model for the EHW system it was noted that, in the full PDE simulations, the EHM limit ($\alpha = 10$), seemed to prefer non-local interactions over an inverse cascade as a method of producing zonal flows. Figures 6.9 and 6.10 show the progression in Fourier space of a system with $\alpha = 10$ and $\alpha = 0.5$ respectively. It can be seen that small α system develops modes which, in k-space, lie in close proximity, allowing local interactions and the production of zonal flows via cascades. Conversely, modes grown by the large α case are grouped into four regions that are separated in k-space so that non-local interactions are required to cause the zonal flow transition.

This can be characterised more rigorously using energy transfer functions (ETFs)[Camargo et al., 1995]; these describe the transfer of energy between mode numbers in Fourier space. ETFs are a general technique and can be applied to experimental data[Manz et al., 2009a,b]. The change in kinetic energy can be written as

$$\partial_t E^K(\vec{k}) = \sum_{\vec{k_1}} \mathscr{T}^K(\vec{k} \leftarrow \vec{k_1}) + \text{linear contribution}, \tag{6.20}$$

the change in potential energy as

$$\partial_t E^N(\vec{k}) = \sum_{\vec{k_1}} \mathscr{T}^N(\vec{k} \leftarrow \vec{k_1}) + \text{linear contribution} \tag{6.21}$$

and the change in enstrophy as

$$\partial_t \mathcal{W}(\vec{k}) = \sum_{\vec{k_1}} \mathscr{T}^{\mathcal{W}}(\vec{k} \leftarrow \vec{k_1}) + \text{linear contribution}. \tag{6.22}$$

The spectral energy transfer terms $\mathscr{T}$ are given by

$$\mathscr{T}^K(\vec{k} \leftarrow \vec{k_1}) = 2Re[(k_x k_{1y} - k_{1x} k_y)\varphi^\star_{\vec{k}} \omega_{\vec{k_2}} \varphi_{\vec{k_1}}], \tag{6.23}$$

$$\mathscr{T}^N(\vec{k} \leftarrow \vec{k_1}) = 2Re[(k_x k_{1y} - k_{1x} k_y)N^\star_{\vec{k}} \varphi_{\vec{k_2}} N_{\vec{k_1}}], \tag{6.24}$$

$$\mathscr{T}^{\mathcal{W}}(\vec{k} \leftarrow \vec{k_1}) = 2Re[(k_x k_{1y} - k_{1x} k_y)w^\star_{\vec{k}} \varphi_{\vec{k_2}} w_{\vec{k_1}}], \tag{6.25}$$

where $w_{\vec{k}} = \vec{k}^2 \varphi_{\vec{k}}$ is the vorticity and $\vec{k} = \vec{k_1} + \vec{k_2}$. To produce the ETF plots used later in this section the quantity $\mathscr{T}$ is calculated and averaged over a number of time slices. Normally ETFs are applied to fully developed turbulence where $\mathscr{T}$ will vary in time and space, they are therefore usually averaged over a large number of ensembles to ensure convergence. This is not possible here as we are

investigating the transient state of linear growth, therefore we use limited averaging over a discrete time window to produce our figures. This makes the amplitudes of the energy transfer functions less reliable, however, our focus is on the direction of the energy transfer and its locality. To remove any linear growth due to the primary instability the data is detrended before calculating the ETF. $\mathscr{T}(\vec{k} \leftarrow \vec{k_1})$ is a four dimensional quantity, therefore in order to display the results shown later it is averaged over absolute values of k.

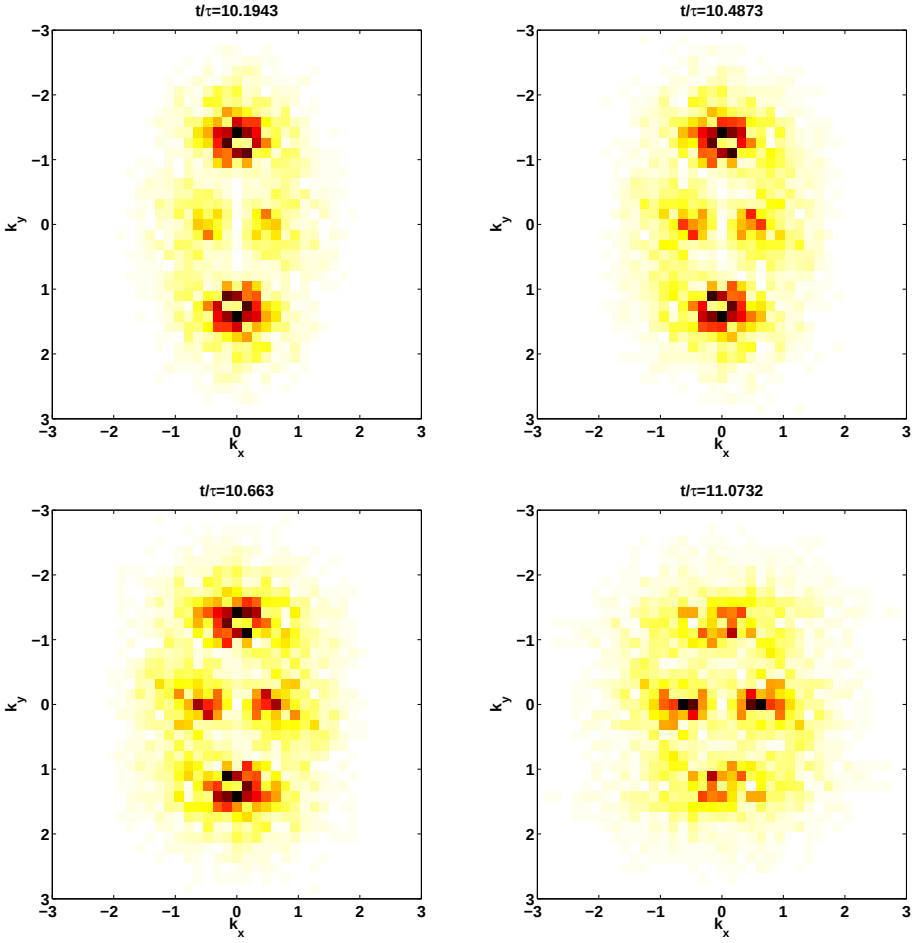

Figure 6.9: The transition from a drift-wave dominated system to a zonal-flow as seen in Fourier space for a case with $\alpha = 10$. It can be seen that the low k modes, which cause the zonal flow, remain separated from the high k modes which form the drift waves.

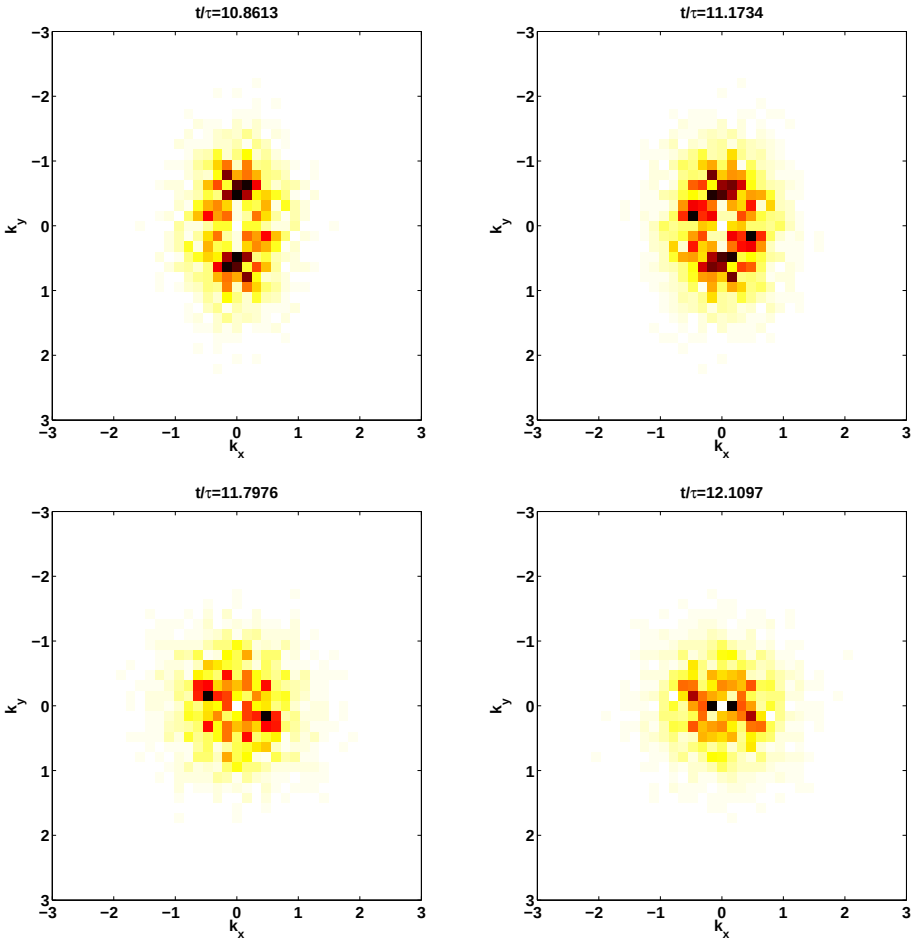

Figure 6.10: The transition from a drift wave dominated system to a zonal flow as seen in Fourier space for a case with $\alpha = 0.5$. It can be seen that there are a large number of modes with a moderate amplitude between the high k (drift wave) and low k (zonal flow) regions.

6.5.1 The EHM limit

Figure 6.11 shows the energy transfer functions averaged over 10 iterations during the linear growth phase of the $\alpha = 10$ system at $t/\tau \sim 7.6$. Points adjacent to the line $k = k_1$ indicate local interactions and therefore cascades. The potential energy transfer (E^N) in figure 6.11 forms a population transferring energy non-locally between $|k| \approx 1.41$ and $|k_1| \approx 0.47$, this same population is seen in the other panels in this figure but is masked by the cascading happening at higher modenumbers. In particular there are strong local cascades for the enstrophy ($\mathcal{W}$) as well as strong nonlocal interactions in the regions around $k = 3$ and $k_1 = 3$. The mode selected for exploring the MI ($k \sim 1.43, k_1 \sim 0.16$) is in fact on the edge of the population showing non-local interactions in the potential energy transfer plot. This suggests that although it is indeed transferring energy non-locally it is not the main driving force for the transition from drift waves to zonal flows. There are a number of other non-local interactions that cause energy to be transferred to the $|k| \approx \frac{2\pi}{L}$ scale, therefore causing zonal flows.

One of the strongest four-wave interactions at scales of interest indicated in this figure is between modes with $k \sim 1.41 \sim \frac{9\times 2\pi}{L}$ and $k \sim 0.47 \sim \frac{3\times 2\pi}{L}$. We therefore compared the analtytical models with the growth of the modes $\vec{p} = (0, \frac{-9\times 2\pi}{L}) = (0, -1.4137)$ and $\vec{q} = (\frac{3\times 2\pi}{L}, 0) = (0.47124, 0)$, shown in figure 6.12. It can be seen that the growth of the zonal mode deviates from linear growth less than the $\vec{q} = (\frac{2\pi}{L}, 0)$ case, figure 6.3, and unlike that case the ODEs now begin to oscillate around approximately the same saturation amplitude as the full simulation. This suggests that this non-local iteration may be more important for the zonal flow transition than the first case investigated.

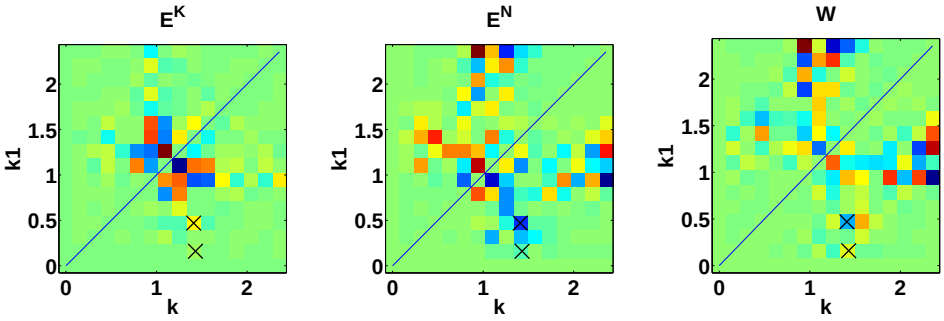

Figure 6.11: Energy transfer functions for $\alpha = 10$. Crosses mark modes that are referred to in the text.

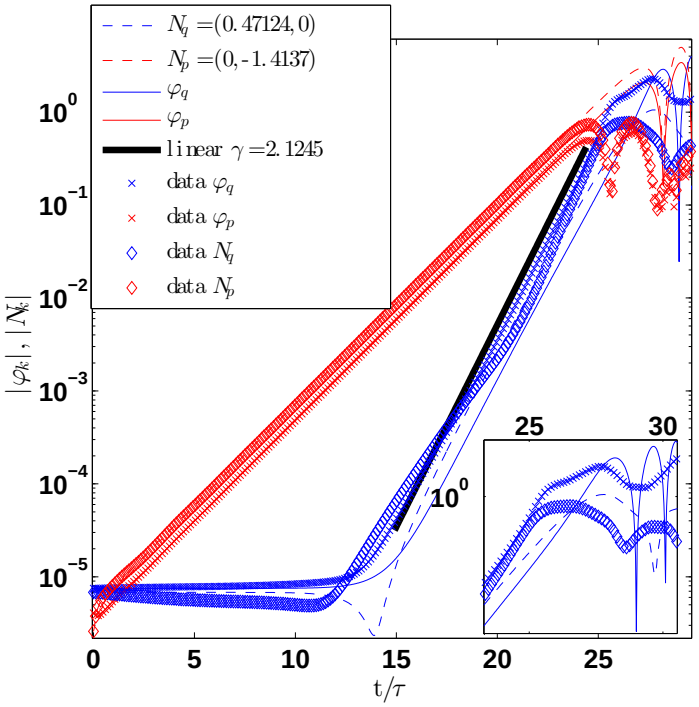

Figure 6.12: A comparison between the ODE predictions (lines) and the PDE simulation (markers) for a high $\alpha = 10$ case for modes $\vec{p} = (0, \frac{-9\times 2\pi}{L}) = (0, -1.4137)$ and $\vec{q} = (\frac{3\times 2\pi}{L}, 0) = (0.47124, 0)$. Density and potential were seeded independently with white noise. The line labelled linear grows at twice the primary growth rate of φ_p. The inset figure shows the saturation of potential, φ_q, in more detail.

6.5.2 The EHW regime

Again, figure 6.13 shows the energy transfer function averaged over 10 iterations during the linear growth phase at $t/\tau \sim 9.1$. It is immediately clear that, for small $|k|$, the majority of the energy transfer is either from cascades of nearby non-local interactions, for example $\Delta k = k_1 - k \sim \frac{2\times 2\pi}{L}$. Potential energy and vorticity show non-local interactions between modes with larger mode numbers, however these do not cause zonal flows. For comparison with the earlier ODE model we are specifically interested in transfer between $|k| \approx 0.471$ and $|k| \approx 0.157$. Although there is some contribution from neighbouring modes the transfer of energy to this mode is non-local.

Unlike the high alpha case there is no clear region of non-local interaction that stands out, however, the kinetic energy plot in figure 6.13 suggests that modes

$k \sim 0.63 \sim \frac{4\times 2\pi}{L}$ and $k =\sim 0.31 \sim \frac{2\times 2\pi}{L}$ are interacting strongly. Comparisons between ODE models and full simulations for modes $\vec{p} = (0, \frac{-4\times 2\pi}{L}) = (0, -0.62832)$ and $\vec{q} = (\frac{2\times 2\pi}{L}, 0) = (0.31416, 0)$ are therefore shown in figure 6.14. As with the previous case studied, figure 6.7, it takes approximately 15 linear growth times for the zonal waves to begin growing linearly, before which the density now oscillates in the real system. Once in the linear growth phase, the system grows at approximately twice the primary growth rate of φ_p, as expected. The ODEs now capture the saturation level better than for the $\vec{q} = (\frac{2\pi}{L}, 0)$ case, oscillating around the saturation level of the real system rather than just below it.

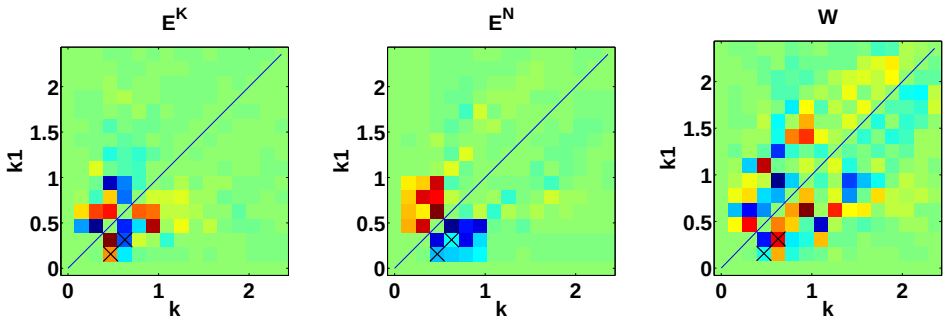

Figure 6.13: Energy transfer functions for $\alpha = 0.5$. Crosses mark modes that are referred to in the text.

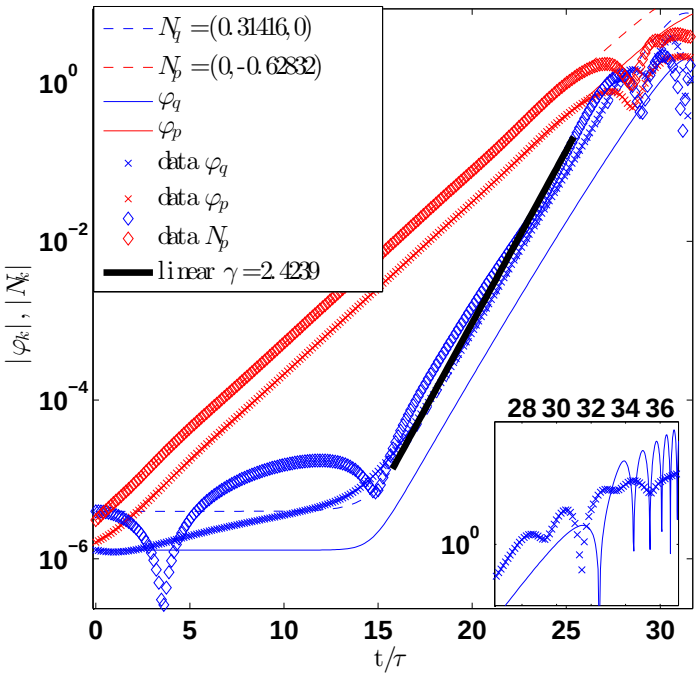

Figure 6.14: A comparison between the ODE predictions (lines) and the PDE simulation (markers) for a high $\alpha = 10$ case for modes $\vec{p} = (0, \frac{-4\times 2\pi}{L}) = (0, -0.62832)$ and $\vec{q} = (\frac{2\times 2\pi}{L}, 0) = (0.31416, 0)$. Density and potential were seeded independently with white noise. The line labelled linear grows at twice the primary growth rate of φ_p. The inset figure shows the saturation of potential, φ_q, in more detail.

6.6 Conclusions

The methods developed in chapter 5 were used to create analytical descriptions of the Extended-Hasegawa-Wakatani system. These took the form of a set of ODE equations and a linear prediction for the drift wave to zonal flow transition. These analytical techniques were used to investigate four-mode interactions in the presence of the EHW drift wave spectrum as well as their role in formation of zonal flows.

The primary instability in the EHW system means that the process used to derive a linear model in chapter 5 can not be applied in this chapter. Therefore physical arguments were made to suggest that the zonal modes should grow at approximately twice the rate of the pump waves. This proved to be an accurate approximation for the cases studied.

Four-mode truncations were particularly relevant for the high α, EHM limit, case. Energy transfer functions were used to show that in this setting, during the linear growth phase, local cascades did not cause a transfer of energy to large scales. Therefore, non-local couplings were responsible for the generation of zonal flows. This is not as clear for the low α case, but the ETFs do suggest that the transfer of energy to the lowest mode ($k = \frac{2\pi}{L}$) was via non-local couplings.

For both the high and low α cases, the ETFs suggested that the initial modes investigated were not the best modes for investigating four-wave interactions. New sets of modes were investigated based on the ETFs, these showed an even better agreement between the full system and the analytical models.

Chapter 7

Driving the Extended-Hasegawa-Mima System

7.1 Introduction

In chapter 6 we demonstrated how the growth rate of the zonal mode in the Extended-Hasegawa-Wakatani model could be adequately captured using four-wave truncated equations, although features such as the onset of the growth and saturation level were not correctly reproduced by such a simple approach. The two field EHW model, while more appealing due to its built in 'primary' instability mechanism, is difficult to treat analytically. The next natural step is to reproduce the effects of the EHW instability within the Extended-Hasegawa-Mima system. We do this using using a driving term whose features are similar to that of the Extended-Hasegawa-Wakatani primary instability, in a similar manner to the reproduction of the ion temperature gradient in [Quinn, 2011].

In this section each wave in the Extended-Hasegawa-Mimia system is driven at a rate determined by the linear dispersion relation of the EHW system, equation (3.80). Numerically this is easy to implement in Fourier space when each mode is individually accessible. Due to the normalisations used, the EHW primary dispersion relation depends entirely on the values of the adiabaticity parameter, α, defined by equation (3.57), and the density gradient parameter, κ, defined by equation (3.58). Using such an approach, the EHM system grows a spectrum of waves and, as in chapter 6, we select resonant sets of waves to compare to our analytical predictions. Despite the fact that we now have a spectrum of waves, we continue to use a four-

wave truncation as it is well known that adding additional sidebands does little to alter the accuracy of the predictions[Strintzi and Jenko, 2007].

At the beginning of the chapter the ODEs and linear dispersion relation derived in chapter 5 are extended to include the new driving term. Then, full numerical simulations, as described in chapter 4 but with an added driving term, are compared to the analytical models. Initially, modes are selected by inspecting Fourier space plots of the potential as it evolves. Two cases are considered, one where the equivalent Extended-Hasegawa-Wakatani system would be considered adiabatic and one where it would not. The chapter ends by using energy transfer functions (ETFs) to categorise local and non-local interactions in the two cases. The ETFs are used to select the most strongly interacting modes in the system and these are compared to the analytical models.

7.2 Adding forcing to the four-mode system

A linear forcing term can be added to the Fourier space representation of the EHM equation, (3.49), by writing it as

$$\partial_t \phi_{\vec{k}} + i\Omega_{\vec{k}}\phi_{\vec{k}} - \frac{1}{2}\sum_{\vec{k_1},\vec{k_2}} T(\vec{k},\vec{k_1},\vec{k_2})\phi_{\vec{k_1}}\phi_{\vec{k_2}}\delta_{\vec{k},\vec{k_1}+\vec{k_2}} = \nu_k \phi_{\vec{k}}. \tag{7.1}$$

In this chapter the length is normalised to ρ_s and time to ω_i so that the whole equation is unitless. The additional forcing term, $\nu_{\vec{k}}\phi_{\vec{k}}$, is artificially added to the end of the equation. It could be incorporated into the advection term, $i\Omega_{\vec{k}}\phi_{\vec{k}}$, but is left as a separate term to simplify the derivation of the ODEs. This separate forcing term does not effect the procedure used in the derivation, which was detailed in section 5.2. In fact, writing the forcing as a separate term means that the only difference between the ODEs for the forced and unforced systems is an extra term in each equation. In total this gives

$$\begin{aligned}
\partial_t \psi_{\vec{p}}(t) &= e^{it(\Delta_-)} T\left(\vec{p},\vec{p_-},\vec{q}\right)\psi_{\vec{q}}(t)\,\psi_{\vec{p_-}}(t) \\
&\quad + e^{it(\Delta_+)} T\left(\vec{p},-\vec{q},\vec{p_+}\right)\psi_{\vec{p_+}}(t)\,\overline{\psi_{\vec{q}}(t)} + \nu_{\vec{p}}\psi_{\vec{p}}(t) && (7.2)\\
\partial_t \psi_{\vec{q}}(t) &= e^{-it(\Delta_-)} T\left(\vec{q},-\vec{p_-},\vec{p}\right)\psi_{\vec{p}}(t)\,\overline{\psi_{\vec{p_-}}(t)} \\
&\quad + e^{it(\Delta_+)} T\left(\vec{q},-\vec{p},\vec{p_+}\right)\psi_{\vec{p_+}}(t)\,\overline{\psi_{\vec{p}}(t)} + \nu_{\vec{q}}\psi_{\vec{q}}(t) && (7.3)\\
\partial_t \psi_{\vec{p_-}}(t) &= e^{-it(\Delta_-)} T\left(\vec{p_-},-\vec{q},\vec{p}\right)\psi_{\vec{p}}(t)\,\overline{\psi_{\vec{q}}(t)} + \nu_{\vec{p_-}}\psi_{\vec{p_-}}(t) && (7.4)\\
\partial_t \psi_{\vec{p_+}}(t) &= e^{-it(\Delta_+)} T\left(\vec{p_+},\vec{q},\vec{p}\right)\psi_{\vec{p}}(t)\,\psi_{\vec{q}}(t) + \nu_{\vec{p_+}}\psi_{\vec{p_+}}(t) && (7.5)
\end{aligned}$$

where once again $\phi_{\vec{k}} = \psi_{\vec{k}}(t)e^{-i\Omega_{\vec{k}}t}$ and $\overline{\phi_{\vec{k}}} = \overline{\psi_{\vec{k}}}(t)e^{i\Omega_{\vec{k}}t}$ is a conjugate of $\phi_{\vec{k}}$. It should be noted here that the forced linear growth is incorporated into $\psi_{\vec{k}}(t)$; an equally valid solution for substitution into the truncated version of equation (7.1) would be $\phi_{\vec{k}} = \psi_{\vec{k}}(t)e^{-i(\Omega_{\vec{k}}+i\nu_{\vec{k}})t}$, where the linear growth has been written explicitly. In this case a set of ODEs would be produced that did not have the extra forcing term, but had a modified resonance condition, as defined by $\Delta_{\pm}$, instead.

The coupling parameter T, now unitless, is given by

$$T(\vec{k},\vec{k_1},\vec{k_2}) = -\frac{(k_{1_y}k_{2_x} - k_{1_x}k_{2_y})(k_2^2 - k_1^2 + \delta_{s,1}(\delta_{k_{1_y},0} - \delta_{k_{2_y},0}))}{(1 + k^2 - \delta_{k_y,0}\delta_{s,1})}, \tag{7.6}$$

$$\Delta_- = \Omega_{\vec{p}} - \Omega_{\vec{q}} - \Omega_{\vec{p}_-}, \tag{7.7}$$

$$\Delta_+ = \Omega_{\vec{p}} + \Omega_{\vec{q}} - \Omega_{\vec{p}_+} \tag{7.8}$$

and $\Omega_{\vec{k}}$ is

$$\Omega_{\vec{k}} = -\frac{v_\star k_y}{1 + k^2}. \tag{7.9}$$

where $v_\star$ is now a unitless parameter defining the density gradient of the system. Although the derivation here is valid for any linear function where $\nu_{\vec{k}} = \nu(\vec{k})$, in this work the form

$$\nu_{\vec{k}} = a(\vec{k}) - bk^4 \tag{7.10}$$

was used. The second term, $bk^4\phi_k$ is the Fourier space representation of a real space hyperviscosity term $b\nabla^2(\nabla^2\phi)$, b is a hyperviscosity coefficient. The hyperviscosity is added to model the dissipation that would occur at high mode numbers in a real system but is not included in the Hasegawa-Mima equation.

Quantity $a(\vec{k})$ is a general representation of a term that drives the system. In this work $a(\vec{k})$ will become $a(\vec{k},\alpha,\kappa)$ and will drive the EHM system in such a way as to reproduce the effect of the extended-Hasegawa-Wakatani primary instability described in section 3.2.4. A more complete description specific to this chapter is given in section 7.4.

7.3 The linearised growth rate

Unlike section 5.3, the growth caused by the additional forcing term in equation (7.1) means that it is not possible to derive a linear dispersion relation for the zonal flow transition investigated in this chapter. The forcing term means that a time independent eigenvalue problem cannot be formed. Nevertheless, some linearisation

can still be performed, and a prediction for the growth rate made in the style of section 6.3.

As in chapter 5 we linearise the ODEs, (7.2) to (7.5), using

$$\vec{\psi} = \begin{pmatrix} \psi_{\vec{p}} \\ \psi_{\vec{q}} \\ \psi_{\vec{p_+}} \\ \psi_{\vec{p_-}} \end{pmatrix} = \begin{pmatrix} \psi_p \\ 0 \\ 0 \\ 0 \end{pmatrix} + \varepsilon \begin{pmatrix} 0 \\ \psi_{\vec{q}} \\ \psi_{\vec{p_+}} \\ \psi_{\vec{p_-}} \end{pmatrix}, \tag{7.11}$$

where ε is a small parameter. Firstly, for the pump mode $\vec{p}$, this gives us

$$\frac{d}{dt}\psi_p = \varepsilon^2 e^{it(\Delta_-)} T(p, p_-, q)\psi_q \psi_{p_-} + \varepsilon^2 e^{it(\Delta_+)} T(p, -q, p_+)\psi_{p_+}\overline{\psi_q} + v_p\psi_p \tag{7.12}$$

and keeping only terms $O(1)$ this becomes

$$\frac{d}{dt}\psi_p = \nu_p\psi_p. \tag{7.13}$$

This is no longer constant in time and has a solution

$$\psi_p = \psi_0 e^{\nu_p t}.$$

For consistency with chapter 6, where we used G to represent the total linear growth rate of the driving wave, we will write

$$\psi_p = \psi_0 e^{Gt}. \tag{7.14}$$

Repeating the process for each of the remaining equations in turn, this time keeping $O(\varepsilon)$ terms, leaves us with

$$\frac{d}{dt}\psi_q = e^{-it(\Delta_-)} T(q, -p_-, p)\psi_p\overline{\psi_{p_-}} + e^{it(\Delta_+)} T(q, -p, p_+)\psi_{p_+}\overline{\psi_p} + \nu_q\psi_q, \tag{7.15}$$

$$\frac{d}{dt}\psi_{p_-} = e^{-it(\Delta_-)} T(p_-, -q, p)\psi_p\overline{\psi_q} + \nu_{p_-}\psi_{p_-}, \tag{7.16}$$

$$\frac{d}{dt}\psi_{p_+} = e^{-it(\Delta_+)} T(p_+, q, p)\psi_p\psi_q + \nu_{p_+}\psi_{p_+}. \tag{7.17}$$

We now consider the smooth and slowly varying form of the EHW linear dispersion relation, for example see figure 7.1, as this will be used to calculate the driving used on each mode. We restrict ourselves to cases where $p \gg q$ so that $\vec{p_\pm} = \vec{p} \pm \vec{q} \sim \vec{p}$ and therefore $\nu_{p_\pm} \sim \nu_p = G$. We use this as justification to seek

solutions of the form

$$\psi_{p_+}(t) = A_{p_+} e^{-i\omega_{p_+} t} e^{Gt}, \tag{7.18}$$

$$\psi_{p_-}(t) = A_{p_-} e^{-i\omega_{p_-} t} e^{Gt}, \tag{7.19}$$

where $\omega_{p_\pm}$ and G are real. We also know that the zonal mode is not being driven, hence, imposing $\nu_q = 0$. Using equations (7.18) and (7.19), and considering the resonant case where $\Delta_\pm = 0$, we can rewrite equation (7.15) as

$$\frac{d}{dt}\psi_q = \left\{ T(q, -p_-, p)\psi_0 \overline{A_{p_-}} e^{i\omega_{p_-} t} + T(q, -p, p_+) A_{p_+} \overline{\psi_0} e^{-i\omega_{p_+} t} \right\} e^{2Gt}. \tag{7.20}$$

The time dependant parts inside the braces are oscillatory, therefore φ_q must grow linearly at a rate

$$\gamma = 2G, \tag{7.21}$$

as with chapter 6 this is unitless as time is normalised to ω_i.

As with the Extended-Hasegawa-Wakatani case (chapter 6) we define an associated linear growth time

$$\tau = \frac{1}{\gamma}.$$

When plotting numerical results, γ is the gradient of the lines labelled 'linear'.

7.4 Numerical Results

As we wish to recreate the effect of the Hasegawa-Wakatani primary instability we will drive the Extended-Hasegawa-Mima system, in Fourier space, using a profile dictated by the EHW dispersion relation, equation (3.80). To do this we solve equation (3.80) for a given value of adiabaticity parameter α and density gradient κ, and use the imaginary part of the solution as the $a(\vec{k})$ part of the forcing term given in equation (7.10). As κ is the EHW equivalent of $v_\star$ we will use $\kappa = v_\star = 10$ throughout this chapter, due to the normalisations used they are both dimensionless parameters related to the density gradient in the system.

Here we consider two regimes for driving the Extended-Hasegawa-Mima system. The first is the the limit where the adiabaticity parameter $\alpha \gg 1$. In the nomenclature of the Hasegawa-Wakatani system this is known as the Hasegawa-Mima limit as it represents the recovery of an adiabatic electron response, described in section 3.2.4. Here we use the term 'high-α' to refer to the case where $\alpha = 10$; the driving profile used for this limit is shown in figure 7.1(a).

The other limit, $\alpha \ll 1$, is known as the Euler limit and is not explored here. Instead we look at the regime where $\alpha \sim 1$ and the Extended-Hasegawa-Wakani system would have a non-adiabatic parallel plasma response. We call this the 'low-α' case and use a value of $\alpha = 0.5$. The relevant profile for driving the EHM system is shown in 7.1(b).

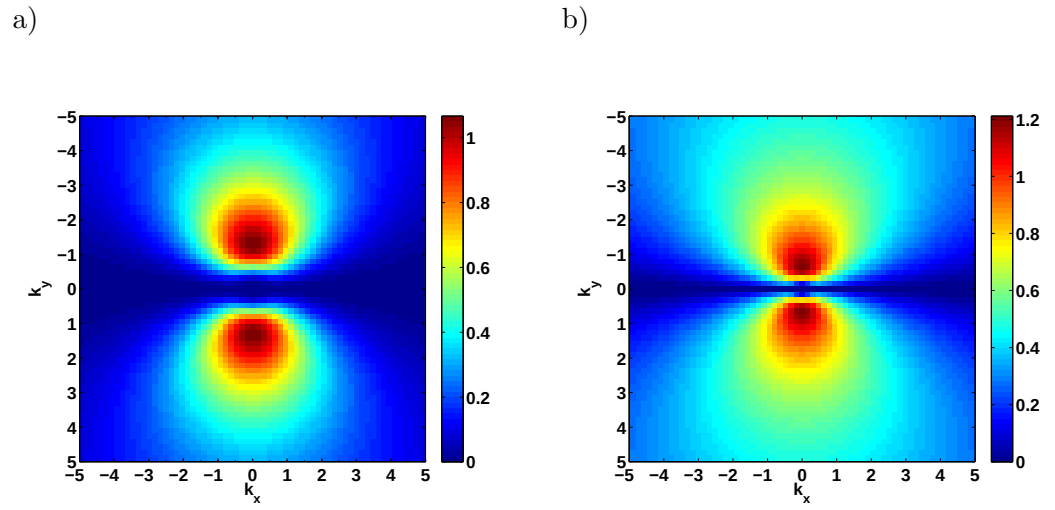

Figure 7.1: A subset of the profiles used to drive the EHM system. In both cases the mode numbers have been normalised to the box size, which was identical for both simulations. It can be seen that the EHM limit case (a), with $\alpha = 10$, is centred around higher mode numbers than the EHW case (b), with $\alpha = 0.5$. In both cases $\kappa = 10$, and beyond the region shown the driving rapidly decays.

7.4.1 The high-α limit

The first case studied was the high-α case, the EHM system was driven in such a way as to reproduce the drift waves grown by the primary instability in the Extended-Hasegawa-Wakatani system when $\alpha = 10$ and $\kappa = 10$. In this case the driving profile is centred around $|k| \approx \frac{10\times 2\pi}{L} \approx 1.57$. Figure 7.1(a) shows that it tends to 0 before reaching the $k_y = 0$ axis.

As with chapter 6 the values of $\vec{p}$ and $\vec{q}$ to be used in the ODE system and analytical growth rate predictions were chosen by looking at the Fourier space evolution of the system. The evolution of potential in real space is shown in figure 7.2 and the Fourier transform used to chose modes is shown figure 7.3. In this case $\vec{p} = (0, -\frac{9\times 2\pi}{L}) = (0, -1.41)$ and $\vec{q} = (\frac{2\pi}{L}, 0) = (0.157, 0)$ were chosen, again because

satellite modes were clearly visible. The pump mode, $\vec{p}$, is close to the most strongly driven mode, which is at $\vec{k}_{max} = (0, \pm\frac{2\pi}{L} \times 8)$. The results are shown in figure 7.4, it can clearly be seen that the ODEs correctly capture the linear growth rate of the driving mode $\vec{p}$, however there is some initial growth of the perturbing mode, between $t = 0$ and $t = 4\tau$, that is not captured by the linear driving. If this extra growth is measured at early times and applied as a linear driving term the ODEs capture the initial stage of the evolution better, but with or without it they deviate after ~ 4 linear growth times and after short adjustment grow at approximately the linear growth rate. In both cases the growth rate of mode $\vec{p}$ has been measured from the full PDE simulation and its value has been assigned to G when solving the ODE equations, (7.2) to (7.5), as well as when solving equation (7.21) to obtain the linear growth rate. The measured growth rate is roughly equal to the linear growth rate of the primary instability described by (3.80). The measured value is $\nu_p^{\text{measured}} = 1.066$ whereas the analytical prediction from equation (3.80) is $\nu_p^{\text{analytical}} = 1.062$. This indicates that there is very little damping on this mode, and its interactions with other modes are negligible. A line growing linearly with a growth rate $\gamma = 2G$, labelled 'linear', is also shown in figure 7.4. This shows reasonable agreement with the truncated ODE model, indicating that the approximation $\nu_\pm \approx \nu_p = G$ is reasonable.

It can also be seen in figure 7.4 that after a short period of linear growth, at around $\frac{t}{\tau} \sim 10$, the amplitude of $\vec{q}$ in the real system begins to oscillate before returning to growing linearly. This is discussed further in section 7.5.

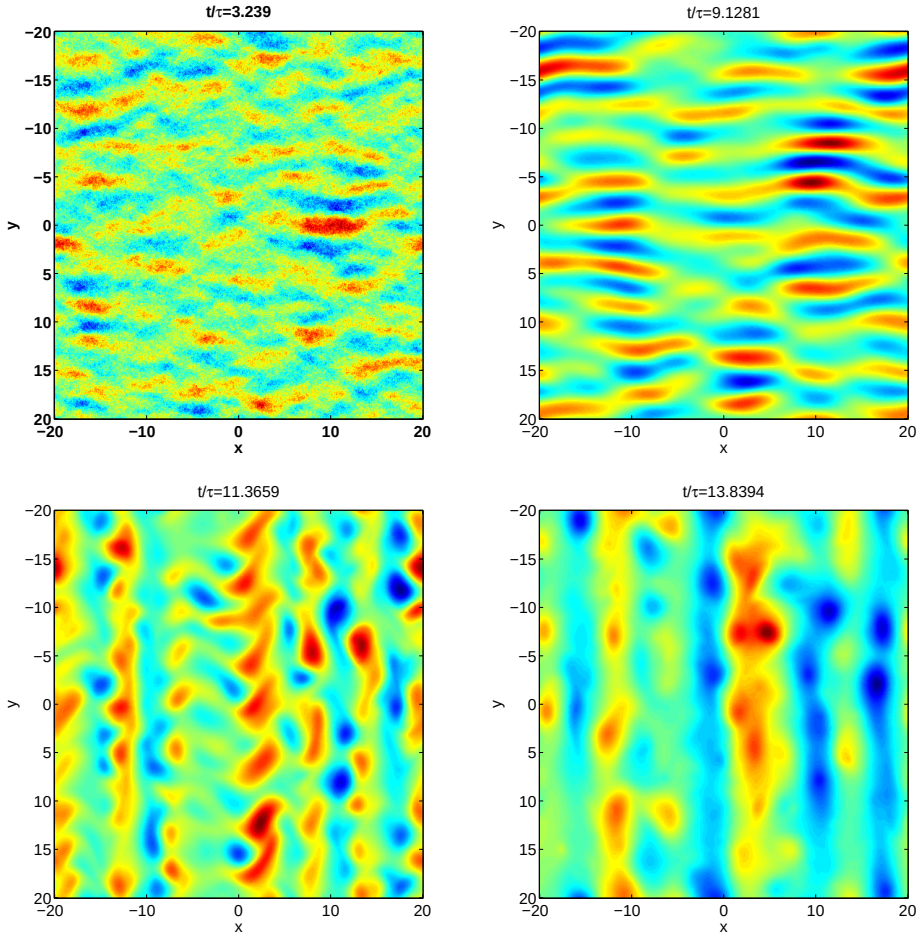

Figure 7.2: Real space images of potential in a driven system where the driving profile was generated using $\alpha = 10$ and $\kappa = 10$. It can be seen that the drift wave spectrum supersedes the high frequency components of the initial condition, before transitioning to a zonal structure. The times shown correspond to figure 7.4.

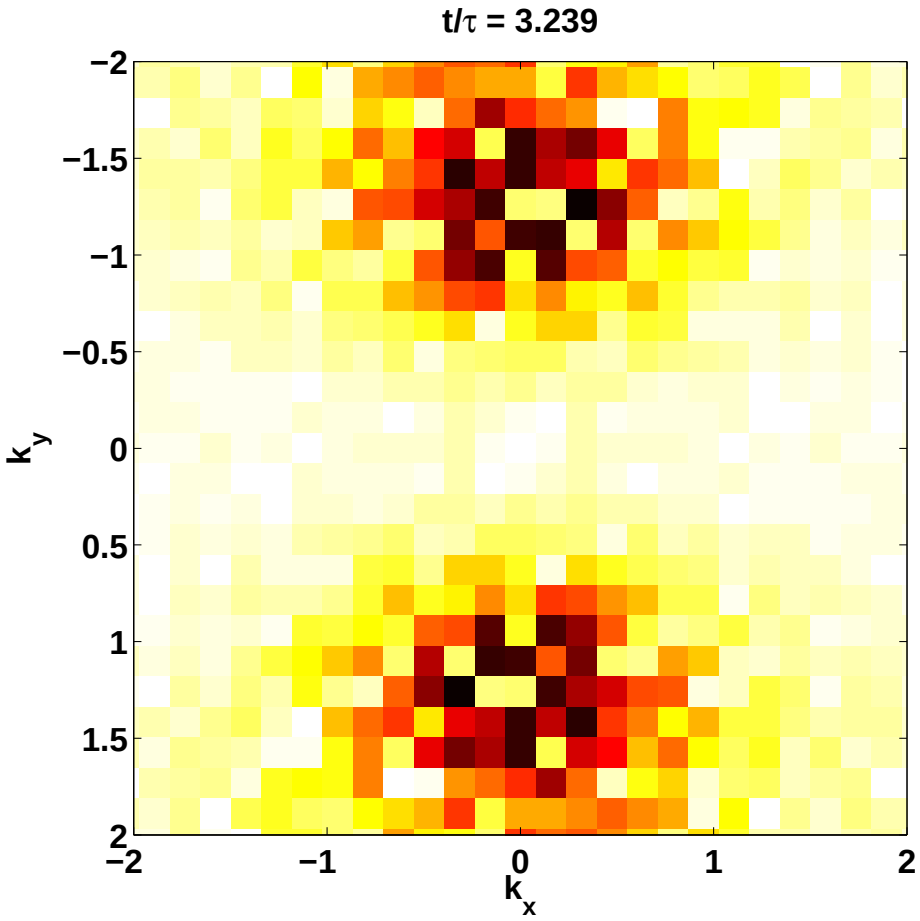

Figure 7.3: A Fourier transform of the potential presented in the first panel of figure 7.2. The modes $\vec{p} = (0, -\frac{9\times 2\pi}{L}) = (0, -1.41)$ and $\vec{p_{\pm}} = (\pm\frac{2\pi}{L}, -\frac{9\times 2\pi}{L}) = (\pm 0.157, -1.41)$ are clearly present and can form a coupled set of modes for use in the analytical models.

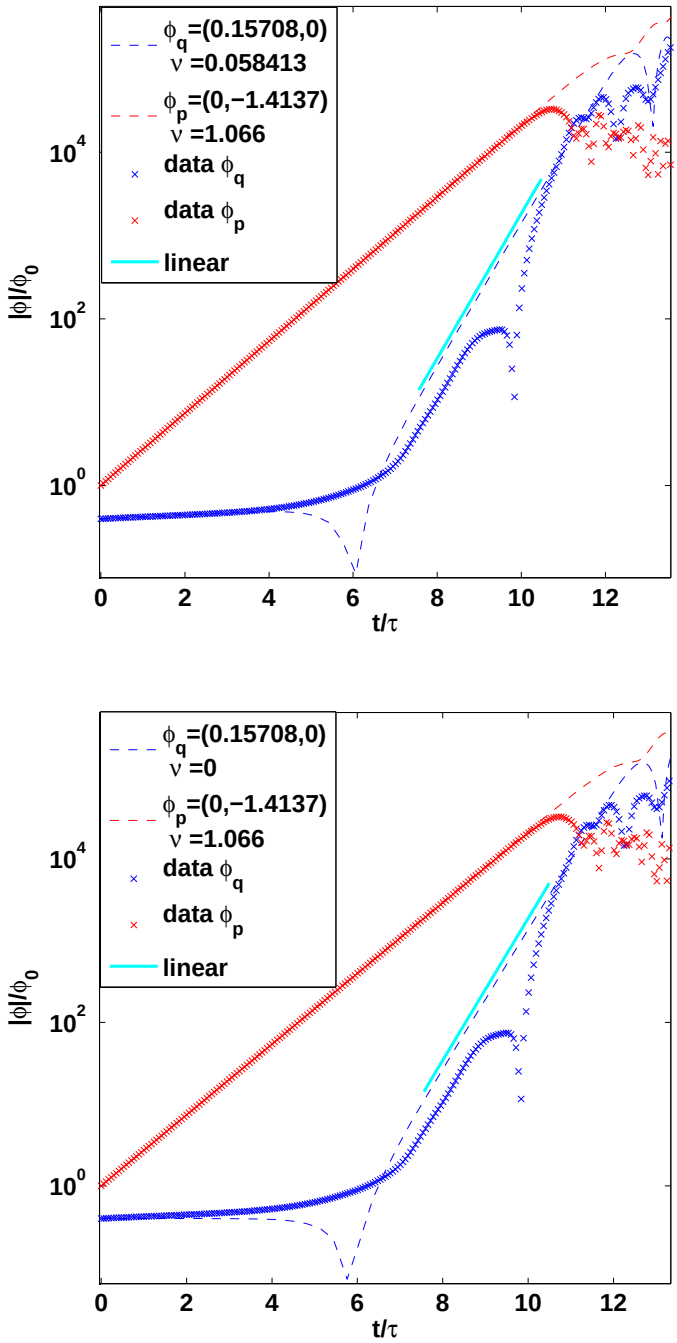

Figure 7.4: Comparing the ODE and linear predictions to the PDE simulation in the $\alpha = 10$ case. Markers indicate output from the full simulation, dashed lines predictions from the ODEs, and the line labelled linear is arbitrarily positioned but grows at the linear growth rate. The forcing (ν) used for each mode is shown in the legend. Without artificially forcing ϕ_q (bottom), the ODE does not capture the growth between $t = 0$ and $t = 4\tau$. In both cases the linear growth rate of ϕ_q is $\gamma = 2.1$.

7.4.2 The low-α case

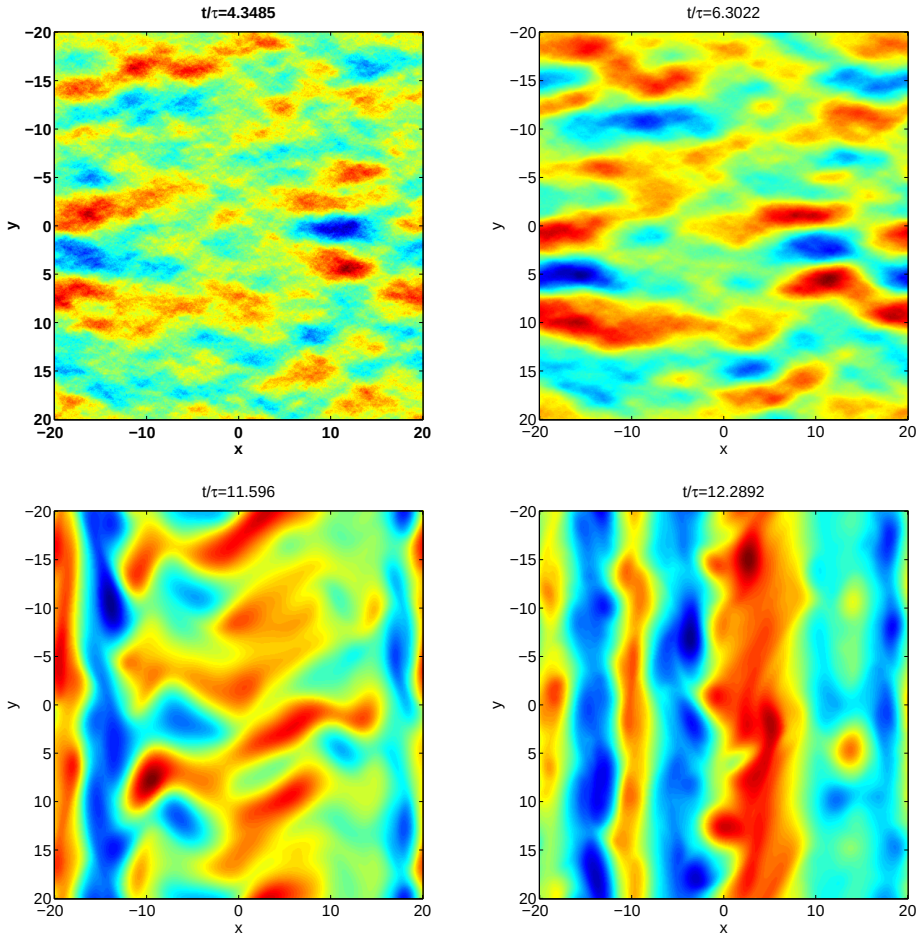

Figure 7.5: Real space images of potential in a driven system where the driving was generated using $\alpha = 0.5$ and $\kappa = 10$. It can be seen that the drift wave spectrum supersedes the high frequency components of the initial condition, before transitioning to a zonal structure. The times shown correspond to figure 7.7(a).

In this case the EHM system was driven so as to reproduce the drift waves that would be grown by the primary instability in an extended-Hasegawa-Wakatani system when $\alpha = 0.5$ and $\kappa = 10$. We will refer to this situation as the low-α case. The resulting driving profile, shown in figure 7.1, shows that modes are now driven far closer to the $k_y = 0$ line than in the $\alpha = 10$ case. This difference can be seen by comparing the Fourier space images from the full simulation in figures 7.6 and 7.3. Along with the results of chapter 6, this leads us to expect more interactions that are local in wave number space. These local interactions could provide a secondary

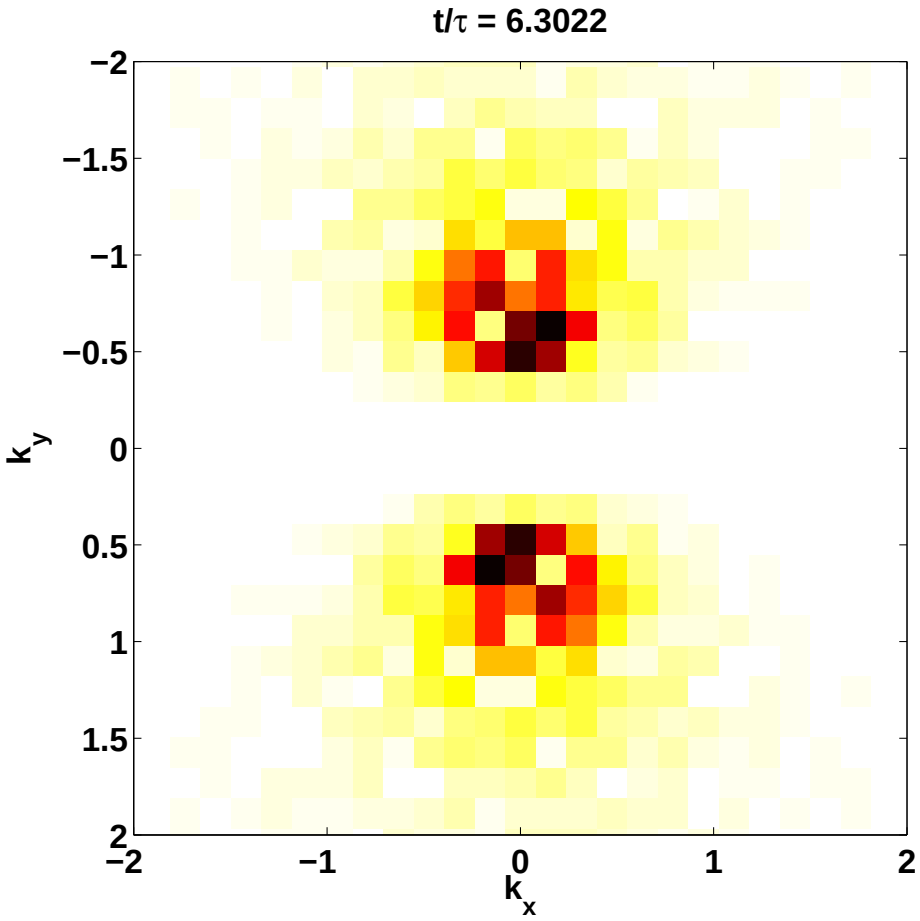

Figure 7.6: A Fourier transform of the potential presented in the second panel of figure 7.5. The modes $\vec{p} = (0, -3 \times \frac{2\pi}{L}) = (0, -0.471)$ and $\vec{p_{\pm}} = (\pm\frac{2\pi}{L}, -3 \times \frac{2\pi}{L}) = (\pm 0.157, -0.471)$ are clearly present and form a coupled set of modes for use in the analytical models.

mechanism for the production of zonal flows, by gradually transferring energy to large scales. The real space images in figure 7.5 show broader drift waves, which is a direct result of the driving profile used in in this case, which drives modes at lower $\vec{k}$. We now investigate the modes $\vec{p} = (0, -3 \times \frac{2\pi}{L}) = (0, -0.471)$ and $\vec{q} = (\frac{2\pi}{L}, 0) = (0.157, 0)$, shown in figure 7.6. The evolution of potential in real space is shown in figure 7.5. The chosen pump mode, $\vec{p}$, is again close to the most strongly driven mode, which is at $\vec{k}_{max} = (0, \pm\frac{2\pi}{L} \times 4)$. Once again the growth of the driving mode $\vec{p}$ was measured from the full PDE system and used as G in the ODEs and linear prediction, the measured value is $\nu_p^{\text{measured}} = 1.1408$. This is again almost identical to the value used to drive the system, $\nu_p^{\text{analytical}} = 1.1412$, obtained from the linear growth rate of the Extended-Hasegawa-Wakatani primary instability, equation (3.80).

An immediate difference from the previous section, 7.4.1, is that when initialising the ODEs at t=0 they produce inaccurate predictions, as shown in figure 7.7(a). In order to get reasonable predictions from the ODEs it is necessary to initialise them with conditions taken from the real simulation once it has already entered the linear growth phase. This is shown in figure 7.7(b) where it can be seen that the ODEs do produce a reasonable prediction for the growth rate of the system, but the linear approximation does not. For the real system, this suggests that other modes are contributing to the growth of ϕ_q. Again, this is discussed further in section 7.5 where energy transfer functions are used to attempt to separate the cascades from the non-local interactions.

a)

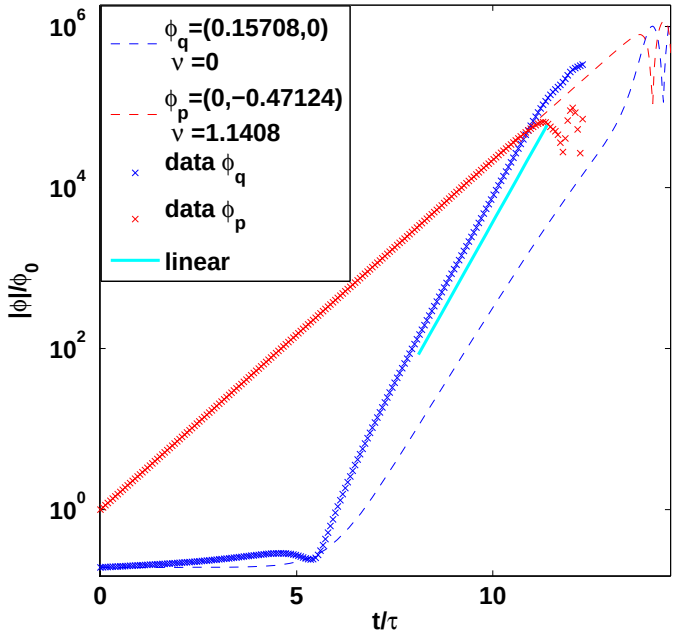

b)

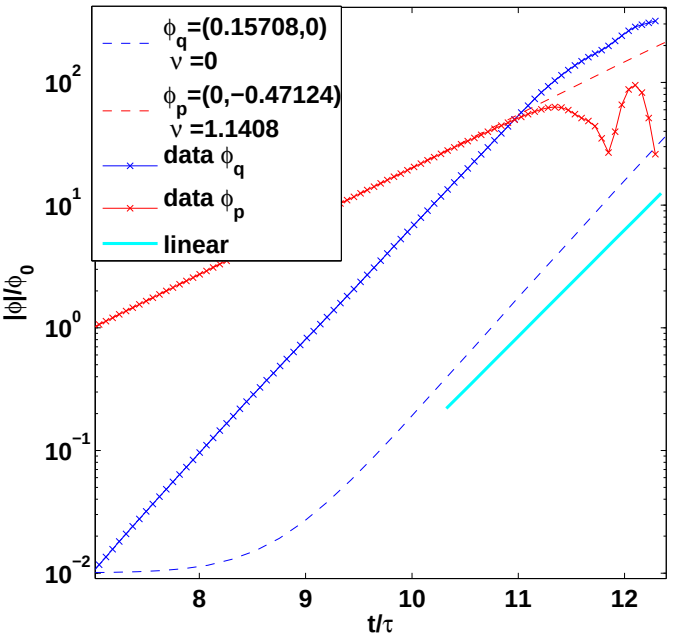

Figure 7.7: Comparing the ODE and linear predictions to the PDE simulation in the $\alpha = 0.5$ case. Markers indicate output from the full simulation, dashed lines predictions from the ODEs, and the line labelled linear is arbitrarily positioned but grows at the linear growth rate. The forcing (ν) used for each mode is shown in the legend. The linear growth rate is $\gamma = 2.28$ Unlike the high α case the ODEs must be solved after the system has started growing linearly, shown in panel (b).

7.5 Energy transfer functions

As in section 6.5, we now use energy transfer functions to distinguish between cascades and non-local interactions. The energy transfer functions for the EHM equation can be easily derived from equation (3.49), which is firstly rewritten as

$$\partial_t(1-\delta_{k_y,0}\delta_{s,1}+k^2)\phi_{\vec{k}}+i(1-\delta_{k_y,0}\delta_{s,1}+k^2)\Omega_{\vec{k}}\phi_{\vec{k}} \\ -(1-\delta_{k_y,0}\delta_{s,1}+k^2)\frac{1}{2}\sum_{\vec{k_1},\vec{k_2}}T(\vec{k},\vec{k_1},\vec{k_2})\phi_{\vec{k_1}}\phi_{\vec{k_2}}\delta_{\vec{k},\vec{k_1}+\vec{k_2}}=0 \tag{7.22}$$

in order to separate the potential and kinetic energy parts. Then the whole equation is multiplied by the conjugate of $\phi_{\vec{k}}$ which we denote as $\phi^{\star}_{\vec{k}}$ to give

$$\partial_t(1-\delta_{k_y,0}\delta_{s,1}+k^2)|\phi_{\vec{k}}|^2+i(1-\delta_{k_y,0}\delta_{s,1}+k^2)\Omega_{\vec{k}}|\phi_{\vec{k}}|^2 \\ -(1-\delta_{k_y,0}\delta_{s,1}+k^2)\frac{1}{2}\sum_{\vec{k_1},\vec{k_2}}T(\vec{k},\vec{k_1},\vec{k_2})\phi_{\vec{k_1}}\phi_{\vec{k_2}}\phi^{\star}_{\vec{k}}\delta_{\vec{k},\vec{k_1}+\vec{k_2}}=0. \tag{7.23}$$

(7.24)

The spectral energy transfer terms are then obtained by splitting the nonlinear term into kinetic ($\mathscr{T}^K$) and potential ($\mathscr{T}^N$) contributions and writing $\vec{k_2}=\vec{k}-\vec{k_1}$ to give

$$\mathscr{T}^K(\vec{k}\leftarrow\vec{k_1})=\frac{1}{2}\sum_{\vec{k_1},\vec{k}-\vec{k_1}}k^2T(\vec{k},\vec{k_1},\vec{k}-\vec{k_1})\phi_{\vec{k_1}}\phi_{\vec{k}-\vec{k_1}}\phi^{\star}_{\vec{k}} \tag{7.25}$$

and

$$\mathscr{T}^N(\vec{k}\leftarrow\vec{k_1})=\frac{1}{2}\sum_{\vec{k_1},\vec{k}-\vec{k_1}}(1-\delta_{k_y,0}\delta_{s,1})T(\vec{k},\vec{k_1},\vec{k}-\vec{k_1})\phi_{\vec{k_1}}\phi_{\vec{k}-\vec{k_1}}\phi^{\star}_{\vec{k}} \tag{7.26}$$

Finally the energy transfer functions are obtained by summing over all $\vec{k_1}$, hence

$$\partial_t E^K(\vec{k})=\sum_{\vec{k_1}}\mathscr{T}^K(\vec{k}\leftarrow\vec{k_1})+\text{linear contribution} \tag{7.27}$$

and

$$\partial_t E^N(\vec{k})=\sum_{\vec{k_1}}\mathscr{T}^N(\vec{k}\leftarrow\vec{k_1})+\text{linear contribution} \tag{7.28}$$

7.5.1 The high-α limit

Figure 7.8 shows energy transfer functions for an $\alpha = 10$ case averaged over a time window where the perturbing mode $\vec{q} = (0, 0.157)$ was growing. There are clusters of interacting modes away from the line $k = k_1$ clearly showing a dominance of non-local interactions. However, the interaction corresponding to a transfer of energy between $\vec{p} = (0, -1.41)$ and $\vec{q} = (0, 0.157)$ is on the edge of the visible interactions and has a considerably lower amplitude than other nearby modes. What's more, it directly neighbours modes with energy flowing in the opposite direction. Keeping in mind that these ETF plots involve binning data and averaging over time this may explain the dip seen in figure 7.4. If during the linear growth phase energy cascades to the neighbouring mode, which the ETF indicates is happening for mode numbers $k \gtrsim 1$, it could then be transferred in the wrong direction.

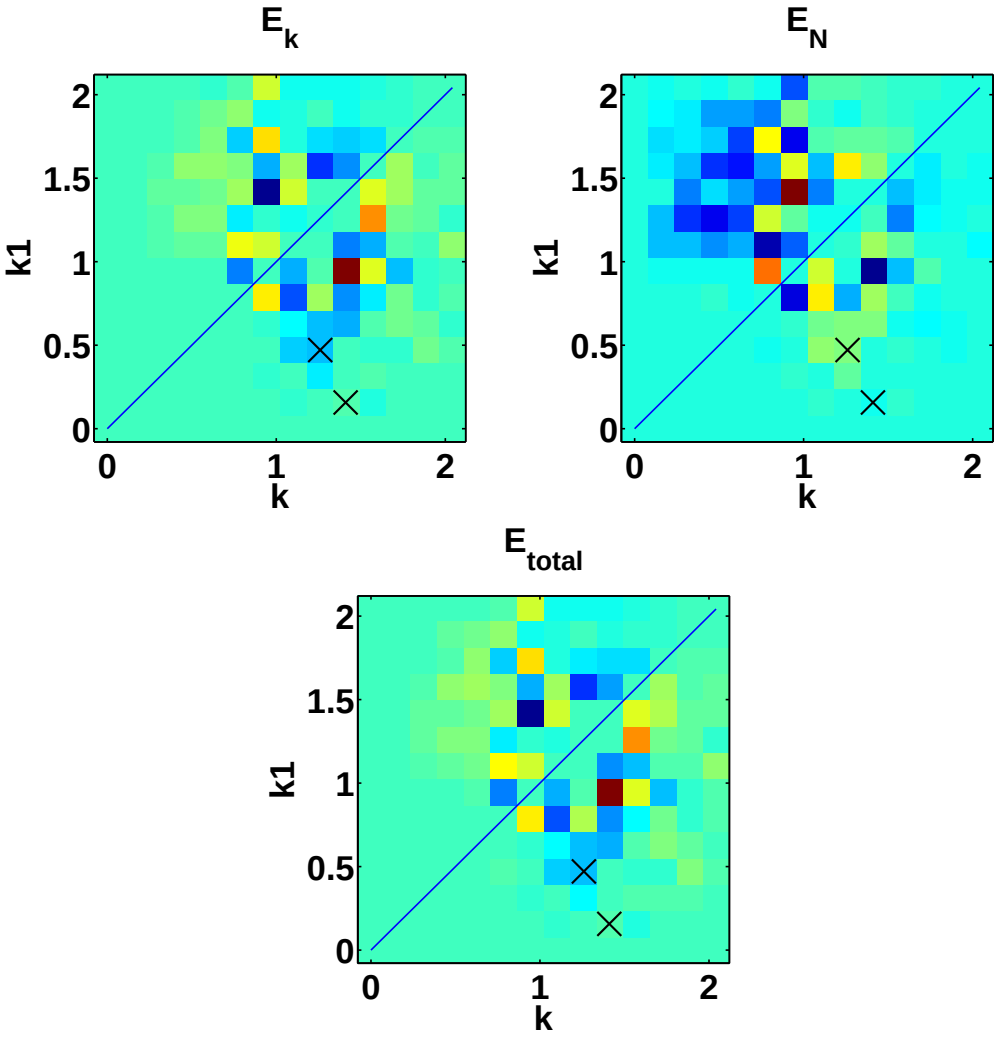

Figure 7.8: Energy transfer functions for the $\alpha = 10$ case. They have been produced by averaging over the section that grows at the linear growth rate, $t/\tau \sim 7$ to $t/\tau \sim 9$. Crosses mark modes that are referred to in the text.

The ETF plots do however suggest that there is a strong non-local coupling is between modes $\vec{p} = (0, -1.26) = (0, \frac{-8\times 2\pi}{L})$ and $\vec{q} = (0.471, 0) = (\frac{3\times 2\pi}{L}, 0)$. The evolution of their amplitudes is plotted in figure 7.9. It can be seen that although the real system does not grow entirely linearly it does grow at roughly the linear growth rate. In this case both the ODEs and the linear prediction from solving (7.21) give the correct growth rate, the ODEs even predict the amplitude at which the system departs from the linear growth phase.

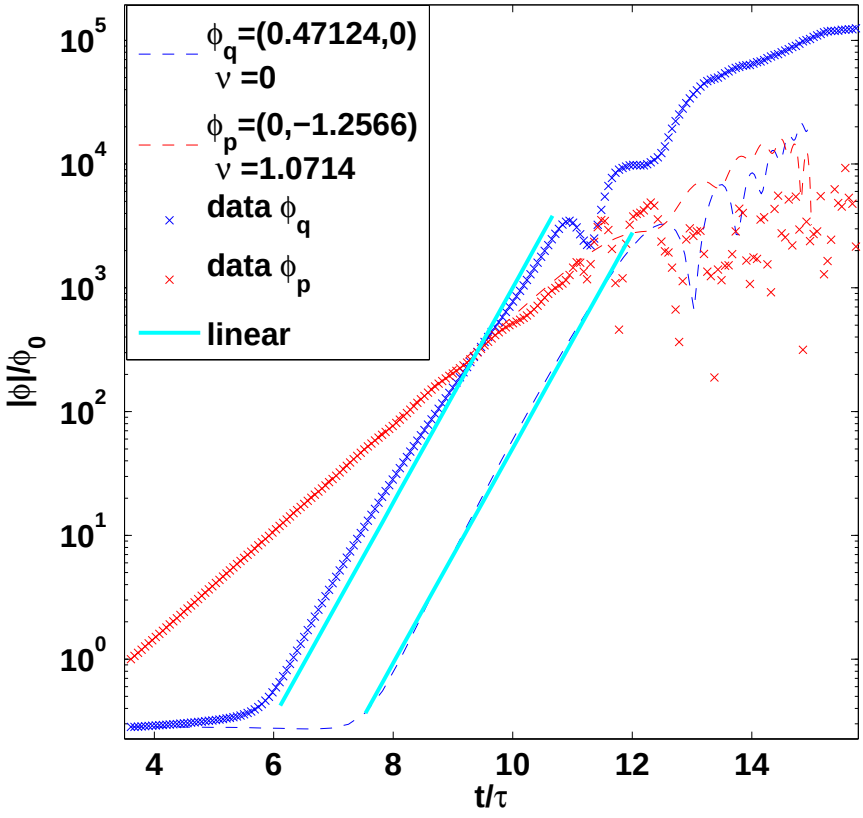

Figure 7.9: Comparing the ODE and linear predictions to the PDE simulation in the $\alpha = 10$ case for modes $\vec{p} = (0, -1.26) = (0, \frac{-8\times 2\pi}{L})$ and $\vec{q} = (0.471, 0) = (\frac{3\times 2\pi}{L}, 0)$ as indicated by the ETF plot . Markers indicate output from the full simulation, dashed lines predictions from the ODEs, and the lines labelled linear are arbitrarily positioned but grow at the linear growth rate. The forcing (ν) used for each mode is shown in the legend. The ODEs use initial values taken at time $\frac{t}{\tau} \sim 3.5$, after the system has made some initial adjustments. Unlike the case in figure 7.4, the full simulation does not strongly deviate from linear growth.

7.5.2 The low-α case

We now turn to the case $\alpha = 0.5$. In contrast with the previous case figure 7.10 indicates that there are a number of local interactions at low modenumbers, there are strongly interacting modes close to the $k = k_1$ line. This suggests that we are indeed in a regime where cascades are important. Once again the modes investigated earlier (in section 7.4.2), $\vec{p} = (0, -0.471)$ and $\vec{q} = (0.157, 0)$, are on the edge of the nonlocal interaction region. Unlike the high-α case there is a clear region around $k \sim 0.5$ where energy is being transferred from k to k_1, however there are a number of modes transferring energy to $k_1 \sim 0.1$, this would explain why the system grows faster than the linear prediction in figure 7.7 but not why the ODE prediction is more accurate.

Once again there is a suggestion that a different set of modes are coupling more strongly than the set we initially investigated, in this case $\vec{p} = (0, -0.785) = (0, \frac{-5\times 2\pi}{L})$ and $\vec{q} = (0.157, 0) = (\frac{2\pi}{L}, 0)$. However, the randomly generated initial conditions for this set of modes did not have $\phi_p(t = 0) \gg \phi_q(t = 0)$, therefore the system was left for some time before the ODEs were initialised. The results are shown in figure 7.11. Again the linear approximation and ODEs give a better prediction than in the previous case investigated. In this case neither the PDE nor ODE predictions show a completely linear growth even though it still seems to be the dominant effect.

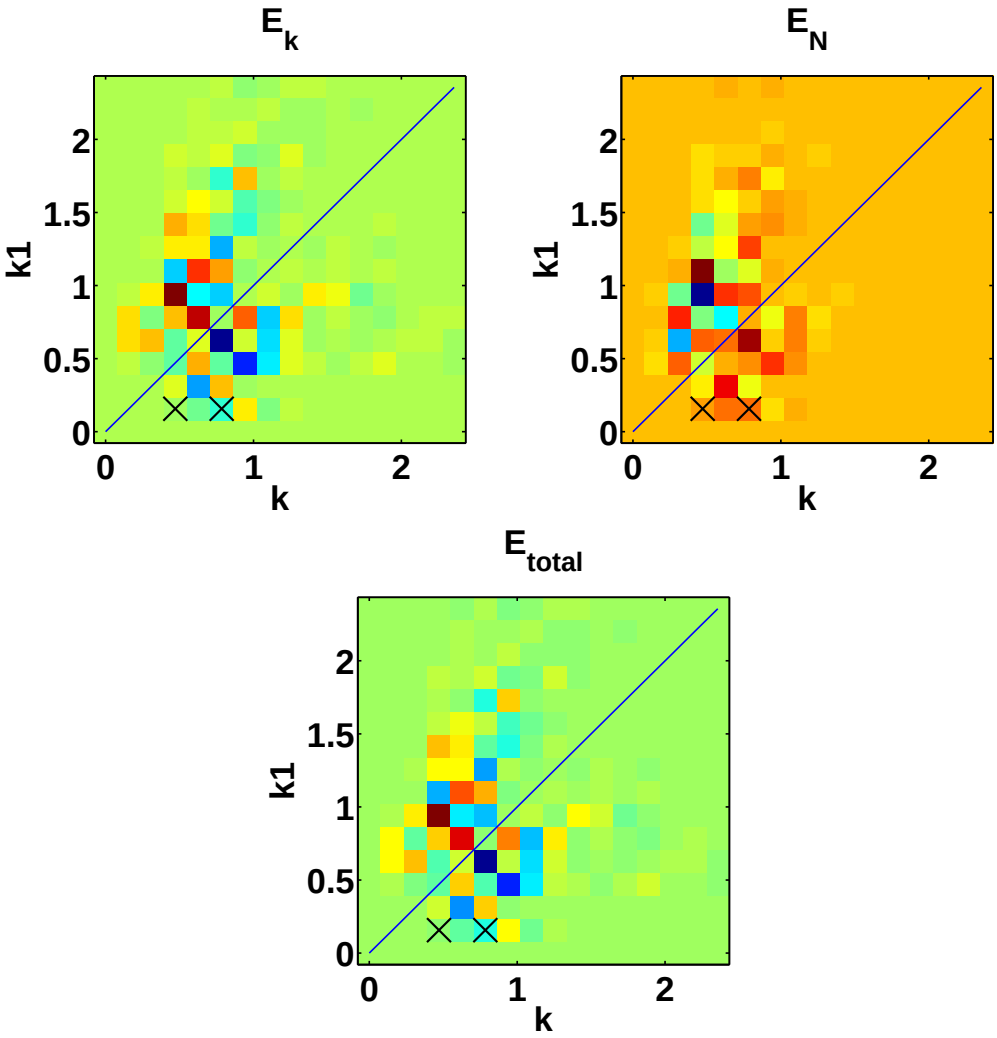

Figure 7.10: Energy transfer functions for the $\alpha = 0.5$ case. They have been produced by averaging over the section that grows at the linear growth rate, $t/\tau \approx 7$ to $t/\tau \approx 11$. Crosses mark modes that are referred to in the text.

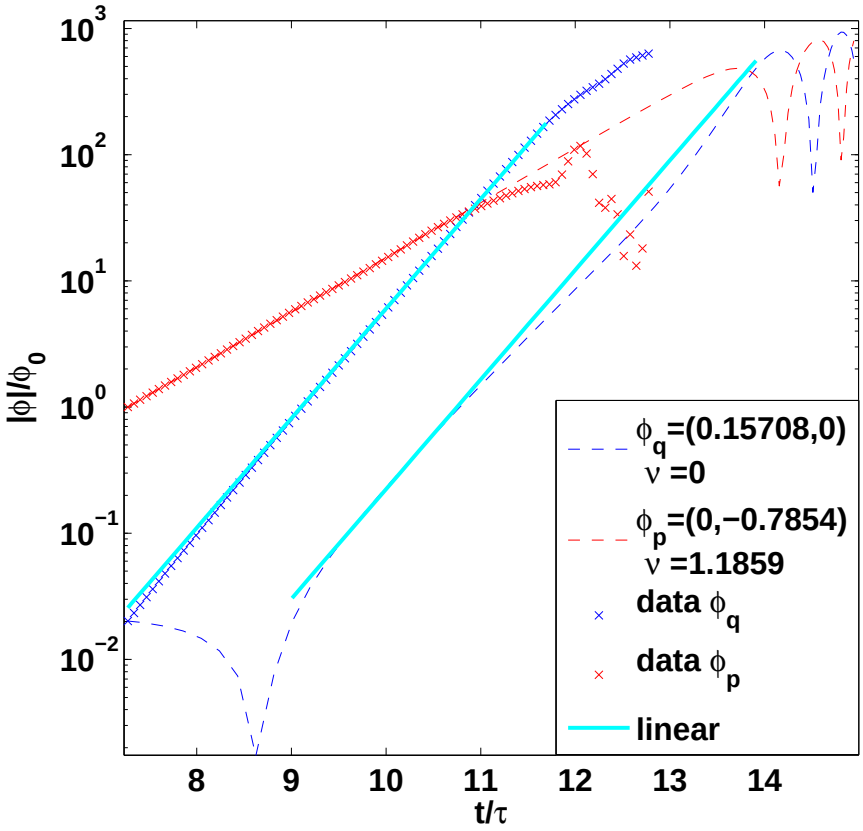

Figure 7.11: Comparing the ODE and linear predictions to the PDE simulation in the $\alpha = 0.5$ case for modes $\vec{p} = (0, -0.785) = (0, \frac{-5\times 2\pi}{L})$ and $\vec{q} = (0.157, 0) = (\frac{2\pi}{L}, 0)$ as indicated by the ETF figures. Markers indicate output from the full simulation, dashed lines predictions from the ODEs, and the line labelled linear is arbitrarily positioned but grows at the linear growth rate. In this case the initial condition had $\phi_q(t = 0) \gg \phi_p(t = 0)$ so the initial conditions for the ODEs was taken at $\frac{t}{\tau} \sim 7$ when this was no longer the case.

7.6 Conclusions

The analytical techniques developed in chapter 5 were extended to model a version of the Extended-Hasegawa-Mima equation that includes a driving term. This driving term was used to reproduce the growth of drift waves as seen in the Extended-Hasegawa-Wakatani system.

Initially attempts were made to find four-wave interactions by examining Fourier space images of the evolution of potential. This was partially successful, if the initial conditions were correctly chosen the correct growth rate of the zonal mode could be found using the ODEs, and for the high–α case with the linear prediction as well.

Energy transfer functions were then used to investigate the behaviour of the system during the linear growth phase. These showed the increased importance of cascades in the low–α case as well as suggesting modes that were interacting more strongly than those originally investigated. These new modes were modelled analytically and it was shown that they displayed linear growth that was better captured by the analytical methods than the modes identified by examining Fourier space images.

Chapter 8

Conclusions

Turbulence is one of the major problems that must be overcome in order to build a tokamak capable of commercial power production. It is such a complicated problem that although it can be included in numerical simulations, this does not always lead to a better understanding of physical processes involved. This is where reduced models of plasma turbulence play a role, despite their apparent simplicity they still contain enough of the physical processes governing turbulence to make analytically tractable predictions of plasma behaviour. In this work they are used to investigate the drift wave to zonal flow transition. The particular models used here were the Extended-Hasegawa-Mima and Extended-Hasegawa-Wakatani equations.

In chapter 5 the Extended-Hasegawa-Mima system was used to investigate the transition to zonal flows caused by four-wave interactions. This is particularly relevant in the EHM system as it has no built in instability, therefore the waves seeded in its initial condition will dominate the early evolution of the system. A truncated ODE description of the system was derived along with a linear dispersion relation for the four-wave zonal flow transition.

The linear dispersion relation was used to produce maps of the linear growth rate for various parameter regimes of the modulational instability. These clearly showed that as the nonlinear terms become more important in the evolution of the system, more modes became unstable. Both the ODEs and linear growth rate predictions were compared with equivalent partial differential equation simulations that were not truncated. For cases where the four waves in the system were in resonance it was shown that both the ODEs and linear dispersion relation accurately predicted the growth rate of the system. In some cases the ODEs were even capable of capturing behaviour other than linear growth, such as the oscillatory behaviour at the beginning of off-axis simulations and the saturation level of moderately nonlinear

systems.

Chapter 6 extended the analytical technique for deriving truncated equations developed in chapter 5 for use with the Extended-Hasegawa-Wakatani system. The EHW system has a separate equation for potential and density, coupled together by assuming electrons experience a resistivity whilst moving parallel to the magnetic field when equilibrating them. The resistivity means that there is a phase shift between perturbations in potential and density, which has an associated linear instability leading the growth of a spectrum of drift waves. This thesis investigated four-mode interactions in the presence of this linearly unstable drift wave spectrum. A truncated ODE model was produced, this time with 8 equations, four for density and four for potential. Unlike the EHM system, it is not possible to derive a stationary dispersion relation for the secondary instability as the time dependence, introduced by the linear growth from the primary instability, cannot be removed.

It was found that the ODEs could predict the growth rate of the zonal mode, although they did not capture other features, such as the saturation level of the full system, as well as for the EHM case. For the cases presented here the zonal mode always grew at approximately twice the rate of the driving mode, which was demonstrated mathematically by considering the case where the driving and satellite modes grew at the same rate.

The chapter finished by using energy transfer functions to investigate whether non-local couplings or local cascades were causing the transition to a zonal configuration. These suggested that the non-local interactions modelled by the ODE equations were present in both the adiabatic, $\alpha = 10$, and non-adiabatic, $\alpha = 0.5$, cases studied. However, only in the high α case was the transition dominated by non-local interactions.

As these energy transfer functions directly measure four-wave interactions from the full simulation they were used to inform the selection of additional interactions to investigate. The ODEs still captured the linear growth rate of these additional interactions and were better able to capture the saturation amplitude of the zonal mode.

Chapter 7 tried to reproduce the growing drift wave spectrum of the Extended-Hasegawa-Wakatani equations in the Extended-Hasegaw-Mima system. To do this a forcing term was added the the EHM equation which drove modes in Fourier space at a rate determined by the primary dispersion relation of the EHW system.

As with the EHW case studied in chapter 6, a spectrum of drift waves was produced and modes from this spectrum were selected for comparison to ODE equations, which had been modified to include the driving term. This time however, some

of the simplicity of the EHM system is recovered as there are only four ODEs to consider.

It was found that the four-mode truncated ODEs once again made reasonable predictions of the growth rate of the zonal modes, but not their saturation behaviour. In the full system interactions with drift waves other than those considered in the four-mode truncation do cause deviations from linear growth. This was particularly noticeable for the case simulating an adiabatic EHW system. For the non-adiabatic case, the real system grew linearly, but at a rate slightly faster than predicted by the ODEs.

Energy transfer functions were again used to contrast local and non-local energy transfer in k-space. The system for which the driving profile was centred on a lower k number once again transitioned to a zonal state via both local and non-local interactions. The energy transfer functions were used to find strongly interacting modes for which the ODEs could better predict the end of the liner growth phase.

Despite the relative simplicity of the driven EHM system, it is still not possible to produce a linear dispersion relation for the drift wave to zonal flow transition. As for the EHW case the growth of the driving mode means that a time stationary solution cannot be found, but making the assumption that the satellite modes grow at the same rate as the driving mode indicates that the zonal mode should grow at twice the rate of the driving mode. This is true for all but the case with cascading behaviour, it is likely that the cascade is enhancing the growth of the zonal mode.

In general, this suggests that four-wave ODE truncations can produce reasonable predictions of the growth rate of the zonal flow in the reduced models studied in this thesis. This is still true, for selected modes, even when an unstable spectrum of drift waves is present. However, it is always possible for interactions with modes not included in the truncation to cause deviations from linear growth, or growth at a rate not predicted by the ODEs. This is especially the case when a spectrum of waves is present, yet even the EHM system can spontaneously grow additional waves that invalidate growth rate predictions.

Bibliography

G.P. Agrawal. *Nonlinear Fiber Optics*. Academic Press. Academic Press, 2013. ISBN 9780123970237. URL http://books.google.co.uk/books?id=xNvw-GDVn84C.

Akio Arakawa. Computational design for long-term numerical integration of the equations of fluid motion: Two-dimensional incompressible flow. part i. *Journal of Computational Physics*, 1(1):119 – 143, 1966. ISSN 0021-9991. doi: 10.1016/0021-9991(66)90015-5. URL http://www.sciencedirect.com/science/article/pii/0021999166900155.

Stepfano Azteni and Jürgen Meyer-ter-Vehn. *The Physics of Inertial Fusion*. Oxford University Press, 2004. ISBN 0198562640.

V. Berionni and Ö. D. Gürcan. Predator prey oscillations in a simple cascade model of drift wave turbulence. *Physics of Plasmas (1994-present)*, 18(11):112301, 2011. doi: http://dx.doi.org/10.1063/1.3656953. URL http://scitation.aip.org/content/aip/journal/pop/18/11/10.1063/1.3656953.

D. Biskamp. *Nonlinear Magnetohydrodynamics*. Cambridge University Press, 1993.

Dieter Biskamp and He Kaifen. Threedriftwave interaction at finite parallel wavelength: Bifurcations and transition to turbulence. *Physics of Fluids (1958-1988)*, 28(7), 1985.

G. Boffetta. Energy and enstrophy fluxes in the double cascade of two-dimensional turbulence. *Journal of Fluid Mechanics*, 589:253–260, 10 2007. ISSN 1469-7645. doi: 10.1017/S0022112007008014. URL http://journals.cambridge.org/article_S0022112007008014.

Guido Boffetta and Robert E. Ecke. Two-dimensional turbulence. *Annual Review of Fluid Mechanics*, 44(1):427–451, 2012. doi: 10.1146/annurev-fluid-120710-101240. URL http://www.annualreviews.org/doi/abs/10.1146/annurev-fluid-120710-101240.

S. I. Braginskii. Transport processes in a plasma. *Reviews of Plasma Physics*, 1: 205, 1965.

Suzana J. Camargo, Dieter Biskamp, and Bruce D. Scott. Resistive driftwave turbulence. *Physics of Plasmas (1994-present)*, 2(1), 1995.

J. G. Charney. On a physical basis for numerical prediciton of large-scale motions in the atmosphere. 6(6):371 – 385, December 1949.

Francis F Chen. Spectrum of low-β plasma turbulence. *Physical Review Letters*, 15 (9):381–383, 1965.

Liu Chen, Zhihong Lin, and Roscoe White. Excitation of zonal flow by drift waves in toroidal plasmas. *Physics of Plasmas (1994-present)*, 7(8), 2000.

G. F. Chew, M. L. Goldberger, and F. E. Low. The boltzmann equation and the one-fluid hydromagnetic equations in the absence of particle collisions. *Proceedings of the Royal Society of London. Series A. Mathematical and Physical Sciences*, 236(1204):112–118, 1956. doi: 10.1098/rspa.1956.0116. URL `http://rspa.royalsocietypublishing.org/content/236/1204/112.abstract`.

Y Choi, Y. V. Lvov, and S. Nazarenko. *Recent Research Developments in Fluid Dynamics*. Number v. 5. Transworld Research Network, 2004. ISBN 9788178951461.

C.P. Connaughton, B.T. Nadiga, S. Nazarenko, and B. Quinn. Modulational instability of rossby and drift waves and generation of zonal jets. *Journal of Fluid Mechanics*, 654:207–231, 2010.

R.O. Dendy. *Plasma Dynamics*. Oxford Science Publications. Clarendon Press, 1990. ISBN 9780198520412. URL `http://books.google.co.uk/books?id=S1C6-4OBOeYC`.

R.L. Dewar and RF Abdullatif. Zonal flow generation by modulational instability. In *Frontiers in turbulence and coherent structures: proceedings of the COSNet/CSIRO Workshop on Turbulence and Coherent Structures in Fluids, Plasmas and Nonlinear Media, the Australian National University, Canberra, Australia, 10-13 January 2006*, volume 6, page 415. World Scientific Pub Co Inc, 2007.

J. M. Dewhurst, B. Hnat, and R. O. Dendy. The effects of nonuniform magnetic field strength on density flux and test particle transport in drift wave turbulence. *Physics of Plasmas*, 16(7):072306, 2009. doi: 10.1063/1.3177382. URL `http://link.aip.org/link/?PHP/16/072306/1`.

P. H. Diamond, Y.-M. Liang, B. A. Carreras, and P. W. Terry. Self-regulating shear flow turbulence: A paradigm for the L to H transition. *Phys. Rev. Lett.*, 72: 2565–2568, Apr 1994. doi: 10.1103/PhysRevLett.72.2565. URL http://link.aps.org/doi/10.1103/PhysRevLett.72.2565.

P. H. Diamond, M. N. Rosenbluth, E. Sanchez, C. Hidalgo, B. Van Milligen, T. Estrada, B. Brañas, M. Hirsch, H. J. Hartfuss, and B. A. Carreras. In search of the elusive zonal flow using cross-bicoherence analysis. *Phys. Rev. Lett.*, 84:4842–4845, May 2000. doi: 10.1103/PhysRevLett.84.4842. URL http://link.aps.org/doi/10.1103/PhysRevLett.84.4842.

P H Diamond, S-I Itoh, K Itoh, and T S Hahm. Zonal flows in plasma – a review. *Plasma Physics and Controlled Fusion*, 47(5):R35, 2005. URL http://stacks.iop.org/0741-3335/47/i=5/a=R01.

W. Dorland and G. W. Hammett. Gyrofluid turbulence models with kinetic effects. *Phys. Fluids B*, 5:812, 1993.

W Dorland, GW Hammett, L Chen, W Park, SC Cowley, S Hamaguchi, and W Horton. Numerical simulations of nonlinear 3-d itg fluid turbulence with an improved landau damping model. *Bull. Am. Phys. Soc*, 35:2005, 1990.

T. Dubos and A. Babiano. Comparing the two-dimensional cascades of vorticity and a passive scalar. *Journal of Fluid Mechanics*, 492:131–145, 10 2003. ISSN 1469-7645. doi: 10.1017/S0022112003005585. URL http://0-journals.cambridge.org.pugwash.lib.warwick.ac.uk/article_S0022112003005585.

T. Dudok de Wit, S. Benkadda, P. Gabbai, and A. D. Verga. Transport and self-organization in dissipative drift-wave turbulence. *Phys. Rev. E*, 52:6753–6758, Dec 1995. doi: 10.1103/PhysRevE.52.6753. URL http://link.aps.org/doi/10.1103/PhysRevE.52.6753.

EFDA, 2013a. URL http://www.efda.org/fusion/fusion-machine/types-of-fusion-machines/stellarators/.

EFDA, 2013b. URL http://www.efda.org/2011/09/tokamak-principle-2/?view=gallery-273.

Ragnar Fjørtoft. On the changes in the spectral distribution of kinetic energy for twodimensional, nondivergent flow. *Tellus*, 5(3):225–230, 1953. ISSN 2153-3490. doi: 10.1111/j.2153-3490.1953.tb01051.x. URL http://dx.doi.org/10.1111/j.2153-3490.1953.tb01051.x.

U. Frisch and P.L. Sulem. Numerical simulation of the inverse cascade in twodimensional turbulence. *Physics of Fluids (1958-1988)*, 27(8), 1984.

Uriel Frisch. *Turbulence*. Cambridge University Press, 1995. ISBN 0521457130.

Akihide Fujisawa. A review of zonal flow experiments. *Nuclear Fusion*, 49(1):013001, 2009. URL `http://stacks.iop.org/0029-5515/49/i=1/a=013001`.

S. Gallagher, B. Hnat, C. Connaughton, S. Nazarenko, and G. Rowlands. The modulational instability in the extended hasegawa-mima equation with a finite larmor radius. *Physics of Plasmas*, 19(12):122115, 2012. doi: 10.1063/1.4773050. URL `http://link.aip.org/link/?PHP/19/122115/1`.

O E Garcia. Collective motions in non-uniformly magnetized plasmas. *European Journal of Physics*, 24(4):331, 2003. URL `http://stacks.iop.org/0143-0807/24/i=4/a=351`.

A.E. Gill. The stability of planetary waves on an infinite betaplane. *Geophysical Fluid Dynamics*, 6(1):29–47, 1974. doi: 10.1080/03091927409365786. URL `http://www.tandfonline.com/doi/abs/10.1080/03091927409365786`.

D.A. Gurnett and A. Bhattacharjee. *Introduction to plasma physics: with space and laboratory applications*. Cambridge University Press, 2005. ISBN 0521367301.

P. N. Guzdar, R. G. Kleva, and Liu Chen. Shear flow generation by drift waves revisited. *Physics of Plasmas)*, 8(2), 2001.

A. Hasegawa and K. Mima. Pseudo-three-dimensional turbulence in magnetized non-uniform plasma. *Phys. Fluids*, 21:87, 1978.

Akira Hasegawa and Masahiro Wakatani. Plasma edge turbulence. *Phys. Rev. Lett.*, 50:682–686, Feb 1983. doi: 10.1103/PhysRevLett.50.682. URL `http://0-link.aps.org.pugwash.lib.warwick.ac.uk/doi/10.1103/PhysRevLett.50.682`.

Akira Hasegawa, Carol G. Maclennan, and Yuji Kodama. Nonlinear behavior and turbulence spectra of drift waves and rossby waves. *Physics of Fluids (1958-1988)*, 22(11), 1979.

R.D. Hazeltine and J.D. Meiss. *Plasma confinement*. Dover Books on Physics Series. Dover Publications, Incorporated, 2003. ISBN 0486432424. URL `http://books.google.co.uk/books?id=s3LQU_04GccC`.

R.D. Hazeltine and F.L. Waelbroeck. *The Framework of Plasma Physics*. Frontiers in Physics. Westview Press, Advanced Book Program, 2004. ISBN 9780813342139. URL http://books.google.co.uk/books?id=iRvjYX8bq08C.

P. Helander and D.J. Sigmar. *Collisional Transport in Magnetized Plasmas*. Cambridge Monographs on Plasma Physics. Cambridge University Press, 2005. ISBN 9780521020985. URL http://books.google.co.uk/books?id=nm-V01E0H2MC.

W Horton. Drift waves and transport. *Reviews of Modern Physics*, 71:735–778, 1999.

ITER Organisation, 2013. URL http://www.iter.org/.

George Em Karniadakis, Moshe Israeli, and Steven A Orszag. High-order splitting methods for the incompressible navier-stokes equations. *Journal of Computational Physics*, 97(2):414 – 443, 1991. ISSN 0021-9991. doi: 10.1016/0021-9991(91)90007-8. URL http://www.sciencedirect.com/science/article/pii/0021999191900078.

R. H. Kraichnan. Inertial-Range Spectrum of Hydromagnetic Turbulence. *Physics of Fluids*, 8:1385–1387, July 1965. doi: 10.1063/1.1761412.

Robert H. Kraichnan. Inertial ranges in twodimensional turbulence. *Physics of Fluids (1958-1988)*, 10(7), 1967a.

Robert H Kraichnan. Inertial ranges in two-dimensional turbulence. *Physics of fluids*, 10:1417, 1967b.

C. N. Lashmore-Davies, D. R. McCarthy, and A. Thyagaraja. The nonlinear dynamics of the modulational instability of drift waves and the associated zonal flows. *Physics of Plasmas*, 8:5121–5133, December 2001. doi: 10.1063/1.1416881.

G. Manfredi, CM Roach, and RO Dendy. Zonal flow and streamer generation in drift turbulence. *Plasma physics and controlled fusion*, 43:825, 2001.

Giovanni Manfredi. Slowly decaying drift turbulence with wave effects. *Journal of Plasma Physics*, 61:601–622, 5 1999. ISSN 1469-7807. doi: null. URL http://journals.cambridge.org/article_S002237789900759X.

P. Manz, M. Ramisch, and U. Stroth. Physical mechanism behind zonal-flow generation in drift-wave turbulence. *Phys. Rev. Lett.*, 103:165004, Oct 2009a. doi: 10.1103/PhysRevLett.103.165004. URL http://link.aps.org/doi/10.1103/PhysRevLett.103.165004.

P Manz, M Ramisch, and U Stroth. Experimental estimation of the dual cascade in two-dimensional drift-wave turbulence. *Plasma Physics and Controlled Fusion*, 51(3):035008, 2009b. URL http://stacks.iop.org/0741-3335/51/i=3/a=035008.

D. R. McCarthy, C. N. Lashmore-Davies, and A. Thyagaraja. Rapid beat generation of large-scale zonal flows by drift waves: A nonlinear generic paradigm. *Phys. Rev. Lett.*, 93:065004, Aug 2004. doi: 10.1103/PhysRevLett.93.065004. URL http://0-link.aps.org.pugwash.lib.warwick.ac.uk/doi/10.1103/PhysRevLett.93.065004.

Volker Naulin. Electromagnetic transport components and sheared flows in drift-alfvn turbulence. *Physics of Plasmas (1994-present)*, 10(10), 2003.

Volker Naulin and Anders H. Nielsen. Accuracy of spectral and finite difference schemes in 2d advection problems. *SIAM J. Sci. Comput.*, 25(1):104–126, January 2003. ISSN 1064-8275. doi: 10.1137/S1064827502405070. URL http://dx.doi.org/10.1137/S1064827502405070.

S. Nazarenko. *Wave Turbulence*. Lecture Notes in Physics. Springer, 2011. ISBN 9783642159411.

Ryusuke Numata, Rowena Ball, and Robert L. Dewar. Bifurcation in electrostatic resistive drift wave turbulence. *Physics of Plasmas*, 14(10):102312, 2007. doi: http://dx.doi.org/10.1063/1.2796106. URL http://scitation.aip.org/content/aip/journal/pop/14/10/10.1063/1.2796106.

D.E. Potter. *Computational physics*. Wiley-Interscience publication. J. Wiley, 1973. ISBN 0471695556.

W.H. Press. *Numerical Recipes in C: The Art of Scientific Computing*. Cambridge University Press, 1988. ISBN 9780521354653.

Brenda E Quinn. *Rossby wave, drift wave and zonal flow turbulence*. PhD thesis, University of Warwick, United Kingdom, 2011.

Bruce D Scott. Energetics of the interaction between electromagnetic exb turbulence and zonal flows. *New Journal of Physics*, 7(1):92, 2005. URL http://stacks.iop.org/1367-2630/7/i=1/a=092.

Bruce D Scott. Computation of turbulence in magnetically confined plasmas. *Plasma Physics and Controlled Fusion*, 48(12B):B277, 2006. URL http://stacks.iop.org/0741-3335/48/i=12B/a=S27.

Bruce D. Scott. Basics of turbulence computation for magnetically confined plasmas. *AIP Conference Proceedings*, 1013(1), 2008.

A. I. Smolyakov, P. H. Diamond, and M. Malkov. Coherent structure phenomena in drift wave˘zonal flow turbulence. *Phys. Rev. Lett.*, 84:491–494, Jan 2000a. doi: 10.1103/PhysRevLett.84.491. URL `http://link.aps.org/doi/10.1103/PhysRevLett.84.491`.

A. I. Smolyakov, P. H. Diamond, and V. I. Shevchenko. Zonal flow generation by parametric instability in magnetized plasmas and geostrophic fluids. *Physics of Plasmas (1994-present)*, 7(5), 2000b.

D. Strintzi and F. Jenko. On the relation between secondary and modulational instabilities. *Physics of Plasmas*, 14(4):042305, 2007. doi: 10.1063/1.2720370. URL `http://link.aip.org/link/?PHP/14/042305/1`.

Paul Terry and Wendell Horton. Stochasticity and the random phase approximation for three electron drift waves. *Physics of Fluids*, 25(3), 1982.

B. Ph. van Milligen, C. Hidalgo, and E. Sánchez. Nonlinear phenomena and intermittency in plasma turbulence. *Phys. Rev. Lett.*, 74:395–398, Jan 1995. doi: 10.1103/PhysRevLett.74.395. URL `http://link.aps.org/doi/10.1103/PhysRevLett.74.395`.

R. E. Waltz. Numerical study of drift wave turbulence with simple models for wavewave nonlinear coupling. *Physics of Fluids (1958-1988)*, 26(1), 1983.

J. Wesson. *Tokamaks*. The International Series of Monographs on Physics Series. Clarendon Press, 2004. ISBN 0198509227.

VE Zakharov. Weak turbulence in media with a decay spectrum. *Journal of Applied Mechanics and Technical Physics*, 6(4):22–24, 1965.

V.E. Zakharov and N.N. Filonenko. Weak turbulence of capillary waves. *Journal of Applied Mechanics and Technical Physics*, 8(5):37–40, 1967. ISSN 0021-8944. doi: 10.1007/BF00915178. URL `http://dx.doi.org/10.1007/BF00915178`.

Vladimir E Zakharov. Collapse of langmuir waves. *Sov. Phys. JETP*, 35(5):908–914, 1972.